Multiscale VEM for the Biot consolidation analysis of complex and highly heterogeneous domains

Abhilash Sreekumar[a], Savvas P. Triantafyllou[b,*], François-Xavier Bécot[c], Fabien Chevillotte[c]

[a] *Centre for Structural Engineering and Informatics, Faculty of Engineering, The University of Nottingham, UK*
[b] *Institute for Structural Analysis and Aseismic Research, School of Civil Engineering, National Technical University of Athens, Greece*
[c] *Matelys - Research Lab 7 rue des Maraîchers Bâtiment B 69120 Vaulx-en-Velin France*

Abstract

We introduce a novel heterogeneous multi-scale method for the consolidation analysis of two-dimensional porous domains with a complex micro-structure. A two-scale strategy is implemented wherein an arbitrary polygonal domain can be discretised into clusters of polygonal elements, each with its own set of fine scale discretization. The method harnesses the advantages of the Virtual Element Method into accurately capturing fine scale heterogeneities of arbitrary polygonal shapes. The upscaling is performed through a set of numerically evaluated multi-scale basis functions. The solution of the coupled governing equations is performed at the coarse-scale at a reduced computational cost. We discuss the computation of the multi-scale basis functions and corresponding virtual projection operators. The performance of the method in terms of accuracy and computational efficiency is evaluated through a set of numerical examples for poro-elastic materials with heterogeneities of various shapes.

Keywords: `consolidation, porous materials, multiscale finite element method, virtual element method`

*Corresponding author
Email address: `savtri@mail.ntua.gr` (Savvas P. Triantafyllou)

1. Introduction

It is often in nature that physics evolve across highly heterogeneous, geometrically complex, and multiscale deformable domains; examples pertain to sound absorption and transmission in foams and fibrous materials [1, 2, 3, 4] and fracture analysis of composite components [5]. Focal point of this work is the mechanical response of highly heterogeneous saturated poro-elastic domains where material variability spans several length scales, within the context of the Biot consolidation theory [6]. Pertinent applications involve large scale geomechanics [7, 8], reservoir modelling and subsurface flows [9], and tissue modelling [10].

Achieving numerical solutions for the Biot consolidation problem in highly heterogeneous domains with standard discretization methods, .e.g, the FEM, BEM [11], etc. necessitates the explicit resolution of all underlying heterogeneities so that i) material distributions are accurately accounted for and ii) geometrical interfaces are accurately resolved. In computational terms, this can be prohibitively expensive. Multiscale modelling methods have been developed over the years to accurately treat heterogeneous material distributions across scales while reducing computational costs using the robust mathematical framework of homogenisation [12]. These include volume averaging [see, e.g., 13], analytical homogenization [14] and computational homogenization approaches [see, e.g., 15, 16], see, also, FE^2 methods [17].

Homogenization theory relies on the assumptions of scale separation and periodicity. However such assumptions do not necessarily hold for the case of highly heterogeneous domains. Hence, alternative methods that do not rely on this assumption have been developed, such as multiscale finite volume [18] and multiscale finite element methods (MsFEM) [19, 20]. A comparison between different multiscale approaches in the context of elliptic problems was performed in [21].

The MsFEM relies on the notion of nested computational domains and the evaluation of a numerical basis that maps quantities, i.e., displacements, from

the one to the other. Contrary to FE^2 (see, e.g., in [17]) methods where a micro-scale finite element mesh is attached to each coarse scale integration point, in the MsFEM the coarse scale is fully spanned by the fine scale. Hence, the MsFEM is more suited to highly heterogeneous domains where scales cannot be fully separated. The MsFEM was based on the pioneering work of [22] and was further developed by, e.g., [23] to resolve flows in highly heterogeneous media.

The Coupling Multiscale Finite Element Method (CMsFEM) [24] was developed to resolve the coupled field fully saturated porous media consolidation problem using a two-scale (meso-macro) approach. Meso-scale heterogeneities are mapped to the macroscopic scale using numerically computed multiscale basis functions. A thorough discussion on the computational gains of the MsFEM and the CMsFEM is provided in [23, 24, 25]. A more specific comparison of different multiscale finite element approaches for composites and porous media flows was done in [26].

In all the aforementioned multiscale finite element methods, scales are meshed with classical quadrilateral elements. Unfortunately, accounting for complex meso-scale morphologies using such elements necessitates quite fine discretizations, rendering the computation of these multiscale basis functions expensive. Optimization of the meshes involved could significantly improve the performance of the method. To do this, one requires numerical methods that can handle more flexible element geometries.

Polygonal finite elements (PFEM) [see, e.g., 27, 28, 29] are used in fluid mechanics [30], contact mechanics [31], computational fracture and damage modelling [32, 33, 34] and topology optimization [35, 35], where one encounters complex inclusion and interface geometries. Analytical basis functions [36] are employed over simplex polyhedra. Numerical approaches are necessary for computing basis functions for non-convex domains such as maximum-entropy [37] and harmonic [38] shape functions. This can significantly drive up computational costs especially in the case of non-linear problems [39, 40]. The Virtual Element Method (VEM) [41, 42, 43, 44, 45, 46, 47] is a recently developed numerical method that specifically addresses these limitations.

The VEM has found extensive application in linear elasticity [48, 49, 50, 51], topology optimization [52], modelling of plates and shells [53, 54, 55], linear and ductile fracture mechanics [56, 57, 58], contact mechanics [59], homogenization of fiber reinforced composites [60], geomechanics and porous media flows [61, 62] and mixed VEM finite-volume discretization of Biot poromechanics [63]. The scheme has recently been extended to account for curved geometries [64, 65, 66]. The method naturally emerged from advances in Mimetic Finite Difference (MFD) methods [see, e.g., 67, 68, 69, 70, 71, 72]. MFDs, when used in conjunction with the Finite Element Method, seek to model trial and test functions spaces without resorting to explicit representations of basis functions over the element interior. When extended to non-standard element geometries, the accuracy of the method is improved by enriching the function spaces with possibly non-polynomial expressions. The basis functions, which are allowed to assumed complex non-polynomial forms, are implicitly defined through carefully chosen degrees of freedom. This implicit representation does away with the problem of analytically or numerically deriving basis functions over complex element domains. A significant point of departure of the VEM from MFDs lies in VEM's attempt to preserve polynomial accuracy over element boundaries [41]. This allows for extension to more generalized inter-element continuity and conformity requirements [73]. The authors have introduced a multiscale VEM formulation for elasto-statics, where the VEM has been introduced within a multiscale setting considering the case of regular coarse element domains only [74]. Very recently, the VEM has been employed within a mixed-formulation setting to address elliptic problems [43, 75, 76]. Furthermore, a three field VEM formulation for the Biot consolidation equations has been presented in [77].

In this work, we harness the merits of the VEM in accurately resolving complex material interfaces and develop a novel Coupled Multiscale Virtual Element Method (CMsVEM) for the consolidation analysis of highly heterogeneous deformable domains across multiple length scales. To achieve this, we recast the three field VEM formulation for the Biot consolidation equations [77] within an engineering context and originally employ it to compute fine scale Representa-

tive Volume Element (RVE) state matrices. Contrary to the work of [63], we employ the VEM to resolve both the solid and pore-pressure governing equations. Further to the methodology provided in [74], the proposed CMsVEM is specifically designed to treat the generic case of arbitrary polygonal coarse element geometries. Using this novel approach, we derive multiscale basis functions to upscale highly heteregoneous porous domains and perform the solution procedure in the time domain at the macroscopic scale at a reduced computational cost. We investigate the potential merits and bottlenecks of the proposed scheme in terms of solution accuracy and computational merits. The influence of the type of boundary conditions used to evaluate the multiscale basis is also examined.

The rest of this manuscript is structured as follows. In Section 2, the governing equations and the VEM formulation for the Biot consolidation problem for fully saturated poroelastic media is presented. The upscaling procedure and associated kinematical constraints used in deriving a CMsVEM is discussed in Section 3. Numerical examples are provided in Section 4 to verify the method and assess its efficiency when comparted to the standard FEM, VEM, and the CMsFEM. Concluding remarks and future outlooks are provided in Section 5.

2. Preliminaries

2.1. Problem Statement

The case of an arbitrary continuous two-dimensional porous domain $\Omega \subset \mathbb{R}^2$ with a domain boundary Γ is considered as shown in Fig. 1a. The domain is subjected to a set of prescribed displacements $\bar{\mathbf{u}}$ on Γ_{u}, enforced pressures $\bar{\mathrm{p}}$ on Γ_{p}, applied tractions $\bar{\mathbf{t}}$ on Γ_{t} and applied volume fluxes $\bar{\mathbf{q}}$ on Γ_{q} such that $\Gamma_{\mathrm{u}} \cap \Gamma_{\mathrm{t}} = \emptyset$ and $\Gamma_{\mathrm{p}} \cap \Gamma_{\mathrm{q}} = \emptyset$. The domain is also subjected to body forces $\mathbf{b}$ and a source/sink term Q.

Considering the case of a linear elastic material, small strains, isothermal conditions, and neglecting inertial effects, the governing equations of the con-

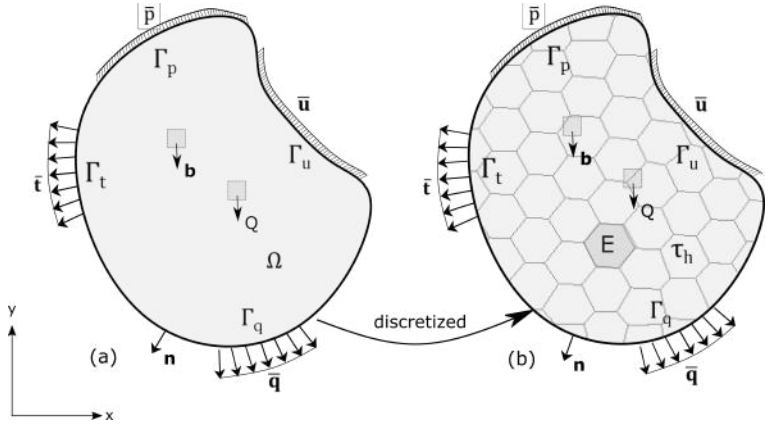

Figure 1: Schematic representation of a two dimensional domain Ω with boundary $\partial\Omega$. (a) Essential and natural boundaries for the solid phase $\bar{\mathbf{u}}$ and $\bar{\mathbf{t}}$ are prescribed on Γ_u and Γ_t respectively. Similarly, the relevant boundaries for the fluid phase $\bar{\mathrm{p}}$ and $\bar{\mathbf{q}}$ are applied on Γ_p and Γ_q respectively. (b) The discretized domain $\mathcal{T}_h$ is decomposed into polygonal elements.

solidation problem assume the following form [24]

$$\mathrm{div}(\mathbb{D}\,\boldsymbol{\varepsilon}(\mathbf{u})) = \mathrm{div}(\alpha_B \mathbf{m}\mathrm{p}) - \mathbf{b} \tag{1a}$$

$$\alpha_B \dot{\boldsymbol{\varepsilon}}_{\mathrm{vol}} + \mathrm{S}_\varepsilon \dot{\mathrm{p}} = \mathrm{div}\Big(\frac{\mathbf{k}}{\gamma_{\mathrm{f}}}\nabla \mathrm{p} + Q\Big), \tag{1b}$$

where $\mathbf{u}$ and p are the vectors of the solid skeleton displacements and the pore-fluid pressures, respectively.

In Eq. (1a), $\boldsymbol{\varepsilon}(\cdot)$ is the strain operator that under the assumption of small strains assumes the following form

$$\boldsymbol{\varepsilon}(\mathbf{u}) = \frac{1}{2}(\nabla \mathbf{u} + (\nabla \mathbf{u})^T), \tag{2}$$

and $\mathbf{m}$ is the identity tensor in Voigt notation, i.e., $\mathbf{m} = \begin{bmatrix} 1 & 1 & 0 \end{bmatrix}^T$. The quantity $\dot{\boldsymbol{\varepsilon}}_{\mathrm{vol}}$ represents the rate of volumetric strain, i.e., $\dot{\boldsymbol{\varepsilon}}_{\mathrm{vol}} = \mathbf{m}^T \boldsymbol{\varepsilon}(\mathbf{u})$. Furthermore, $\mathbb{D}$ is the 2-D elastic constitutive matrix and α_B is the Biot's coefficient.

In Eq. (1b), S_ε is the storage coefficient and $\mathbf{k}$, γ_{f} are the specific permeability and pore-fluid specific viscosity, respectively. Finally, $\mathrm{div}(\cdot)$ and $\nabla(\cdot)$ denote the divergence and gradient operators, respectively and $\dot{(\cdot)}$ denotes differentiation with respect to time. The storage coefficient S_ε is evaluated through the

following expression,

$$\mathrm{S}_\varepsilon = \mathrm{n}\beta + (\alpha_B - \mathrm{n})\mathrm{C}_s, \tag{3}$$

where β, C_s are the pore-fluid and solid-grain compressibility, respectively.

The linear elastic constitutive equations for the solid phase are expressed as

$$\boldsymbol{\sigma} = \mathbb{D}\boldsymbol{\varepsilon}, \tag{4}$$

where $\boldsymbol{\sigma}$ denotes the Cauchy stress tensor. The constitutive relation for the fluid phase is expressed through the static Darcy law for a single phase flow through a porous medium

$$\mathbf{q} = \frac{\mathbf{k}}{\gamma_\mathrm{f}}\nabla \mathrm{p}, \tag{5}$$

where $\mathbf{q}$ denotes the specific discharge, i.e., the specific volume of pore-fluid exiting a control volume; this is expressed as

$$\mathbf{q} = \mathrm{n}(\mathbf{v}_\mathrm{f} - \mathbf{v}_\mathrm{s}), \tag{6}$$

with $\mathbf{v}_f$ and $\mathbf{v}_s$ being the velocities of the pore-fluid and the solid-skeleton, respectively.

The coupled system of Eqs. (1) is supplemented by the following set of initial and boundary conditions

$$\mathbf{u} = \mathbf{u}_0, \qquad \mathrm{p} = \mathrm{p}_0, \quad \text{in } \Omega \quad - \text{initial conditions} \tag{7a}$$

$$\mathbf{u} = \bar{\mathbf{u}} \text{ on } \Gamma_\mathrm{u}, \quad \mathrm{p} = \bar{\mathrm{p}}, \text{ on } \Gamma_\mathrm{p} \quad - \text{enforced boundary conditions} \tag{7b}$$

$$\mathbf{t} = \bar{\mathbf{t}} \text{ on } \Gamma_\mathrm{t}, \quad \mathbf{q} = \bar{\mathbf{q}}, \text{ on } \Gamma_\mathrm{q} \quad - \text{natural boundary conditions}, \tag{7c}$$

where $\mathbf{u}_0$ and p_0 denote the initial displacement and pressure distributions over the domain at time $t = 0$. The Dirichlet boundary values for solid and fluid phases are represented by $\bar{\mathbf{u}}$ and $\bar{\mathrm{p}}$, respectively. The Neumann traction and flux boundary values are contained in $\bar{\mathbf{t}}$ and $\bar{\mathbf{q}}$, respectively.

2.2. Virtual Element discretization

The weak form of the governing Eqs. (1) is derived accordingly as:

$$\begin{cases} \text{Find } (\mathbf{u}, \mathrm{p}) \in \mathcal{V}_1 \times \mathcal{V}_2 := [\mathcal{H}^1(\Omega)]^2 \times [\mathcal{H}^1(\Omega)] \text{ such that :} \\ \mathrm{a}^{\varepsilon}(\mathbf{u}, \mathbf{v})_{\mathbb{D}} - \mathrm{a}^{(\varepsilon,0)}(\mathrm{p}, \mathbf{v})_{\alpha_B \mathbf{m}} = \mathrm{f}^{\mathrm{u}}(\mathbf{v}) \quad \forall\, \mathbf{v} \in \mathcal{V}_1 \\ \mathrm{a}^{(\boldsymbol{\varepsilon},0)}(\dot{\mathbf{u}}, \mathrm{w})_{\alpha_B \mathbf{m}^T} + \mathrm{a}^0(\dot{\mathrm{p}}, \mathrm{w})_{\mathrm{S}_\varepsilon} + \mathrm{a}^{\nabla}(\mathrm{p}, \mathrm{w})_{\mathbf{k}/\gamma_{\mathrm{f}}} = \mathrm{f}^{\mathrm{p}}(\mathrm{w}) \quad \forall\, \mathrm{w} \in \mathcal{V}_2 \ , \end{cases} \tag{8}$$

where $\mathrm{a}^{(\cdot)}$, $\mathrm{f}^{(\cdot)}$ are bilinear and linear functional operators and $\mathbf{v}$ and w are appropriate test functions such that $\mathbf{u}, \mathbf{v} \in \mathcal{V}_1$ and $\mathrm{p}, \mathrm{w} \in \mathcal{V}_2$. The spaces $\mathcal{V}_1$ and $\mathcal{V}_2$ denote the spaces of admissible displacements and pressures, respectively. These assume standard two-dimensional $[\mathcal{H}^1(\Omega)]^2$ and one-dimensional $\mathcal{H}^1(\Omega)$ Hilbert Spaces, respectively.

In this work, the coupled weak form of Eq. (8) is discretized using the Virtual Element Method to account for non-simplex and non-convex element domains. Within this setting, the displacement field is approximated through the following finite dimensional approximation, i.e.,

$$\mathbf{u}_{\mathrm{h}},\ \mathbf{v}_{\mathrm{h}} \in \mathcal{V}_{\mathrm{h}1} \subset \mathcal{V}_1, \tag{9}$$

where $\mathbf{u}_{\mathrm{h}}$ and $\mathbf{v}_{\mathrm{h}}$ are the discretized trial and test functions, respectively; these are defined over a finite-dimensional subspace $\mathcal{V}_{\mathrm{h}1}$.

Similarly, the discretized pressure field trial p_{h} and test w_{h} functions are defined accordingly as

$$\mathrm{p}_{\mathrm{h}},\ \mathrm{w}_{\mathrm{h}} \in \mathcal{V}_{\mathrm{h}2} \subset \mathcal{V}_2, \tag{10}$$

over the finite-dimensional subspace $\mathcal{V}_{\mathrm{h}2}$.

Using the discrete approximations introduced in Eqs. (9) and (10), the abstract formulation of the discretized weak form is expressed

$$\begin{cases} \text{Find } (\mathbf{u}_{\mathrm{h}}, \mathrm{p}_{\mathrm{h}}) \in \mathcal{V}_{\mathrm{h}1} \times \mathcal{V}_{\mathrm{h}2} \text{ such that :} \\ \mathrm{a}^{\varepsilon}(\mathbf{u}_{\mathrm{h}}, \mathbf{v}_{\mathrm{h}})_{\mathbb{D}} - \mathrm{a}^{(\varepsilon,0)}(\mathrm{p}_{\mathrm{h}}, \mathbf{v}_{\mathrm{h}})_{\alpha_B \mathbf{m}} = \mathrm{f}^{\mathrm{u}}(\mathbf{v}_{\mathrm{h}}) \quad \forall\, \mathbf{v}_{\mathrm{h}} \in \mathcal{V}_{\mathrm{h}1} \\ \mathrm{a}^{(\boldsymbol{\varepsilon},0)}(\dot{\mathbf{u}}_{\mathrm{h}}, \mathrm{w}_{\mathrm{h}})_{\alpha_B \mathbf{m}^T} + \mathrm{a}^0(\dot{\mathrm{p}}_{\mathrm{h}}, \mathrm{w}_{\mathrm{h}})_{\mathrm{S}_\varepsilon} + \mathrm{a}^{\nabla}(\mathrm{p}_{\mathrm{h}}, \mathrm{w}_{\mathrm{h}})_{\mathbf{k}/\gamma_{\mathrm{f}}} = \mathrm{f}^{\mathrm{p}}(\mathrm{w}_{\mathrm{h}}) \quad \forall\, \mathrm{w}_{\mathrm{h}} \in \mathcal{V}_{\mathrm{h}2} \ , \end{cases} \tag{11}$$

where $\mathrm{a}^{(\cdot)}$, $\mathrm{f}^{(\cdot)}$ are bilinear and linear functional operators. The individual operators are defined as follows:

$$\mathrm{a}^{\boldsymbol{\varepsilon}}(\mathbf{u}_\mathrm{h}, \mathbf{v}_\mathrm{h})_{\mathbb{D}} = \int_\Omega \boldsymbol{\varepsilon}(\mathbf{u}_\mathrm{h})\, \mathbb{D}\, \boldsymbol{\varepsilon}(\mathbf{v}_\mathrm{h})\, \mathrm{d}\Omega \tag{12a}$$

$$\mathrm{a}^{\boldsymbol{\varepsilon},0}(\mathrm{p}_\mathrm{h}, \mathbf{v}_\mathrm{h})_{\alpha_B \mathbf{m}} = \int_\Omega \boldsymbol{\varepsilon}(\mathbf{v}_\mathrm{h})\, \alpha_B \mathbf{m}\, \mathrm{p}_\mathrm{h}\, \mathrm{d}\Omega \tag{12b}$$

$$\mathrm{a}^{\boldsymbol{\varepsilon},0}(\dot{\mathbf{u}}_\mathrm{h}, \mathrm{w}_\mathrm{h})_{\alpha_B \mathbf{m}^T} = \frac{d}{d\mathrm{t}} \int_\Omega \boldsymbol{\varepsilon}(\mathbf{u}_\mathrm{h})\, \alpha_B \mathbf{m}^T\, \mathrm{w}_\mathrm{h}\, \mathrm{d}\Omega \tag{12c}$$

$$\mathrm{a}^{0}(\dot{\mathrm{p}}_\mathrm{h}, \mathrm{w}_\mathrm{h})_{\mathrm{S}_\varepsilon} = \frac{d}{d\mathrm{t}} \int_\Omega \mathrm{p}_\mathrm{h}\, \mathrm{S}_\varepsilon\, \mathrm{w}_\mathrm{h}\, \mathrm{d}\Omega \tag{12d}$$

$$\mathrm{a}^{\nabla}(\mathrm{p}_\mathrm{h}, \mathrm{w}_\mathrm{h})_{\mathbf{k}/\gamma_f} = \int_\Omega \nabla(\mathrm{p}_\mathrm{h})\, \frac{\mathbf{k}}{\gamma_f}\, \nabla(\mathrm{w}_\mathrm{h})\, \mathrm{d}\Omega \tag{12e}$$

$$\mathrm{f}^{\mathrm{u}}(\mathbf{v}_\mathrm{h}) = \int_{\Gamma_\mathrm{t}} \bar{\mathbf{t}} \cdot \mathbf{v}_\mathrm{h}\, \mathrm{d}\Gamma + \int_\Omega \mathbf{b} \cdot \mathbf{v}_\mathrm{h}\, \mathrm{d}\Omega, \tag{12f}$$

$$\mathrm{f}^{\mathrm{p}}(\mathrm{w}_\mathrm{h}) = -\int_{\Gamma_\mathrm{q}} \bar{\mathbf{q}} \cdot \mathrm{w}_\mathrm{h}\, \mathrm{d}\Gamma + \int_\Omega Q\, \mathrm{w}_h\, \mathrm{d}\Omega. \tag{12g}$$

The nature of the finite-dimensional subspaces $\mathcal{V}_{\mathrm{h}1}$ and $\mathcal{V}_{\mathrm{h}2}$ chosen for the discrete problem varies slightly between the classical FEM and VEM. The FEM approach allows for solutions over simplex elements where the basis functions are explicitly expressed. To extend this approach to account for non-simplex, non-convex element domains, certain conditions on the approximating subspace need to be relaxed. In particular, one allows for a more flexible discretization of Ω into $\mathrm{n_{el}}$ non-intersecting polygonal elements $\mathcal{K}_\mathrm{i}$, $\mathrm{i} = 1, \ldots, \mathrm{n_{el}}$ with arbitrarily defined edges and convexities. The same condition on completeness is required, i.e. $\Omega \approx \mathcal{T}_\mathrm{h}{}^1 = \bigcup_{\mathcal{K}_\mathrm{i} \in \mathcal{T}_\mathrm{h}} \mathcal{K}_\mathrm{i}$ as illustrated in Fig. 1b.

To accommodate for such arbitrary elements, the necessary finite-dimensional space needs to be enlarged, i.e., a weaker definition that allows for non-polynomial function definitions over the element interior, is required. The global virtual

[1] The parameter h is interpreted as the maximum diameter of all elements contained in $\mathcal{T}_\mathrm{h}$.

space of k^{th}-order $V_{\text{h}}^{\text{VEM}}$ is defined as

$$V_{\text{h}}^{\text{VEM}} = \{\text{v} \in [\mathcal{H}^1(\Omega) \cap C^0(\mathcal{T}_{\text{h}})] \ : \ \text{v}|_{\mathcal{K}} \in \mathcal{V}_{\text{h}}^{\mathcal{K}}(\mathcal{K}),\ \forall \mathcal{K} \in \mathcal{T}_{\text{h}}\}, \tag{13}$$

where the local virtual space $\mathcal{V}_{\text{h}}^{\mathcal{K}}$ is defined over an element $\mathcal{K}$ as

$$\mathcal{V}_{\text{h}}^{\mathcal{K}}(\mathcal{K}) = \{\text{v} \in [\mathcal{H}^1(\mathcal{K}) \cap C^0(\mathcal{K})] \ : \ \text{v}_{,i}|_{\text{e}} \in \mathbb{P}_{\text{k}}(\text{e})\ \forall\, \text{e} \in \partial\mathcal{K}\ ; \\ \Delta \mathbf{v}_{,i}|_{\mathcal{K}} \in \mathbb{P}_{k-2}(\mathcal{K}),\ \text{for } i = 1, 2\}. \tag{14}$$

The virtual element spaces $\mathcal{V}_{\text{h1}}$ and $\mathcal{V}_{\text{h2}}$ now assume the following form:

$$\mathcal{V}_{\text{h1}} = [V_{\text{h}}^{\text{VEM}}]^2; \quad \mathcal{V}_{\text{h2}} = V_{\text{h}}^{\text{VEM}}. \tag{15}$$

Based on the aforementioned, we consider a polygonal element $\mathcal{K}$ of N_{v} number of edges and vertices, and area $|\mathcal{K}|$, with arbitrarily chosen polynomial order $\text{k} \geq 1$, as shown in Fig. 2; the corner nodes are represented by ν_{j}, $\text{j} = 1, \ldots, \text{N}_{\text{v}}$. Each edge e_{j}, $\text{j} = 1, \ldots, \text{N}_{\text{v}}$ connects nodes ν_{j} and $\nu_{\text{j+1}}$ and contains $\text{k} - 1$ internal nodes per edge, which are denoted by ν^{e}.

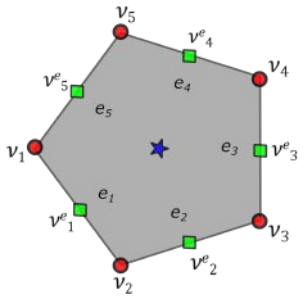

Figure 2: Conventions adopted for computing barycentric coordinates over a polygonal element. The nodes are shown for a $\text{k} = 2$ pentagonal virtual element

The bilinear and linear functional forms used in Eq. (11) can now be computed through assembling local element-wise operators as shown in Eqs. (16).

$$\mathrm{a}^{\boldsymbol{\varepsilon}}(\cdot,\cdot) = \sum_{\mathcal{K}\in\mathcal{T}_\mathrm{h}} \mathrm{a}^{\boldsymbol{\varepsilon}}_{\mathcal{K}}(\cdot,\cdot), \tag{16a}$$

$$\mathrm{a}^{\nabla}(\cdot,\cdot) = \sum_{\mathcal{K}\in\mathcal{T}_\mathrm{h}} \mathrm{a}^{\nabla}_{\mathcal{K}}(\cdot,\cdot), \tag{16b}$$

$$\mathrm{a}^{0}(\cdot,\cdot) = \sum_{\mathcal{K}\in\mathcal{T}_\mathrm{h}} \mathrm{a}^{0}_{\mathcal{K}}(\cdot,\cdot), \tag{16c}$$

$$\mathrm{a}^{(\boldsymbol{\varepsilon},0)}(\cdot,\cdot) = \sum_{\mathcal{K}\in\mathcal{T}_\mathrm{h}} \mathrm{a}^{(\boldsymbol{\varepsilon},0)}_{\mathcal{K}}(\cdot,\cdot), \tag{16d}$$

$$\mathrm{f}^{\mathrm{u}}(\cdot) = \sum_{\mathcal{K}\in\mathcal{T}_\mathrm{h}} \mathrm{f}^{\mathrm{u}}_{\mathcal{K}}(\cdot), \tag{16e}$$

$$\mathrm{f}^{\mathrm{p}}(\cdot) = \sum_{\mathcal{K}\in\mathcal{T}_\mathrm{h}} \mathrm{f}^{\mathrm{p}}_{\mathcal{K}}(\cdot). \tag{16f}$$

The arguments of these functionals belong to either $\mathcal{V}^{\mathcal{K}}_{\mathrm{h}1}(\mathcal{K}) \subset \mathcal{V}_{\mathrm{h}1}(\mathcal{T}_\mathrm{h})$ or $\mathcal{V}^{\mathcal{K}}_{\mathrm{h}2}(\mathcal{K}) \subset \mathcal{V}_{\mathrm{h}2}(\mathcal{T}_\mathrm{h})$. The functions belonging to $\mathcal{V}^{\mathcal{K}}_{\mathrm{h}1}(\mathcal{K})$ and $\mathcal{V}^{\mathcal{K}}_{\mathrm{h}2}(\mathcal{K})$ are not explicitly defined, They are defined implicitly through carefully chosen degrees of freedom (DoFs)[2]. These DoFs are defined in Table 1, where $\mathbb{M}_{k-2}(\mathcal{K})$ and $[\mathbb{M}_{k-2}(\mathcal{K})]^2$ denote spaces containing scalar and vector valued monomials of order $k-2$, respectively.

There are three primary operations performed on the discrete functions as detailed in Eq. (11), i.e., $\boldsymbol{\varepsilon}(\cdot)$ contained in $\mathrm{a}^{\boldsymbol{\varepsilon}}(\cdot,\cdot)$, $\nabla(\cdot)$ contained in $\mathrm{a}^{\nabla}(\cdot,\cdot)$, and $(\cdot)$ contained in $\mathrm{a}^{0}(\cdot,\cdot)$.

The operators $\boldsymbol{\varepsilon}(\cdot)$ and $\nabla(\cdot)$ cannot directly act upon functions belonging to the virtual spaces $\mathcal{V}^{\mathcal{K}}_{\mathrm{h}1}$ and $\mathcal{V}^{\mathcal{K}}_{\mathrm{h}2}$ as they are not explicitly defined. Further, performing numerical integration for all three cases can be computationally expensive. This is because high order quadrature rules are necessary to obtain accurate results for non polynomial integrands.

To avoid this, three operation specific projectors, i.e., $\Pi^{\boldsymbol{\varepsilon}}_{\mathrm{k}}$, $\Pi^{\nabla}_{\mathrm{k}}$ and Π^{0}_{k} are introduced to replace the $\boldsymbol{\varepsilon}(\cdot)$, $\nabla(\cdot)$ and $(\cdot)$ operators respectively. These operators

[2]The member functions of the virtual element spaces $\mathcal{V}^{\mathcal{K}}_{\mathrm{h}1}$ and $\mathcal{V}^{\mathcal{K}}_{\mathrm{h}2}$ are often referred to in VEM literature as a canonical basis Φ. These basis functions are defined implicitly in a barycentric fashion, i.e., $\Phi_\mathrm{i}(\mathbf{x}_\mathrm{j}) = \delta_{\mathrm{ij}}$ where δ_{ij} is the Kronecker Delta function.

DoF Type	**Location**	$\mathcal{V}_{\mathrm{h1}}$		$\mathcal{V}_{\mathrm{h2}}$	
		Number of DoFs	**Description**	**Number of DoFs**	**Description**
Corner	vertices of $\mathcal{K}$	$2\mathrm{N_v}$	$\mathbf{u}_{\mathrm{h}}(\nu_{\mathrm{j}})$, $\mathrm{j}=1,\ldots,\mathrm{N_v}$	$\mathrm{N_v}$	$\mathrm{p_h}(\nu_{\mathrm{j}})$, $\mathrm{j}=1,\ldots,\mathrm{N_v}$
Edge	internal boundary points on each edge of $\mathcal{K}$	$2\mathrm{N_v}(\mathrm{k}-1)$	$\mathbf{u}_{\mathrm{h}}(\nu_{\mathrm{j}}^{\mathrm{e}})$, $\mathrm{j}=1,\ldots,\mathrm{k}-1$ for each edge	$\mathrm{N_v}(\mathrm{k}-1)$	$\mathrm{p_h}(\nu_{j}^{\mathrm{e}})$, $\mathrm{j}=1,\ldots,\mathrm{k}-1$ for each edge
Area Moment	point lying in interior of domain $\mathcal{K}$	$2\frac{\mathrm{k}(\mathrm{k}-1)}{2}$	$\frac{1}{\lvert\mathcal{K}\rvert}\int_{\mathcal{K}}\mathbf{u}_{\mathrm{h}}\cdot\mathbf{m}\,\mathrm{d}\mathcal{K}$ $\forall\,\mathbf{m}\in[\mathbb{M}_{k-2}(\mathcal{K})]^2$	$\frac{\mathrm{k}(\mathrm{k}-1)}{2}$	$\frac{1}{\lvert\mathcal{K}\rvert}\int_{\mathcal{K}}\mathrm{p_h}\cdot\mathrm{m}\,d\mathcal{K}$ $\forall\,\mathrm{m}\in\mathbb{M}_{k-2}(\mathcal{K})$

Table 1: Degrees of Freedom for $\mathcal{V}_{\mathrm{h1}}^{\mathcal{K}}$ and $\mathcal{V}_{\mathrm{h2}}^{\mathcal{K}}$. For Area moment, the monomials belong to $[\mathbb{M}_{k-2}]^2$ and $\mathbb{M}_{k-2}$ spaces, respectively.

project the virtual functions onto an appropriate scalar, or vector polynomial space, denoted by $[\mathbb{P}_{\mathrm{k}}(\mathcal{K})]^{\mathrm{d}},\ \mathrm{d}=1,2$, respectively .

This approximation induces additional error into the formalism. Minimizing the influence of this error is critical to the performance of the VEM. The projectors are defined to this end using the following optimality criteria:

$$\Pi_{\mathrm{k}}^{\boldsymbol{\varepsilon}}:\mathcal{V}_{\mathrm{h1}}^{\mathcal{K}}(\mathcal{K})\to[\mathbb{P}_{\mathrm{k}}(\mathcal{K})]^2:=\ \mathrm{a}_{\mathcal{K}}^{\boldsymbol{\varepsilon}}(\mathbf{u}_{\mathrm{h}}-\Pi_{\mathrm{k}}^{\boldsymbol{\varepsilon}}\mathbf{u}_{\mathrm{h}},\mathbf{m})=0,\quad\forall\,\mathbf{u}_{\mathrm{h}}\in\mathcal{V}_{\mathrm{h1}}^{\mathcal{K}}(\mathcal{K}),\ \mathbf{m}\in[\mathbb{P}_{\mathrm{k}}(\mathcal{K})]^2, \tag{17a}$$

$$\Pi_{\mathrm{k}}^{\nabla}:\mathcal{V}_{\mathrm{h2}}^{\mathcal{K}}(\mathcal{K})\to\mathbb{P}_{\mathrm{k}}(\mathcal{K}):=\ \mathrm{a}_{\mathcal{K}}^{\nabla}(\mathrm{p_h}-\Pi_{\mathrm{k}}^{\nabla}\mathrm{p_h},\mathrm{m})=0,\quad\forall\,\mathrm{p_h}\in\mathcal{V}_{\mathrm{h2}}^{\mathcal{K}}(\mathcal{K}),\ \mathrm{m}\in\mathbb{P}_{\mathrm{k}}(\mathcal{K}), \tag{17b}$$

$$\Pi_{\mathrm{k}}^{0}:\mathcal{V}_{\mathrm{h2}}^{\mathcal{K}}(\mathcal{K})\to\mathbb{P}_{\mathrm{k}}(\mathcal{K}):=\ \mathrm{a}_{\mathcal{K}}^{0}(\mathrm{p_h}-\Pi_{\mathrm{k}}^{0}\mathrm{p_h},\mathrm{m})=0,\quad\forall\,\mathrm{p_h}\in\mathcal{V}_{\mathrm{h2}}^{\mathcal{K}}(\mathcal{K}),\ \mathrm{m}\in\mathbb{P}_{\mathrm{k}}(\mathcal{K}). \tag{17c}$$

The criteria enforced in these definitions ensure that the errors arising from these projections, i.e., $\left(\mathbf{u}_{\mathrm{h}}-\Pi_{\mathrm{k}}^{\boldsymbol{\varepsilon}}\mathbf{u}_{\mathrm{h}}\right)$, $\left(\mathrm{p_h}-\Pi_{\mathrm{k}}^{\nabla}\mathrm{p_h}\right)$ and $\left(\mathrm{p_h}-\Pi_{\mathrm{k}}^{0}\mathrm{p_h}\right)$ are *energetically orthogonal* to the approximating subspaces, $[\mathbb{P}_{\mathrm{k}}(\mathcal{K})]^2$ and $\mathbb{P}_{\mathrm{k}}(\mathcal{K})$, respec-

tively. It follows that the energies associate with these bilinear functionals are computed *exactly*, despite the simplifying assumptions introduced by the polynomial approximations. This property is referred to in standard VEM literature as *polynomial k-consistency* [41].

The approximating subspaces, $[\mathbb{P}_k(\mathcal{K})]^2$ and $\mathbb{P}_k(\mathcal{K})$ are spanned by scaled monomials belonging to $[\mathbb{M}_k(\mathcal{K})]^2$ and $\mathbb{M}_k(\mathcal{K})$, respectively. These monomial spaces also contain members that contribute zero energy to $a^{\boldsymbol{\varepsilon}}_{\mathcal{K}}(\cdot,\cdot)$ and $a^{\nabla}_{\mathcal{K}}(\cdot,\cdot)$, e.g., $\boldsymbol{\varepsilon}([1,\,0]^T) = [0,\,0,\,0]^T$, $\nabla(1) = [0,\,0]^T$. These zero energy modes are specific to the operator considered and are called the *kernel* of the operator. To avoid ill conditioned matrices and consequent spurious results, these are excluded when computing the projectors. The $a^0_{\mathcal{K}}(\cdot,\cdot)$ has no zero energy modes.

Following this reasoning, Eq. (17) can finally be established as follows:

$$\Pi^{\boldsymbol{\varepsilon}}_k := a^{\boldsymbol{\varepsilon}}_{\mathcal{K}}(\mathbf{u}_h - \Pi^{\boldsymbol{\varepsilon}}_k \mathbf{u}_h, \mathbf{m}_j) = 0, \quad \forall\, \mathbf{u}_h \in \mathcal{V}^{\mathcal{K}}_{h1}(\mathcal{K}),\ \mathbf{m}_j \in [\mathbb{M}_k(\mathcal{K})]^2 \setminus \mathbb{K}^{\boldsymbol{\varepsilon}}(\mathcal{K}), \tag{18a}$$

$$\Pi^{\nabla}_k := a^{\nabla}_{\mathcal{K}}(p_h - \Pi^{\nabla}_k p_h, m_j) = 0, \quad \forall\, \mathbf{w}_h \in \mathcal{V}^{\mathcal{K}}_{h2}(\mathcal{K}),\ m_j \in \mathbb{M}_k(\mathcal{K}) \setminus \mathbb{K}^{\nabla}(\mathcal{K}), \tag{18b}$$

$$\Pi^{0}_k := a^{0}_{\mathcal{K}}(p_h - \Pi^{0}_k p_h, m_j) = 0, \quad \forall\, p_h \in \mathcal{V}^{\mathcal{K}}_{h2}(\mathcal{K}),\ m_j \in \mathbb{M}_k(\mathcal{K}), \tag{18c}$$

where $\mathbb{K}^{\boldsymbol{\varepsilon}}(\mathcal{K})$ and $\mathbb{K}^{\nabla}(\mathcal{K})$ belong to the kernels of zero energy modes of $a^{\boldsymbol{\varepsilon}}_{\mathcal{K}}(\cdot,\cdot)$ and $a^{\nabla}_{\mathcal{K}}(\cdot,\cdot)$, respectively. The contents of these spaces can be derived using kinematical decomposition relations mentioned in [76]. The monomials spaces used for the VEM formulation are detailed in Appendix A. The procedure followed in deriving the necessary virtual projectors $\Pi^{\boldsymbol{\varepsilon}}_k$, Π^{∇}_k, Π^0_k is provided in Appendix B. Consequently the associated bilinear functionals $a^{\boldsymbol{\varepsilon}}_{\mathcal{K}}(\cdot,\cdot)$, $a^{\nabla}_{\mathcal{K}}(\cdot,\cdot)$ and $a^0_{\mathcal{K}}(\cdot,\cdot)$ are discussed within a multiscale context in the following section.

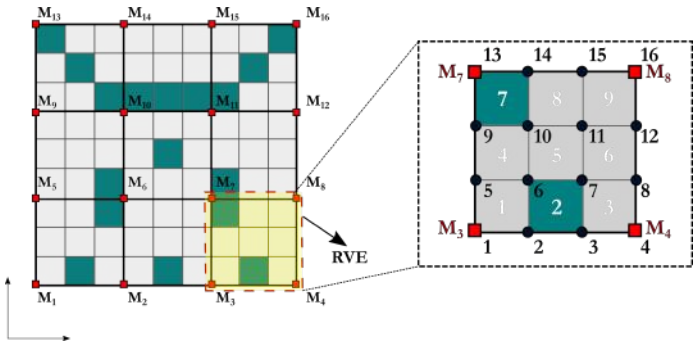

(a)

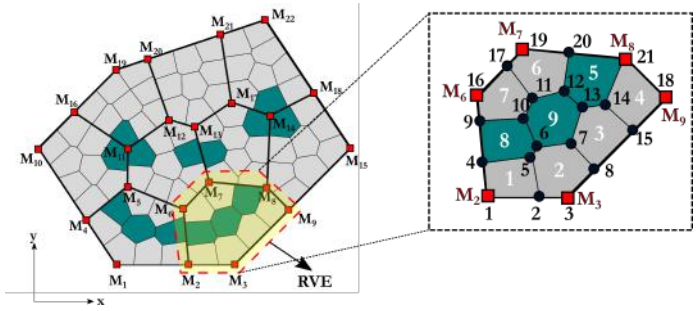

(b)

Figure 3: (a) Multiscale mesh with $n_M = 16$ coarse nodes and $n_{M_{el}} = 9$ quadrilateral coarse elements, each clustering its own fine quadrilateral mesh. (b) Multiscale mesh with $n_M = 22$ coarse nodes and $n_{M_{el}} = 9$ polygonal coarse elements, each clustering its own fine polygonal mesh.

3. Coupled Multiscale Virtual Element Methods for polygonal domains

3.1. Overview

The standard CMsFEM accounts for rectangular elements in the coarse scale and quadrilaterals in the fine scale as shown in Fig. 3a; this limits the applicability of the method especially for the case of inclusions or voids of an arbitrary and typically non-convex geometry. In principle, one would be able to account for such heterogeneities via a very fine finite element discretization; this would considerably increase the number of elements to be resolved at the micro-scale

	Coarse		Fine	
	Nodes	**Elements**	**Nodes**	**Elements**
Fig. 3a	$\mathrm{n_M} = 16$	$\mathrm{n_{M_{el}}} = 9$	$\mathrm{n_m} = 100$	$\mathrm{n_{m_{el}}} = 81$
Fig. 3b	$\mathrm{n_M} = 22$	$\mathrm{n_{M_{el}}} = 9$	$\mathrm{n_m} = 100$	$\mathrm{n_{m_{el}}} = 81$

Table 2: Total number of coarse and fine-scale nodes and elements in the multiscale domains illustrated in Fig. 3

hence countering the computational advantages of the multiscale procedure.

Our objective is to treat the most general case of arbitrarily shaped domains at both the macro- and the micro-scale, see, also, Fig. 3b. To achieve this we harness the flexibility of the the VEM to efficiently resolve non-simplex and non-convex geometries. The discretizations used at both scales in Fig. 3 are summarized in Table 2.

In the proposed CMsVEM, each polygonal coarse-element $\mathcal{K}_{\mathrm{M}(\alpha)}$, $\alpha = 1 \dots \mathrm{n_{M_{el}}}$, clusters its own underlying fine-scale virtual element mesh comprising micro-elements $\mathcal{K}_{\mathrm{m(i)}}$, $\mathrm{i} = 1 \dots \mathrm{n}^{\alpha}_{\mathrm{m_{el}}}$, where $\mathrm{n_{M_{el}}}$ and $\mathrm{n}^{\alpha}_{\mathrm{m_{el}}}$ denote the number of coarse-elements and micro-elements clustered in $\mathcal{K}_{\mathrm{M}(\alpha)}$, respectively . This is illustrated for the case of the coarse element $\mathrm{M_2M_3M_9M_8M_7M_6}$ in Fig. 4.

The resolved parameters at the fine scale are mapped to the coarse scale where the solution of the governing equations is performed. The CMsVEM procedure is schematically depicted in Fig. 4. The upscaling procedure is achieved by numerically deriving appropriate multiscale basis functions to perform this mapping. It is critical that these basis functions sufficiently capture all significant static modes of the coarse element under consideration. In coupled porous consolidation problems, this is equivalent to capturing deformation modes of the solid skeleton and pressure gradient modes of the pore-fluid.

Within this setting, two sets of multiscale basis functions are computed. One set describes the solid skeleton displacements and the other captures the pore-fluid pressure. For these evaluations, both phases are assumed to be decoupled from each other. The basis functions for the displacement field are evaluated

through the solutions of the following homogeneous sub-problems

$$\begin{cases} \text{Find } \mathbf{u}_{\mathrm{h}} \in \mathcal{V}_{\mathrm{h1}}(\mathcal{K}_{\mathrm{M}(\alpha)}) \text{ such that} \\ \mathrm{a}^{\boldsymbol{\varepsilon}}(\mathbf{u}_{\mathrm{h}}, \mathbf{v}_{\mathrm{h}})_{\mathbb{D}} = 0 \quad \forall\, \mathbf{v}_{\mathrm{h}} \in \mathcal{V}_{\mathrm{h1}}(\mathcal{K}_{\mathrm{M}(\alpha)}). \end{cases} \tag{19}$$

Similarly, the fluid phase multiscale basis functions are evaluated as

$$\begin{cases} \text{Find } \mathrm{p}_{\mathrm{h}} \in \mathcal{V}_{\mathrm{h2}}(\mathcal{K}_{\mathrm{M}(\alpha)}) \text{ such that} \\ \mathrm{a}^{\nabla}(\mathrm{p}_{\mathrm{h}}, \mathrm{w}_{\mathrm{h}})_{\mathrm{k}/\gamma_{\mathrm{f}}} = 0 \quad \forall\, \mathrm{w}_{\mathrm{h}} \in \mathcal{V}_{\mathrm{h2}}(\mathcal{K}_{\mathrm{M}(\alpha)}). \end{cases} \tag{20}$$

These equations are subjected to Dirichlet constraints, which are imposed at the coarse element boundary. In CMsFEM the constraints are either linear or periodic in character. Periodic boundaries are not possible in polygonal RVEs. Alternately, a reduced version of the cell problems Eqs. (19) and (20) are solved at the boundary called oscillatory boundary conditions [78]. The implementation of linear and oscillatory boundary conditions is discussed in Section 3.3. The accuracy of the method depends heavily on the ability of the constraints to satisfactorily reflect the physical behaviour of the problem. When encountering comparable coarse and fine length scales in heterogeneous problems, one can artificially enlarge the sampling domain to control resonance errors through oversampling methodologies [25] .

3.2. Virtual fine-scale state matrices

The bilinear forms defined over the coarse-element domain $\mathcal{K}_{\mathrm{M}(\alpha)}$ in Eqs. (19) and (20), respectively can be assembled from individual fine element contributions as shown in Eq. (16):

$$\mathrm{a}^{\boldsymbol{\varepsilon}}(\mathbf{u}_{\mathrm{h}}, \mathbf{v}_{\mathrm{h}}) = \sum_{\mathrm{i}=1}^{\mathrm{n}^{\alpha}_{\mathrm{m_{el}}}} \mathrm{a}^{\boldsymbol{\varepsilon}}_{\mathcal{K}_{\mathrm{m}}}(\mathbf{u}_{\mathrm{h}}, \mathbf{v}_{\mathrm{h}}), \quad \forall (\mathbf{u}_{\mathrm{h}}, \mathbf{v}_{\mathrm{h}}) \in \mathcal{V}^{\mathcal{K}}_{\mathrm{h1}}(\mathcal{K}_{\mathrm{m(i)}}) \subset \mathcal{V}_{\mathrm{h1}}(\mathcal{K}_{\mathrm{M}(\alpha)}) \tag{21a}$$

$$\mathrm{a}^{\nabla}(\mathrm{p}_{\mathrm{h}}, \mathrm{w}_{\mathrm{h}}) = \sum_{\mathrm{i}=1}^{\mathrm{n}^{\alpha}_{\mathrm{m_{el}}}} \mathrm{a}^{\boldsymbol{\varepsilon}}_{\mathcal{K}_{\mathrm{m}}}(\mathrm{p}_{\mathrm{h}}, \mathrm{v}_{\mathrm{h}}), \quad \forall (\mathrm{p}_{\mathrm{h}}, \mathrm{w}_{\mathrm{h}}) \in \mathcal{V}^{\mathcal{K}}_{\mathrm{h2}}(\mathcal{K}_{\mathrm{m(i)}}) \subset \mathcal{V}_{\mathrm{h2}}(\mathcal{K}_{\mathrm{M}(\alpha)}) \tag{21b}$$

Employing the VEM, the solid phase bilinear form at the micro-scale is expressed as

$$\mathrm{a}^{\boldsymbol{\varepsilon}}_{\mathcal{K}_{\mathrm{m}}}(\mathbf{u}_{\mathrm{h}}, \mathbf{v}_{\mathrm{h}}) = \mathrm{a}^{\boldsymbol{\varepsilon}}_{\mathcal{K}_{\mathrm{m}}}\Big((\mathbf{u}_{\mathrm{h}} - \Pi^{\boldsymbol{\varepsilon}_{\mathrm{m}}}_{\mathrm{k}}\mathbf{u}_{\mathrm{h}}) + \Pi^{\boldsymbol{\varepsilon}_{\mathrm{m}}}_{\mathcal{K}}\mathbf{u}_{\mathrm{h}}), (\mathbf{v}_{\mathrm{h}} - \Pi^{\boldsymbol{\varepsilon}_{\mathrm{m}}}_{\mathrm{k}}\mathbf{v}_{\mathrm{h}}) + \Pi^{\boldsymbol{\varepsilon}_{\mathrm{m}}}_{\mathrm{k}}\mathbf{v}_{\mathrm{h}})\Big) \tag{22}$$

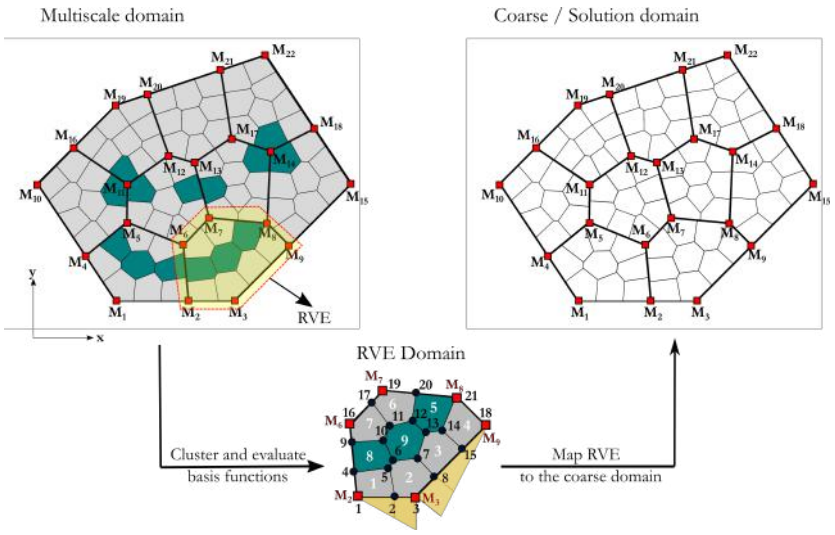

Figure 4: Schematic representation of the CMsVEM upscaling procedure.

and the fluid-phase bilinear form becomes

$$\mathrm{a}^{\nabla}_{\mathcal{K}_\mathrm{m}}(\mathrm{p_h},\mathrm{w_h}) = \mathrm{a}^{\nabla}_{\mathcal{K}_\mathrm{m}}\Big((\mathrm{p_h}-\Pi^{\nabla_\mathrm{m}}_{\mathrm{k}}\mathrm{p_h})+\Pi^{\nabla_\mathrm{m}}_{\mathcal{K}}\mathrm{p_h}),(\mathrm{w_h}-\Pi^{\nabla_\mathrm{m}}_{\mathcal{K}}\mathrm{w_h})+\Pi^{\nabla_\mathrm{m}}_{\mathrm{k}}\mathrm{w_h})\Big), \quad (23)$$

where $\Pi^{\boldsymbol{\varepsilon}_\mathrm{m}}_{\mathrm{k}}$ and $\Pi^{\nabla_\mathrm{m}}_{\mathrm{k}}$ represent the projectors discussed in Section 2.2.

Expanding Eqs. (22) and (23), exploiting the symmetry properties of bilinear functionals and the orthogonality conditions laid out in Eq. (18), one obtains the following relations for the solid phase

$$\mathrm{a}^{\boldsymbol{\varepsilon}}_{\mathcal{K}_\mathrm{m}}(\mathbf{u_h},\mathbf{v_h}) = \underbrace{\mathrm{a}^{\boldsymbol{\varepsilon}}_{\mathcal{K}_\mathrm{m}}(\Pi^{\boldsymbol{\varepsilon}_\mathrm{m}}_{\mathrm{k}}\mathbf{u_h},\Pi^{\boldsymbol{\varepsilon}_\mathrm{m}}_{\mathrm{k}}\mathbf{v_h})}_{\text{solid phase consistency term}} + \underbrace{\mathrm{a}^{\boldsymbol{\varepsilon}}_{\mathcal{K}_\mathrm{m}}(\mathbf{u_h}-\Pi^{\boldsymbol{\varepsilon}_\mathrm{m}}_{\mathrm{k}}\mathbf{u_h},\mathbf{v_h}-\Pi^{\boldsymbol{\varepsilon}_\mathrm{m}}_{\mathrm{k}}\mathbf{v_h})}_{\text{solid phase stability term}}, \quad (24)$$

and the fluid-phase

$$\mathrm{a}^{\nabla}_{\mathcal{K}_\mathrm{m}}(\mathrm{p_h},\mathrm{w_h}) = \underbrace{\mathrm{a}^{\nabla}_{\mathcal{K}_\mathrm{m}}(\Pi^{\nabla_\mathrm{m}}_{\mathcal{K}}\mathrm{p_h},\Pi^{\nabla_\mathrm{m}}_{\mathcal{K}}\mathrm{w_h})}_{\text{fluid phase consistency term}} + \underbrace{\mathrm{a}^{\nabla}_{\mathcal{K}_\mathrm{m}}(\mathrm{p_h}-\Pi^{\nabla_\mathrm{m}}_{\mathcal{K}}\mathrm{p_h},\mathrm{w_h}-\Pi^{\nabla_\mathrm{m}}_{\mathcal{K}}\mathrm{w_h})}_{\text{fluid phase stability term}}, \quad (25)$$

respectively. The corresponding fine scale VEM expressions for $\mathrm{a}^{0}(\mathrm{p_h},\mathrm{w_h})$ and $\mathrm{a}^{(\boldsymbol{\varepsilon},0)}(\mathbf{u_h},\mathrm{w_h})$ are derived in a similar manner and are omitted for brevity.

Remark 1. *The consistency terms comprise entirely polynomial terms and hence can be computed analytically. However, this is not coercive. The stability term is*

introduced to overcome this rank-deficiency. Any bilinear form satisfying basic coercivity and stability properties can be taken up as the stability term. It is designed to reduce to zero over polynomial subspaces. The stability terms contain non-polynomial integrands $\mathbf{u}_h$, $\mathbf{v}_h$, p_h *and* w_h *that have no explicit expression over the element domain, therefore an exact computation is impossible. Obtaining close numerical approximations require higher order numerical quadrature rules, rendering the procedure computationally expensive. Conversely, the stability terms can be estimated with easy to compute forms that approximate the energy contributed by higher order modes. The additional error introduced through this approximation is chosen such that optimal error convergence rates are still achieved.*

Based on the approximation of the stability term, the expression of the solid-phase element-wise bilinear operator at the micro-scale assumes the following form

$$\mathrm{a}^{\boldsymbol{\varepsilon}}_{\mathcal{K}_\mathrm{m}}(\mathbf{u}_\mathrm{h},\mathbf{v}_\mathrm{h}) \approx \mathrm{a}^{\boldsymbol{\varepsilon}}_{\mathcal{K}_\mathrm{m}}(\Pi^{\boldsymbol{\varepsilon}_\mathrm{m}}_\mathrm{k}\mathbf{u}_\mathrm{h},\Pi^{\boldsymbol{\varepsilon}_\mathrm{m}}_\mathrm{k}\mathbf{v}_\mathrm{h}) + \mathcal{S}^{\boldsymbol{\varepsilon}}_{\mathcal{K}_\mathrm{m}}(\mathbf{u}_\mathrm{h}-\Pi^{\boldsymbol{\varepsilon}_\mathrm{m}}_\mathrm{k}\mathbf{u}_\mathrm{h},\mathbf{v}_\mathrm{h}-\Pi^{\boldsymbol{\varepsilon}_\mathrm{m}}_\mathrm{k}\mathbf{v}_\mathrm{h}), \quad (26)$$

where $\mathcal{S}^{\boldsymbol{\varepsilon}}_{\mathcal{K}_\mathrm{m}}(\cdot,\cdot)$ denotes the stability term approximation.

The corresponding element-wise approximations for the fluid phases are expressed as

$$\mathrm{a}^{\nabla}_{\mathcal{K}_\mathrm{m}}(\mathrm{p}_\mathrm{h},\mathrm{w}_\mathrm{h}) \approx \mathrm{a}^{\nabla}_{\mathcal{K}_\mathrm{m}}(\Pi^{\nabla_\mathrm{m}}_{\mathcal{K}}\mathrm{p}_\mathrm{h},\Pi^{\nabla_\mathrm{m}}_{\mathcal{K}}\mathrm{w}_\mathrm{h}) + \mathcal{S}^{\nabla}_{\mathcal{K}_\mathrm{m}}(\mathrm{p}_\mathrm{h}-\Pi^{\nabla_\mathrm{m}}_{\mathcal{K}}\mathrm{p}_\mathrm{h},\mathrm{w}_\mathrm{h}-\Pi^{\nabla_\mathrm{m}}_{\mathcal{K}}\mathrm{w}_\mathrm{h}) \quad (27a)$$

$$\mathrm{a}^{0}_{\mathcal{K}_\mathrm{m}}(\mathrm{p}_\mathrm{h},\mathrm{w}_\mathrm{h}) \approx \mathrm{a}^{0}_{\mathcal{K}_\mathrm{m}}(\Pi^{\boldsymbol{\varepsilon}_\mathrm{m}}_\mathrm{k}\mathrm{p}_\mathrm{h},\Pi^{\boldsymbol{\varepsilon}_\mathrm{m}}_\mathrm{k}\mathrm{w}_\mathrm{h}) + \mathcal{S}^{0}_{\mathcal{K}_\mathrm{m}}(\mathrm{p}_\mathrm{h}-\Pi^{\boldsymbol{\varepsilon}_\mathrm{m}}_\mathrm{k}\mathrm{p}_\mathrm{h},\mathrm{w}_\mathrm{h}-\Pi^{\boldsymbol{\varepsilon}_\mathrm{m}}_\mathrm{k}\mathrm{w}_\mathrm{h}), \quad (27b)$$

where $\mathcal{S}^{\nabla}_{\mathcal{K}_\mathrm{m}}(\cdot,\cdot)$ and $\mathcal{S}^{0}_{\mathcal{K}_\mathrm{m}}(\cdot,\cdot)$ denote the stability term approximations for $\mathrm{a}^{\nabla}_{\mathcal{K}_\mathrm{m}}(\cdot,\cdot)$ and $\mathrm{a}^{0}_{\mathcal{K}_\mathrm{m}}(\cdot,\cdot)$, respectively.

Finally, the VEM approximation for the coupling term is expressed as

$$\mathrm{a}^{(\boldsymbol{\varepsilon},0)}_{\mathcal{K}_\mathrm{m}}(\mathbf{u}_\mathrm{h},\mathrm{w}_\mathrm{h}) \approx \mathrm{a}^{(\boldsymbol{\varepsilon},0)}_{\mathcal{K}_\mathrm{m}}(\Pi^{\nabla_\mathrm{m}}_{\mathcal{K}}\mathbf{u}_\mathrm{h},\Pi^{\nabla_\mathrm{m}}_{\mathcal{K}}\mathrm{w}_\mathrm{h}) + \mathcal{S}^{(\boldsymbol{\varepsilon},0)}_{\mathcal{K}_\mathrm{m}}(\mathbf{u}_\mathrm{h}-\Pi^{\nabla_\mathrm{m}}_{\mathcal{K}}\mathbf{u}_\mathrm{h},\mathrm{w}_\mathrm{h}-\Pi^{\nabla_\mathrm{m}}_{\mathcal{K}}\mathrm{w}_\mathrm{h}), \quad (28)$$

where $\mathcal{S}^{(\boldsymbol{\varepsilon},0)}_{\mathcal{K}_\mathrm{m}}$ is the corresponding stability term. The choice of these stability terms are not unique. One is referred to [79, 80, 81] for an extensive discussion on the properties of stability terms.

Expanding Eqs. (26)-(28) and re-writing in matrix form following Eq. (12), the following set of state-matrices is eventually defined at the micro-scale, i.e.,

$$\mathbf{K}^{\mathrm{el},\alpha}_{\mathrm{m(i)}} \approx \mathrm{a}^{\boldsymbol{\varepsilon}}_{\mathcal{K}_{\mathrm{m}}}(\mathbf{u}_{\mathrm{h}},\mathbf{v}_{\mathrm{h}})_{\mathbb{D}} = \int\limits_{\mathcal{K}_{\mathrm{m(i)}}} \boldsymbol{\varepsilon}\Big(\Pi^{\boldsymbol{\varepsilon}}_{\mathrm{k}}(\mathbf{u}_{\mathrm{h}})\Big)^{T}\mathbf{D}\,\boldsymbol{\varepsilon}\Big(\Pi^{\boldsymbol{\varepsilon}}_{\mathrm{k}}(\mathbf{v}_{\mathrm{h}})\Big)\,\mathrm{d}\mathcal{K} + \mathcal{S}^{\mathrm{K}}_{\mathcal{K}_{\mathrm{m}}}(\mathbf{u}_{\mathrm{h}},\mathbf{v}_{\mathrm{h}}) \tag{29a}$$

$$\mathbf{Q}^{\mathrm{el},\alpha}_{\mathrm{m(i)}} \approx \mathrm{a}^{(\boldsymbol{\varepsilon},0)}_{\mathcal{K}_{\mathrm{m}}}(\mathbf{u}_{\mathrm{h}},\mathrm{w}_{\mathrm{h}})_{\alpha_B\mathbf{m}} = \int\limits_{\mathcal{K}_{\mathrm{m(i)}}} \boldsymbol{\varepsilon}\Big(\Pi^{\boldsymbol{\varepsilon}}_{\mathrm{k}}(\mathbf{u}_{\mathrm{h}})\Big)^{T}\alpha\mathbf{m}\,\Big(\Pi^{0}_{\mathrm{k}}(\mathbf{w}_{\mathrm{h}})\Big)\,\mathrm{d}\mathcal{K} + \mathcal{S}^{\mathrm{Q}}_{\mathcal{K}_{\mathrm{m}}}(\mathbf{u}_{\mathrm{h}},\mathrm{w}_{\mathrm{h}}), \tag{29b}$$

$$\mathbf{H}^{\mathrm{el},\alpha}_{\mathrm{m(i)}} \approx \mathrm{a}^{\nabla}_{\mathcal{K}_{\mathrm{m}}}(\mathrm{p}_{\mathrm{h}},\mathrm{w}_{\mathrm{h}})_{\mathbf{k}/\gamma_{\mathrm{f}}} = \int\limits_{\mathcal{K}_{\mathrm{m(i)}}} \nabla\Big(\Pi^{\nabla}_{\mathrm{k}}(\mathrm{p}_{\mathrm{h}})\Big)^{T}\frac{\mathbf{k}}{\gamma_{\mathrm{f}}}\,\nabla\Big(\Pi^{\nabla}_{\mathrm{k}}(\mathrm{w}_{\mathrm{h}})\Big)\,\mathrm{d}\mathcal{K} + \mathcal{S}^{\mathrm{H}}_{\mathcal{K}_{\mathrm{m}}}(\mathrm{p}_{\mathrm{h}},\mathrm{w}_{\mathrm{h}}) \tag{29c}$$

$$\mathbf{S}^{\mathrm{el},\alpha}_{\mathrm{m(i)}} \approx \mathrm{a}^{0}_{\mathcal{K}_{\mathrm{m}}}(\mathrm{p}_{\mathrm{h}},\mathrm{w}_{\mathrm{h}})_{\mathrm{S}_{\boldsymbol{\varepsilon}}} = \underbrace{\int\limits_{\mathcal{K}_{\mathrm{m(i)}}} \Big(\Pi^{0}_{\mathrm{k}}(\mathrm{p}_{\mathrm{h}})\Big)^{T}\mathrm{S}_{\boldsymbol{\varepsilon}}\,\Big(\Pi^{0}_{\mathrm{k}}(\mathrm{w}_{\mathrm{h}})\Big)\,\mathrm{d}\mathcal{K}}_{\text{consistency}} + \underbrace{\mathcal{S}^{\mathrm{S}}_{\mathcal{K}_{\mathrm{m}}}(\mathrm{p}_{\mathrm{h}},\mathrm{w}_{\mathrm{h}})}_{\text{stability}}. \tag{29d}$$

where the expressions for the consistency and stability state matrices are provided in Appendix C and Appendix D, respectively.

These fine scale matrices can be assembled over the coarse element domain to provide the RVE state matrices using a direct approach:

$$\mathbf{K}^{\alpha}_{\mathrm{m}} = \mathop{\mathrm{A}}_{\mathrm{i}=1}^{\mathrm{n}_{\mathrm{m_{el}}}} \mathbf{K}^{\mathrm{el},\alpha}_{\mathrm{m(i)}}, \quad \mathbf{Q}^{\alpha}_{\mathrm{m}} = \mathop{\mathrm{A}}_{\mathrm{i}=1}^{\mathrm{n}_{\mathrm{m_{el}}}} \mathbf{Q}^{\mathrm{el},\alpha}_{\mathrm{m(i)}}, \quad \mathbf{H}^{\alpha}_{\mathrm{m}} = \mathop{\mathrm{A}}_{\mathrm{i}=1}^{\mathrm{n}_{\mathrm{m_{el}}}} \mathbf{H}^{\mathrm{el},\alpha}_{\mathrm{m(i)}}, \quad \mathbf{S}^{\alpha}_{\mathrm{m}} = \mathop{\mathrm{A}}_{\mathrm{i}=1}^{\mathrm{n}_{\mathrm{m_{el}}}} \mathbf{S}^{\mathrm{el},\alpha}_{\mathrm{m(i)}}. \tag{30}$$

The state-matrices defined in (30) are used to evaluate the multiscale basis functions as discussed in Section 3.3.

Remark 2. *A virtual element formulation is not necessary for the load vectors for our upscaling purposes. This is so because while the state matrices are evaluated at the fine scale for an RVE, the load vectors, in the absence of source/sink terms and body forces, can directly be evaluated over the boundary at the coarse scale thus rendering a virtual element approach unnecessary.*

3.3. Constructing multiscale basis functions

The micro-nodal field variables $\mathbf{u}_{\mathrm{m}}^{\alpha}$ and $\mathrm{p}_{\mathrm{m}}^{\alpha}$ are mapped to the associated coarse-nodes using the following relations:

$$\begin{aligned}
\mathrm{u}_{\mathrm{mx,i}}^{\alpha} &= \sum_{\mathrm{J}=1}^{\mathrm{n_M}} \mathrm{N}_{\mathrm{iJxx}}^{\mathrm{u}} \mathrm{u}_{\mathrm{Mx,J}} + \sum_{\mathrm{J}=1}^{\mathrm{n_M}} \mathrm{N}_{\mathrm{iJxy}}^{\mathrm{u}} \mathrm{u}_{\mathrm{My,J}} \\
\mathrm{u}_{\mathrm{my,i}}^{\alpha} &= \sum_{\mathrm{J}=1}^{\mathrm{n_M}} \mathrm{N}_{\mathrm{iJyx}}^{\mathrm{u}} \mathrm{u}_{\mathrm{Mx,J}} + \sum_{\mathrm{J}=1}^{\mathrm{n_M}} \mathrm{N}_{\mathrm{iJyy}}^{\mathrm{u}} \mathrm{u}_{\mathrm{My,J}} \\
\mathrm{p}_{\mathrm{m,i}}^{\alpha} &= \sum_{\mathrm{J}=1}^{\mathrm{n_M}} \mathrm{N}_{\mathrm{iJ}}^{\mathrm{p}} \mathrm{p}_{\mathrm{M,J}},
\end{aligned} \tag{31}$$

where $\mathrm{u}_{\mathrm{mx,i}}$, $\mathrm{u}_{\mathrm{mx,i}}$ and $\mathrm{p}_{\mathrm{m,i}}$, $\mathrm{i} = 1 \ldots \mathrm{n}_{\mathrm{m}}^{\alpha}$ are the displacement and pressure components of the i^{th} micro-node, $\mathrm{n}_{\mathrm{m}}^{\alpha}$ is the number of micro-nodes within the coarse-element α and $\mathrm{n_M}$ is the number of coarse-nodes belonging to the α^{th} coarse-element. The terms $\mathrm{u}_{\mathrm{Mx,J}}$, $\mathrm{u}_{\mathrm{My,J}}$ and $\mathrm{p}_{\mathrm{M,J}}$ denote the displacement and pressure components at the J^{th} macro-node of the α^{th} coarse-element. The multiscale basis functions $\mathrm{N}_{\mathrm{iJxx}}^{\mathrm{u}}$, $\mathrm{N}_{\mathrm{iJxy}}^{\mathrm{u}}$, $\mathrm{N}_{\mathrm{iJyx}}^{\mathrm{u}}$, $\mathrm{N}_{\mathrm{iJyy}}^{\mathrm{u}}$ and $\mathrm{N}_{\mathrm{iJ}}^{\mathrm{p}}$ interpolate the fine-scale displacements and pressures, respectively. The relations in Eq. (31) hold only if:

$$\begin{aligned}
&\sum_{\mathrm{J}=1}^{\mathrm{n_M}} \mathrm{N}_{\mathrm{IJxx}}^{\mathrm{u}} = 1 \quad \sum_{\mathrm{J}=1}^{\mathrm{n_M}} \mathrm{N}_{\mathrm{IJxy}}^{\mathrm{u}} = 0 \\
&\sum_{\mathrm{J}=1}^{\mathrm{n_M}} \mathrm{N}_{\mathrm{IJyx}}^{\mathrm{u}} = 0 \quad \sum_{\mathrm{J}=1}^{\mathrm{n_M}} \mathrm{N}_{\mathrm{IJyy}}^{\mathrm{u}} = 1 \quad , \mathrm{I} = 1 \ldots \mathrm{n_M}, \\
&\sum_{\mathrm{J}=1}^{\mathrm{n_M}} \mathrm{N}_{\mathrm{IJ}}^{\mathrm{p}} = 1
\end{aligned} \tag{32}$$

The RVE specific fine-element nodal displacements $\mathbf{u}_{\mathrm{m}}^{\alpha} = [\mathrm{u}_{\mathrm{mx}},\ \mathrm{u}_{\mathrm{my}}]^T$, and pressures $\mathrm{p}_{\mathrm{m}}^{\alpha}$ are associated with the corresponding coarse-element field variables through the following equations, i.e.,

$$\mathbf{u}_{\mathrm{m(i)}}^{\alpha} = \mathbf{N}_{\mathrm{m(i)}}^{\mathrm{u}} \mathbf{u}_{\mathrm{M}(\alpha)} \tag{33a}$$

$$\mathbf{p}_{\mathrm{m(i)}}^{\alpha} = \mathbf{N}_{\mathrm{m(i)}}^{\mathrm{p}} \mathbf{p}_{\mathrm{M}(\alpha)}, \tag{33b}$$

where $\mathbf{u}_{\mathrm{m(i)}}^{\alpha}$ and $\mathbf{p}_{\mathrm{m(i)}}^{\alpha}$ denote the displacement and pressure vectors for the i^{th} fine-element in the α^{th} element. The arrays $\mathbf{N}_{\mathrm{m(i)}}^{\mathrm{u}}$ and $\mathbf{N}_{\mathrm{m(i)}}^{\mathrm{p}}$ represent the multiscale basis functions mapping the α^{th} coarse-element nodal displacements $\mathbf{u}_{\mathrm{M}(\alpha)}$ and pressures $\mathbf{p}_{\mathrm{M}(\alpha)}$ to the fine-scale.

Collecting the contributions from each fine-element, Eq. (33) can be expressed over the entire RVE:

$$\mathbf{u}_{\mathrm{m}}^{\alpha} = \mathbf{N}_{\mathrm{m}}^{\mathrm{u}} \mathbf{u}_{\mathrm{M}(\alpha)} \tag{34a}$$

$$\mathbf{p}_{\mathrm{m}}^{\alpha} = \mathbf{N}_{\mathrm{m}}^{\mathrm{p}} \mathbf{p}_{\mathrm{M}(\alpha)}, \tag{34b}$$

where $\mathbf{N}_{\mathrm{m}}^{\mathrm{u}}$ and $\mathbf{N}_{\mathrm{m}}^{\mathrm{p}}$ correspond to the coarse element multi-scale basis functions for the displacement and pressure field, respectively. Each column of these arrays corresponds to a possible static displacement or pressure mode of the RVE. To compute these snapshots of the system in a manner consistent with Eqs. (31) and (32), the discretized matrix forms of the boundary value sub-problems in Eqs. (19) and (20) are solved over the RVE domain:

$$\begin{cases} \mathbf{K}_{\mathrm{m}}^{\alpha} \mathbf{u}_{\mathrm{m}}^{\alpha} = \{\emptyset\} & , \text{on } \mathcal{K}_{\mathrm{M}(\alpha)} \\ \mathbf{u}_{\mathrm{S}} = \bar{\mathbf{u}}_{\mathrm{IJ}} & , \text{on } \partial\mathcal{K}_{\mathrm{M}(\alpha)} \end{cases}, \mathrm{I} = 1 \ldots \mathrm{n_M}, \mathrm{J} = 1, 2 \tag{35}$$

$$\begin{cases} \mathbf{H}_{\mathrm{m}}^{\alpha} \mathbf{p}_{\mathrm{m}}^{\alpha} = \{\emptyset\} & , \text{on } \mathcal{K}_{\mathrm{M}(\alpha)} \\ \mathbf{p}_{\mathrm{S}} = \bar{\mathbf{p}}_{\mathrm{IJ}} & , \text{on } \partial\mathcal{K}_{\mathrm{M}(\alpha)} \end{cases}, \mathrm{I} = 1 \ldots \mathrm{n_M}, \mathrm{J} = 1 \tag{36}$$

where $\mathbf{K}_{\mathrm{m}}^{\alpha}$ and $\mathbf{H}_{\mathrm{m}}^{\alpha}$ are the RVE specific state matrices, which are assembled from fine-element contributions using Eq. (29) and (30), respectively.

In the CMsFEM, the prescribed displacements $\mathbf{u}_{\mathrm{S}}$ and pressures $\mathbf{p}_{\mathrm{S}}$ at the RVE boundary are assigned linear or periodic kinematical constraints $\bar{\mathbf{u}}$ and $\bar{\mathbf{p}}$. For generalized polygonal RVEs (Fig. 5b), assigning periodic constraints is not possible. Alternatively, oscillatory boundaries are used, i.e., reduced versions of Eq. (35) and Eq. (36) are solved over the required edges of the RVE.

In comparison to prescribing linear constraints (Fig. 5a), oscillatory conditions allow for a less rigid enforcement of displacement and pressure profiles along the RVE boundaries (Fig. 5b). Furthermore, the effect of material heterogeneities along the boundaries naturally emerges in the evaluation of the of the corresponding displacement profiles hence providing a physically rigorous approach to the evaluation of the multiscale basis functions. The procedure followed in assigning these kinematical constraints is provided in Appendix E for the sake of completeness.

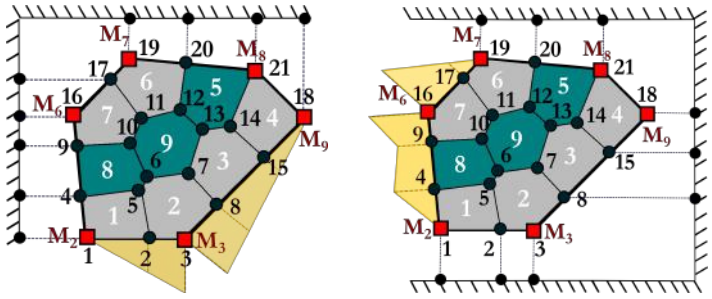

Figure 5: An example 6-noded coarse element ($\alpha = 2$) clustering $\mathrm{n}_{\mathrm{m}_{\mathrm{el}}}$=9 fine elements and $\mathrm{n}_{\mathrm{m}} = 21$ fine nodes. (a) Linear kinematical constraints are prescribed over edges $\Gamma_{\mathrm{M}_2\mathrm{M}_3}$ and $\Gamma_{\mathrm{M}_3\mathrm{M}_9}$, (b) Oscillatory kinematical constraints are prescribed over edges $\Gamma_{\mathrm{M}_7\mathrm{M}_6}$ and $\Gamma_{\mathrm{M}_6\mathrm{M}_2}$.

Remark 3. *The terminologies "Coarse-Element" and "Representative Volume Element (RVE)" are used interchangeably here. This is to remain consistent with the literature. A coarse-element, as employed in this work, is not truly representative of the entire domain, and should therefore not be confused with the classical notion of the RVE found in homogenization theory with scale separation.*

3.4. Governing multiscale equilibrium equations

The element-wise governing equations introduced in Eq. (11) are expressed in matrix form as

$$\begin{bmatrix} \mathbf{K}^{\mathrm{el},\alpha}_{\mathrm{m(i)}} & -\mathbf{Q}^{\mathrm{el},\alpha}_{\mathrm{m(i)}} \\ \mathbf{0} & \mathbf{H}^{\mathrm{el},\alpha}_{\mathrm{m(i)}} \end{bmatrix} \begin{Bmatrix} \mathbf{u}^{\alpha}_{\mathrm{m(i)}} \\ \mathbf{p}^{\alpha}_{\mathrm{m(i)}} \end{Bmatrix} + \begin{bmatrix} \mathbf{0} & \mathbf{0} \\ \mathbf{Q}^{\mathrm{el},\alpha\,T}_{\mathrm{m(i)}} & \mathbf{S}^{\mathrm{el},\alpha}_{\mathrm{m(i)}} \end{bmatrix} \begin{Bmatrix} \dot{\mathbf{u}}^{\alpha}_{\mathrm{m(i)}} \\ \dot{\mathbf{p}}^{\alpha}_{\mathrm{m(i)}} \end{Bmatrix} = \begin{bmatrix} \mathbf{f}^{\mathrm{u\ el},\alpha}_{\mathrm{m(i)}} \\ \mathbf{f}^{\mathrm{p\ el},\alpha}_{\mathrm{m(i)}} \end{bmatrix}. \quad (37)$$

where the state matrices $\mathbf{K}^{\mathrm{el},\alpha}_{\mathrm{m(i)}}$, $\mathbf{Q}^{\mathrm{el},\alpha}_{\mathrm{m(i)}}$, $\mathbf{H}^{\mathrm{el},\alpha}_{\mathrm{m(i)}}$, $\mathbf{S}^{\mathrm{el},\alpha}_{\mathrm{m(i)}}$ are evaluated using the VEM according to Eq. (29). The vectors $\mathbf{f}^{\mathrm{u\ el},\alpha}_{\mathrm{m(i)}}$ and $\mathbf{f}^{\mathrm{p\ el},\alpha}_{\mathrm{m(i)}}$ correspond to the nodal forces and outflows, respectively at the i^{th} micro-element.

Substituting the micro to macro mapping Eqs. (33) into Eq. (37) and pre-multiplying the first row-set of equations by $\mathbf{N}^{\mathrm{u}\,T}_{\mathrm{m}}$ and the second row-set by

$\mathbf{N}_{\mathrm{m}}^{\mathrm{p}\,T}$ the following equation is obtained

$$\begin{bmatrix} \mathbf{K}^{\mathrm{el}}_{\mathrm{M}(\alpha),\mathrm{m(i)}} & -\mathbf{Q}^{\mathrm{el}}_{\mathrm{M}(\alpha),\mathrm{m(i)}} \\ \mathbf{0} & \mathbf{H}^{\mathrm{el}}_{\mathrm{M}(\alpha),\mathrm{m(i)}} \end{bmatrix} \begin{Bmatrix} \mathbf{u}_{\mathrm{M}(\alpha)} \\ \mathbf{p}_{\mathrm{M}(\alpha)} \end{Bmatrix} + \begin{bmatrix} \mathbf{0} & \mathbf{0} \\ \mathbf{Q}^{\mathrm{el}\,T}_{\mathrm{M}(\alpha),\mathrm{m(i)}} & \mathbf{S}^{\mathrm{el}}_{\mathrm{M}(\alpha),\mathrm{m(i)}} \end{bmatrix} \begin{Bmatrix} \dot{\mathbf{u}}_{\mathrm{M}(\alpha)} \\ \dot{\mathbf{p}}_{\mathrm{M}(\alpha)} \end{Bmatrix} = \begin{bmatrix} \mathbf{f}^{\mathrm{u\,el}}_{\mathrm{M}(\alpha),\mathrm{m(i)}} \\ \mathbf{f}^{\mathrm{p\,el}}_{\mathrm{M}(\alpha),\mathrm{m(i)}} \end{bmatrix}, \tag{38}$$

where the stiffness and coupling matrices of the i^{th} micro-element mapped at the coarse element nodes are expressed as

$$\mathbf{K}^{\mathrm{el}}_{\mathrm{M}(\alpha),\mathrm{m(i)}} = \mathbf{N}^{\mathrm{u}\,T}_{\mathrm{m(i)}} \mathbf{K}^{\mathrm{el},\alpha}_{\mathrm{m(i)}} \mathbf{N}^{\mathrm{u}}_{\mathrm{m(i)}} \tag{39}$$

$$\mathbf{Q}^{\mathrm{el}}_{\mathrm{M}(\alpha),\mathrm{m(i)}} = \mathbf{N}^{\mathrm{u}\,T}_{\mathrm{m(i)}} \mathbf{Q}^{\mathrm{el},\alpha}_{\mathrm{m(i)}} \mathbf{N}^{\mathrm{p}}_{\mathrm{m(i)}}. \tag{40}$$

Furthermore, permeability and compressibility matrices are expressed as

$$\mathbf{H}^{\mathrm{el}}_{\mathrm{M}(\alpha),\mathrm{m(i)}} = \mathbf{N}^{\mathrm{p}\,T}_{\mathrm{m(i)}} \mathbf{H}^{\mathrm{el},\alpha}_{\mathrm{m(i)}} \mathbf{N}^{\mathrm{p}}_{\mathrm{m(i)}} \tag{41}$$

$$\mathbf{S}^{\mathrm{el}}_{\mathrm{M}(\alpha),\mathrm{m(i)}} = \mathbf{N}^{\mathrm{p}\,T}_{\mathrm{m(i)}} \mathbf{S}^{\mathrm{el},\alpha}_{\mathrm{m(i)}} \mathbf{N}^{\mathrm{p}}_{\mathrm{m(i)}}. \tag{42}$$

Finally, the forcing terms assume the following form

$$\mathbf{f}^{\mathrm{u\,el}}_{\mathrm{M}(\alpha),\mathrm{m(i)}} = \mathbf{N}^{\mathrm{u}\,T}_{\mathrm{m(i)}} \mathbf{f}^{\mathrm{u\,el},\alpha}_{\mathrm{m(i)}} \tag{43}$$

$$\mathbf{f}^{\mathrm{p\,el}}_{\mathrm{M}(\alpha),\mathrm{m(i)}} = \mathbf{N}^{\mathrm{p}\,T}_{\mathrm{m(i)}} \mathbf{f}^{\mathrm{p\,el},\alpha}_{\mathrm{m(i)}} \tag{44}$$

for the nodal forces and outflows, respectively.

In principle, the coarse-element equilibrium equations could be expressed in a form analogous to Eq. (37), i.e.,

$$\begin{bmatrix} \mathbf{K}^{\mathrm{el}}_{\mathrm{M}(\alpha)} & -\mathbf{Q}^{\mathrm{el}}_{\mathrm{M}(\alpha)} \\ \mathbf{0} & \mathbf{H}^{\mathrm{el}}_{\mathrm{M}(\alpha)} \end{bmatrix} \begin{Bmatrix} \mathbf{u}_{\mathrm{M}(\alpha)} \\ \mathbf{p}_{\mathrm{M}(\alpha)} \end{Bmatrix} + \begin{bmatrix} \mathbf{0} & \mathbf{0} \\ \mathbf{Q}^{\mathrm{el},T}_{\mathrm{M}(\alpha)} & \mathbf{S}^{\mathrm{el}}_{\mathrm{M}(\alpha)} \end{bmatrix} \begin{Bmatrix} \dot{\mathbf{u}}_{\mathrm{M}(\alpha)} \\ \dot{\mathbf{p}}_{\mathrm{M}(\alpha)} \end{Bmatrix} = \begin{bmatrix} \mathbf{f}^{\mathrm{u\,el}}_{\mathrm{M}(\alpha)} \\ \mathbf{f}^{\mathrm{p\,el}}_{\mathrm{M}(\alpha)} \end{bmatrix}, \tag{45}$$

where $\mathbf{K}^{\mathrm{el}}_{\mathrm{M}(\alpha)}$, $\mathbf{Q}^{\mathrm{el}}_{\mathrm{M}(\alpha)}$, $\mathbf{H}^{\mathrm{el}}_{\mathrm{M}(\alpha)}$, $\mathbf{S}^{\mathrm{el}}_{\mathrm{M}(\alpha)}$ denote the coarse-element state matrices and $\mathbf{f}^{\mathrm{u\,el}}_{\mathrm{M}(\alpha)}$, $\mathbf{f}^{\mathrm{p\,el}}_{\mathrm{M}(\alpha)}$ denote the coarse-element load vectors, respectively. Due to the heterogeneous material distribution at the fine scale, explicit expressions for these matrices do not exist. Yet, these can be evaluated on the basis of energy equivalence between the coarse element domain Eqs. (45) and the upscaled fine-element components Eqs. (39)-(44).

Considering Eq. (45), the internal energy associated with each operator is defined as

$$\mathrm{E}^{\mathrm{K}}_{\mathrm{int}} = \int\limits_{\mathcal{K}_{\mathrm{M}(\alpha)}} \boldsymbol{\varepsilon}^{T}_{\mathrm{M}}\, \mathbb{D}\, \boldsymbol{\varepsilon}_{\mathrm{M}}\, \mathrm{d}\mathcal{K} = \mathbf{u}^{T}_{\mathrm{M}(\alpha)} \mathbf{K}^{\mathrm{el}}_{\mathrm{M}(\alpha)} \mathbf{u}_{\mathrm{M}(\alpha)} \tag{46a}$$

$$\mathrm{E}^{\mathrm{Q}}_{\mathrm{int}} = \int\limits_{\mathcal{K}_{\mathrm{M}(\alpha)}} \mathrm{p}^{T}_{\mathrm{M}}\, \alpha_{\mathrm{B}} \mathbf{m}\, \boldsymbol{\varepsilon}_{\mathrm{M}}\, \mathrm{d}\mathcal{K} = \mathbf{p}^{T}_{\mathrm{M}(\alpha)} \mathbf{Q}^{\mathrm{el}}_{\mathrm{M}(\alpha)} \mathbf{u}_{\mathrm{M}(\alpha)} \tag{46b}$$

$$\mathrm{E}^{\mathrm{H}}_{\mathrm{int}} = \int\limits_{\mathcal{K}_{\mathrm{M}(\alpha)}} \nabla \mathrm{p}^{T}_{\mathrm{M}}\, \frac{\mathbf{k}}{\gamma_{\mathrm{f}}}\, \nabla \mathrm{p}_{\mathrm{M}}\, \mathrm{d}\mathcal{K} = \mathbf{p}^{T}_{\mathrm{M}(\alpha)} \mathbf{H}^{\mathrm{el}}_{\mathrm{M}(\alpha)} \mathbf{p}_{\mathrm{M}(\alpha)} \tag{46c}$$

$$\mathrm{E}^{\mathrm{S}}_{\mathrm{int}} = \int\limits_{\mathcal{K}_{\mathrm{M}(\alpha)}} \mathrm{p}^{T}_{\mathrm{M}}\, \mathrm{S}_{\varepsilon}\, \mathrm{p}_{\mathrm{M}}\, \mathrm{d}\mathcal{K} = \mathbf{p}^{T}_{\mathrm{M}(\alpha)} \mathbf{S}^{\mathrm{el}}_{\mathrm{M}(\alpha)} \mathbf{p}_{\mathrm{M}(\alpha)} \tag{46d}$$

where $\boldsymbol{\varepsilon}_{\mathrm{M}}$ and p_{M} correspond to the strain and pressure fields defined over the coarse element domain.

The internal energy of the RVE is also additively decomposed into the contributions of its underlying fine-elements, i.e.,

$$\mathrm{E}^{\mathrm{K}}_{\mathrm{int}} = \sum_{\mathrm{i}=1}^{\mathrm{n}_{\mathrm{m}_{\mathrm{el}}}} \int\limits_{\mathcal{K}_{\mathrm{m(i)}}} \boldsymbol{\varepsilon}^{T}_{\mathrm{m(i)}}\, \mathbb{D}\, \boldsymbol{\varepsilon}_{\mathrm{m(i)}}\, \mathrm{d}\mathcal{K} = \sum_{\mathrm{i}=1}^{\mathrm{n}_{\mathrm{m}_{\mathrm{el}}}} \mathbf{u}^{\alpha\, T}_{\mathrm{m(i)}} \mathbf{K}^{\mathrm{el},\alpha}_{\mathrm{m(i)}} \mathbf{u}^{\alpha}_{\mathrm{m(i)}} \tag{47a}$$

$$\mathrm{E}^{\mathrm{Q}}_{\mathrm{int}} = \sum_{\mathrm{i}=1}^{\mathrm{n}_{\mathrm{m}_{\mathrm{el}}}} \int\limits_{\mathcal{K}_{\mathrm{m(i)}}} \mathrm{p}^{T}_{\mathrm{m(i)}}\, \alpha_{\mathrm{B}} \mathbf{m}\, \boldsymbol{\varepsilon}_{\mathrm{m(i)}}\, \mathrm{d}\mathcal{K} = \sum_{\mathrm{i}=1}^{\mathrm{n}_{\mathrm{m}_{\mathrm{el}}}} \mathbf{p}^{\alpha\, T}_{\mathrm{m(i)}} \mathbf{Q}^{\mathrm{el},\alpha}_{\mathrm{m(i)}} \mathbf{u}^{\alpha}_{\mathrm{m(i)}} \tag{47b}$$

$$\mathrm{E}^{\mathrm{H}}_{\mathrm{int}} = \sum_{\mathrm{i}=1}^{\mathrm{n}_{\mathrm{m}_{\mathrm{el}}}} \int\limits_{\mathcal{K}_{\mathrm{m(i)}}} \nabla \mathrm{p}^{T}_{\mathrm{m(i)}}\, \frac{\mathbf{k}}{\gamma_{\mathrm{f}}}\, \nabla \mathrm{p}_{\mathrm{m(i)}}\, \mathrm{d}\mathcal{K} = \sum_{\mathrm{i}=1}^{\mathrm{n}_{\mathrm{m}_{\mathrm{el}}}} \mathbf{p}^{\alpha\, T}_{\mathrm{m(i)}} \mathbf{H}^{\mathrm{el},\alpha}_{\mathrm{m(i)}} \mathbf{p}^{\alpha}_{\mathrm{m(i)}} \tag{47c}$$

$$\mathrm{E}^{\mathrm{S}}_{\mathrm{int}} = \sum_{\mathrm{i}=1}^{\mathrm{n}_{\mathrm{m}_{\mathrm{el}}}} \int\limits_{\mathcal{K}_{\mathrm{m(i)}}} \mathrm{p}^{T}_{\mathrm{m(i)}}\, \mathrm{S}_{\varepsilon}\, \mathrm{p}_{\mathrm{m(i)}}\, \mathrm{d}\mathcal{K} = \sum_{\mathrm{i}=1}^{\mathrm{n}_{\mathrm{m}_{\mathrm{el}}}} \mathbf{p}^{\alpha\, T}_{\mathrm{m(i)}} \mathbf{S}^{\mathrm{el},\alpha}_{\mathrm{m(i)}} \mathbf{p}^{\alpha}_{\mathrm{m(i)}} \tag{47d}$$

Equating Eqs. (46a) and (47a) the following expression is derived

$$\mathbf{u}^{T}_{\mathrm{M}(\alpha)} \mathbf{K}^{\mathrm{el}}_{\mathrm{M}(\alpha)} \mathbf{u}_{\mathrm{M}(\alpha)} = \mathbf{u}^{T}_{\mathrm{M}(\alpha)} \sum_{\mathrm{i}=1}^{\mathrm{n}_{\mathrm{m}_{\mathrm{el}}}} \Big(\mathbf{N}^{\mathrm{u}\, T}_{\mathrm{m(i)}} \mathbf{K}^{\mathrm{el},\alpha}_{\mathrm{m(i)}} \mathbf{N}^{\mathrm{u}}_{\mathrm{m(i)}} \Big) \mathbf{u}_{\mathrm{M}(\alpha)}, \tag{48}$$

that holds if and only if

$$\mathbf{K}^{\mathrm{el}}_{\mathrm{M}(\alpha)} = \sum_{\mathrm{i}=1}^{\mathrm{n}_{\mathrm{m}_{\mathrm{el}}}} \mathbf{K}^{\mathrm{el}}_{\mathrm{M}(\alpha),\mathrm{m(i)}} \tag{49}$$

Hence, Eq. (49) provides the reduced order stiffness matrix of the coarse element that however comprises stiffness contributions from the underlying micro-elements.

The upscaled expressions for the coupling, permeability, and compressibility matrices are derived in a similar manner as

$$\mathbf{Q}^{\mathrm{el}}_{\mathrm{M}(\alpha)} = \sum_{\mathrm{i}=1}^{\mathrm{n_{m_{el}}}} \mathbf{Q}^{\mathrm{el}}_{\mathrm{M}(\alpha),\mathrm{m(i)}}, \tag{50}$$

$$\mathbf{H}^{\mathrm{el}}_{\mathrm{M}(\alpha)} = \sum_{\mathrm{i}=1}^{\mathrm{n_{m_{el}}}} \mathbf{H}^{\mathrm{el}}_{\mathrm{M}(\alpha),\mathrm{m(i)}}, \tag{51}$$

and

$$\mathbf{S}^{\mathrm{el}}_{\mathrm{M}(\alpha)} = \sum_{\mathrm{i}=1}^{\mathrm{n_{m_{el}}}} \mathbf{S}^{\mathrm{el}}_{\mathrm{M}(\alpha),\mathrm{m(i)}}, \tag{52}$$

respectively.

Finally, the upscaled load and outflow vectors are

$$\mathbf{f}^{\mathrm{u\ el}}_{\mathrm{M}(\alpha)} = \sum_{\mathrm{i}=1}^{\mathrm{n_{m_{el}}}} \mathbf{f}^{\mathrm{u\ el}}_{\mathrm{M}(\alpha),\mathrm{m(i)}} \tag{53}$$

and

$$\mathbf{f}^{\mathrm{p\ el}}_{\mathrm{M}(\alpha)} = \sum_{\mathrm{i}=1}^{\mathrm{n_{m_{el}}}} \mathbf{f}^{\mathrm{p\ el}}_{\mathrm{M}(\alpha),\mathrm{m(i)}}, \tag{54}$$

respectively (see, also, [24]).

The coarse element state and load matrices defined in Eqs. (49)-54 can then be assembled using a direct assembly approach to derive the reduced order structure matrices and corresponding forcing vectors

$$\mathbf{K}_{\mathrm{M}} = \mathop{\mathrm{A}}_{\alpha=1}^{\mathrm{n_{M_{el}}}} \mathbf{K}^{\mathrm{el}}_{\mathrm{M}(\alpha)}, \quad \mathbf{Q}_{\mathrm{M}} = \mathop{\mathrm{A}}_{\alpha=1}^{\mathrm{n_{M_{el}}}} \mathbf{Q}^{\mathrm{el}}_{\mathrm{M}(\alpha)}, \quad \mathbf{f}^{\mathrm{u}}_{\mathrm{M}} = \mathop{\mathrm{A}}_{\alpha=1}^{\mathrm{n_{M_{el}}}} \mathbf{f}^{\mathrm{u,el}}_{\mathrm{M}(\alpha)}, \tag{55a}$$

$$\mathbf{H}_{\mathrm{M}} = \mathop{\mathrm{A}}_{\alpha=1}^{\mathrm{n_{M_{el}}}} \mathbf{H}^{\mathrm{el}}_{\mathrm{M}(\alpha)}, \quad \mathbf{S}_{\mathrm{M}} = \mathop{\mathrm{A}}_{\alpha=1}^{\mathrm{n_{M_{el}}}} \mathbf{S}^{\mathrm{el}}_{\mathrm{M}(\alpha)}, \quad \mathbf{f}^{\mathrm{p}}_{\mathrm{M}} = \mathop{\mathrm{A}}_{\alpha=1}^{\mathrm{n_{M_{el}}}} \mathbf{f}^{\mathrm{p,el}}_{\mathrm{M}(\alpha)}. \tag{55b}$$

Hence, the upscaled governing equations assume the following form

$$\begin{bmatrix} \mathbf{K}_{\mathrm{M}} & -\mathbf{Q}_{\mathrm{M}} \\ \mathbf{0} & \mathbf{H}_{\mathrm{M}} \end{bmatrix} \begin{Bmatrix} \mathbf{u}_{\mathrm{M}} \\ \mathbf{p}_{\mathrm{M}} \end{Bmatrix} + \begin{bmatrix} \mathbf{0} & \mathbf{0} \\ \mathbf{Q}^{T}_{\mathrm{M}} & \mathbf{S}_{\mathrm{M}} \end{bmatrix} \begin{Bmatrix} \dot{\mathbf{u}}_{\mathrm{M}} \\ \dot{\mathbf{p}}_{\mathrm{M}} \end{Bmatrix} = \begin{bmatrix} \mathbf{f}^{\mathrm{u}}_{\mathrm{M}} \\ \mathbf{f}^{\mathrm{p}}_{\mathrm{M}} \end{bmatrix}, \tag{56}$$

The unknown field variables $\mathbf{u}_{\mathrm{M}}$ and $\mathbf{p}_{\mathrm{M}}$ represent the global coarse-nodal displacements and vectors, respectively.

The algorithmic implementation of the multiscale virtual element method vis-a-vis the assembly of the discretized governing equations at the coarse scale is summarized in Algorithm 1.

Algorithm 1 Upscaling procedure performed for solid and fluid phases

Result: Global coarse scale stiffness matrices $\mathbf{K}_{\mathrm{M}}$, $\mathbf{H}_{\mathrm{M}}$ and load vectors $\mathbf{f}^{\mathbf{u}}_{\mathrm{M}}$, $\mathbf{f}^{\mathrm{p}}_{\mathrm{M}}$

for $\Omega_{M(\alpha)},\ 1 \leq \alpha \leq n_{M_{el}}$ **do**

1. Compute RVE stiffnesses,
   (a) Solid phase: $\mathbf{K}^{\alpha}_{\mathrm{m}}$ with $\mathbf{K}^{\alpha}_{\mathrm{m}} = \sum_{\mathrm{i}=1}^{\mathrm{n_{m_{el}}}} \mathbf{K}^{\mathrm{el},\alpha}_{\mathrm{m(i)}}$,
   (b) Fluid phase: $\mathbf{H}^{\alpha}_{\mathrm{m}}$ with $\mathbf{H}^{\alpha}_{\mathrm{m}} = \sum_{\mathrm{i}=1}^{\mathrm{n_{m_{el}}}} \mathbf{H}^{\mathrm{el},\alpha}_{\mathrm{m(i)}}$
2. Compute multiscale basis functions using kinematic constraints with
   (a) Solid phase: $\mathbf{N}^{\mathrm{u}}_{\mathrm{m}} : \mathbf{K}^{\alpha}_{\mathrm{m}}\mathbf{u}^{\alpha}_{\mathrm{m}} = \mathbf{0}$, where $\mathbf{u}^{\alpha}_{\mathrm{m}} \equiv \mathbf{N}^{\mathrm{u}}_{\mathrm{m}}$,
   (b) Fluid phase: $\mathbf{N}^{\mathrm{p}}_{\mathrm{m}} : \mathbf{H}^{\alpha}_{\mathrm{m}}\mathbf{p}^{\alpha}_{\mathrm{m}} = \mathbf{0}$, where $\mathbf{p}^{\alpha}_{\mathrm{m}} \equiv \mathbf{N}^{\mathrm{p}}_{\mathrm{m}}$
3. Compute multiscale contributions with
   (a) Solid phase: $\mathbf{K}^{\mathrm{el}}_{\mathrm{M}(\alpha),\mathrm{m(i)}} = \mathbf{N}^{\mathrm{u}\,T}_{\mathrm{m(i)}}\mathbf{K}^{\mathrm{el},\alpha}_{\mathrm{m(i)}}\mathbf{N}^{\mathrm{u}}_{\mathrm{m(i)}}$ and $\mathbf{f}^{\mathrm{u,el}}_{\mathrm{M}(\alpha),\mathrm{m(i)}} = \mathbf{N}^{\mathrm{u}\,T}_{\mathrm{m(i)}}\mathbf{f}^{\mathrm{u\,el},\alpha}_{\mathrm{m(i)}}$,
   (b) Fluid phase: $\mathbf{H}^{\mathrm{el}}_{\mathrm{M}(\alpha),\mathrm{m(i)}} = \mathbf{N}^{\mathrm{p}\,T}_{\mathrm{m(i)}}\mathbf{H}^{\mathrm{el},\alpha}_{\mathrm{m(i)}}\mathbf{N}^{\mathrm{p}}_{\mathrm{m(i)}}$ and $\mathbf{f}^{\mathrm{p,el}}_{\mathrm{M}(\alpha),\mathrm{m(i)}} = \mathbf{N}^{\mathrm{p},T}_{\mathrm{m(i)}}\mathbf{f}^{\mathrm{p\,el},\alpha}_{\mathrm{m(i)}}$
4. Assemble coarse-element stiffnesses with
   (a) Solid phase: $\mathbf{K}^{\mathrm{el}}_{\mathrm{M}(\alpha)} = \sum_{\mathrm{i}=1}^{\mathrm{n_{m_{el}}}} \mathbf{K}^{\mathrm{el}}_{\mathrm{M}(\alpha),\mathrm{m(i)}}$, and $\mathbf{f}^{\mathbf{u},\mathrm{el}}_{\mathrm{M}(\alpha)} = \sum_{\mathrm{i}=1}^{\mathrm{n_{m_{el}}}} \mathbf{f}^{\mathbf{u},\mathrm{el}}_{\mathrm{M}(\alpha),\mathrm{m(i)}}$,
   (b) Fluid phase: $\mathbf{H}^{\mathrm{el}}_{\mathrm{M}(\alpha)} = \sum_{\mathrm{i}=1}^{\mathrm{n_{m_{el}}}} \mathbf{H}^{\mathrm{el}}_{\mathrm{M}(\alpha),\mathrm{m(i)}}$, and $\mathbf{f}^{\mathbf{p},\mathrm{el}}_{\mathrm{M}(\alpha)} = \sum_{\mathrm{i}=1}^{\mathrm{n_{m_{el}}}} \mathbf{f}^{\mathrm{p,el}}_{\mathrm{M}(\alpha),\mathrm{m(i)}}$,

end

Assemble global coarse stiffness matrix and load vector with

(a) Solid phase: $\mathbf{K}_{\mathrm{M}} = \mathrm{A}_{\alpha=1}^{\mathrm{n_{M_{el}}}}\,\mathbf{K}^{\mathrm{el}}_{\mathrm{M}(\alpha)}$ and $\mathbf{f}^{\mathbf{u}}_{\mathrm{M}} = \mathrm{A}_{\alpha=1}^{\mathrm{n_{M_{el}}}}\,\mathbf{f}^{\mathbf{u},\mathrm{el}}_{\mathrm{M}(\alpha)}$

(b) Fluid phase: $\mathbf{H}_{\mathrm{M}} = \mathrm{A}_{\alpha=1}^{\mathrm{n_{M_{el}}}}\,\mathbf{H}^{\mathrm{el}}_{\mathrm{M}(\alpha)}$ and $\mathbf{f}^{\mathrm{p}}_{\mathrm{M}} = \mathrm{A}_{\alpha=1}^{\mathrm{n_{M_{el}}}}\,\mathbf{f}^{\mathrm{p,el}}_{\mathrm{M}(\alpha)}$

3.5. Solution procedure at the coarse scale

Eq. (56) is a system of first order differential/ algebraic equations with respect to time of the following generic form

$$\mathbf{A}\,\dot{\mathbf{X}} + \mathbf{B}\,\mathbf{X} = \mathbf{F}, \tag{57}$$

where $\mathbf{X} = \left\{\mathbf{u}_{\mathrm{M}}, \quad \mathbf{p}_{\mathrm{M}}\right\}^{T}$. The quantities $\mathbf{A}$, $\mathbf{B}$ and $\mathbf{F}$ can be obtained from Eq. (56) by inspection.

In this work, a theta rule time discretization scheme is employed to obtain solution states at each time step. Assuming that the time domain is discretized into a finite number of $N_t + 1$ points, i.e., $t_0 < t_1 \cdots < t_n < t_{n+1} < \cdots < t_{N_t}$ the solution vector $\mathbf{X}$ and it's time derivative $\dot{\mathbf{X}}$ are defined as

$$\mathbf{X}_{\mathrm{n}+\theta} = (1-\theta)\mathbf{X}_{\mathrm{n}} + \theta\mathbf{X}_{\mathrm{n}+1} \tag{58}$$

and

$$\dot{\mathbf{X}}_{\mathrm{n}+\theta} = \frac{\mathbf{X}_{\mathrm{n}+1} - \mathbf{X}_{\mathrm{n}}}{\Delta t}, \tag{59}$$

respectively, where $\Delta\mathrm{t}$ is the time increment and θ is the implicitness parameter $0 \leq \theta \leq 1$. The vectors $\mathbf{X}_{\mathrm{n}}$ and $\mathbf{X}_{\mathrm{n}+1}$ denote the state vectors at time $\mathrm{t_n}$ and $\mathrm{t_{n+1}}$, respectively.

Substituting Eqs. (58) and (59) into Eq. (57) gives rise to the following time marching scheme

$$\tilde{\mathbf{A}}\mathbf{X}_{\mathrm{n}+1} = \tilde{\mathbf{B}}\mathbf{X}_{\mathrm{n}} + \Delta t\mathbf{F}_{\mathrm{n}+\theta}, \tag{60}$$

where $\tilde{\mathbf{A}}$ and $\tilde{\mathbf{B}}$ are the effective state matrices, which after the necessary algebraic manipulation assume the following form, i.e.,

$$\tilde{\mathbf{A}} = \begin{bmatrix} \theta\mathbf{K}_{\mathrm{M}} & -\theta\mathbf{Q}_{\mathrm{M}} \\ \mathbf{Q}_{\mathrm{M}}^{T} & \mathbf{S}_{\mathrm{M}} + \Delta\mathrm{t}\theta\mathbf{H}_{\mathrm{M}} \end{bmatrix}_{\mathrm{n}+\theta} \tag{61}$$

and

$$\tilde{\mathbf{B}} = \begin{bmatrix} (\theta-1)\mathbf{K}_{\mathrm{M}} & (1-\theta)\mathbf{Q}_{\mathrm{M}} \\ \mathbf{Q}_{\mathrm{M}}^{T} & \mathbf{S}_{\mathrm{M}} - (1-\theta)\Delta\mathrm{t}\mathbf{H}_{\mathrm{M}} \end{bmatrix}_{\mathrm{n}+\theta}, \tag{62}$$

respectively and the discretized forcing vector $\mathbf{F}_{\mathrm{n}+\theta} = \left\{\mathbf{f}_{\mathrm{M}}^{\mathrm{u}} \quad \mathbf{f}_{\mathrm{M}}^{\mathrm{p}}\right\}^{T}$

A central difference scheme, $\theta = \frac{1}{2}$ is adopted in this work. Since such a scheme is conditionally stable, one should exercise caution in choosing appropriate spatial and temporal time discretization steps.

3.6. Downscaling

The fine-scale displacements and pressures at each time-step can be evaluated from the solution of Eq. (60) by employing the following down-scaling procedure. The coarse element-wise displacements and pressures are first extracted at the desired time steps from $\{\mathbf{u}_{\mathrm{M}}\}_{\mathrm{n}}$ and $\{\mathbf{p}_{\mathrm{M}}\}_{\mathrm{n}}$, respectively. These values are now stored in the vectors of coarse-nodal displacements $\mathbf{u}_{\mathrm{M}(\alpha)}$ and pressures $\mathbf{p}_{\mathrm{M}(\alpha)},\ \alpha = 1 \dots \mathrm{n}_{\mathrm{M_{el}}}$, respectively. The displacements and pressures associated with the i^{th} fine-element in the α^{th} coarse-element / RVE can be evaluated using Eq. (33). Derivative quantities, like strains and stresses associated with the fine-scale elements can now be computed:

$$\boldsymbol{\varepsilon}^{\alpha}_{\mathrm{m(i)}} = \mathbf{B}^{\boldsymbol{\varepsilon}} \mathbf{u}^{\alpha}_{\mathrm{m(i)}}, \quad \boldsymbol{\sigma}^{\alpha}_{\mathrm{m(i)}} = \mathbb{D}\, \boldsymbol{\varepsilon}^{\alpha}_{\mathrm{m(i)}}, \tag{63}$$

Similarly, the derivative quantities for the fluid phase, i.e., the pressure flux and specific discharge, can be evaluated

$$\nabla \mathbf{p}^{\alpha}_{\mathrm{m(i)}} = \mathbf{B}^{\nabla} \mathbf{p}^{\alpha}_{\mathrm{m(i)}}, \quad \mathbf{q}^{\alpha}_{\mathrm{m(i)}} = -\frac{\mathbf{k}}{\gamma_w} \nabla \mathbf{p}^{\alpha}_{\mathrm{m(i)}}. \tag{64}$$

The terms $\mathbf{B}^{\boldsymbol{\varepsilon}}$ and $\mathbf{B}^{\nabla}$ are VEM based strain and gradient matrices, respectively. They are described fully in Appendix B.

The process flow of the CMsVEM is graphically shown in Fig. 6.

4. Numerical Examples

In the following, we examine the performance of the CMsVEM in terms of accuracy and computational efficiency, through three numerical examples. A first-order VEM ($k = 1$) is used in all cases. The element-types used are illustrated in Fig. 7. The centroidal Voronoi tesselations (CVT) shown in Fig. 7b are generated using Polymesher [82].

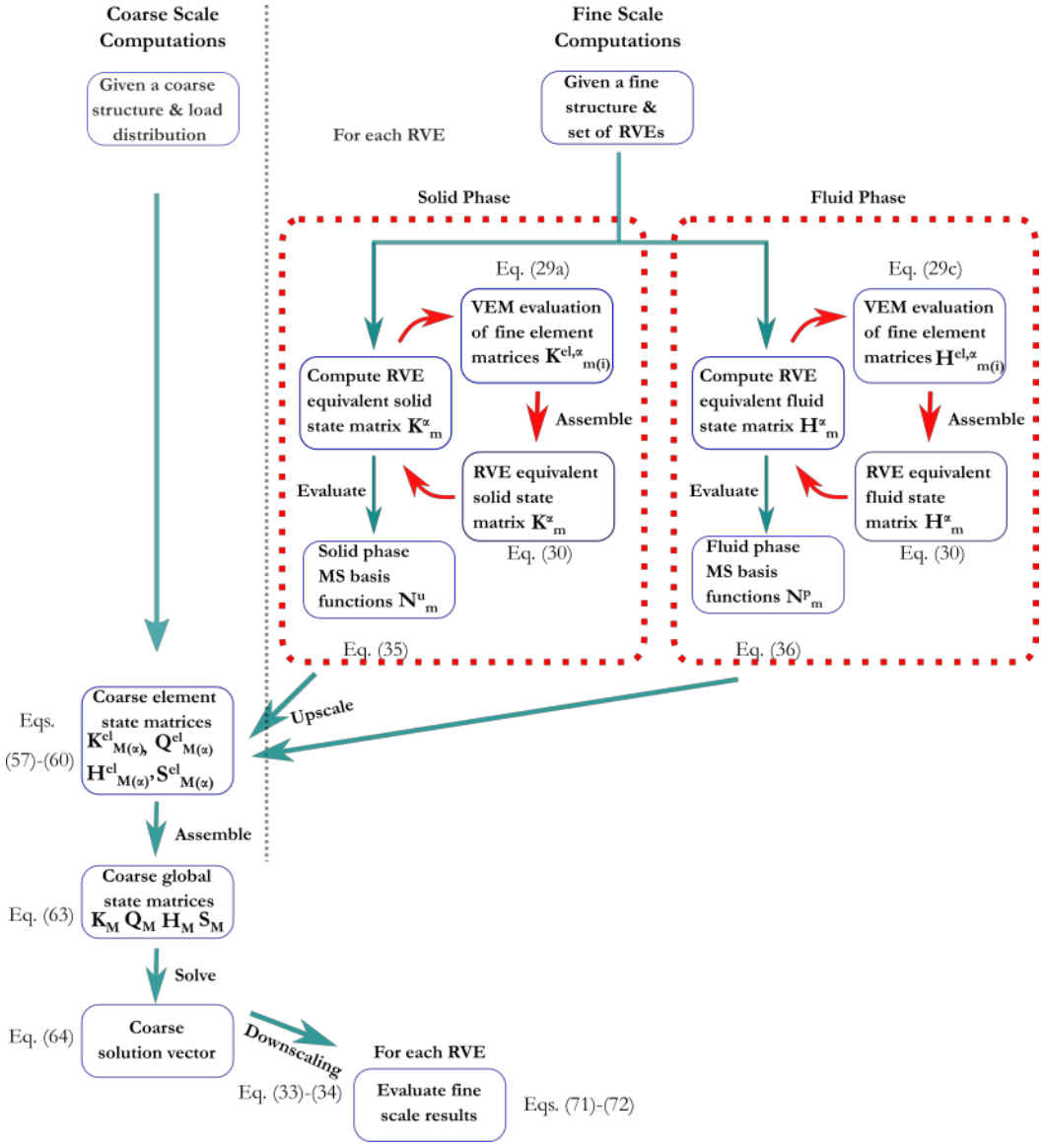

Figure 6: Process flow of the Coupled Multiscale Virtual Element procedure.

The accuracy of the displacement and stress/strain approximations is quantified through the relative $\mathcal{L}_2$ norm and the $\mathcal{H}_1$ semi-norm, respectively as follows:

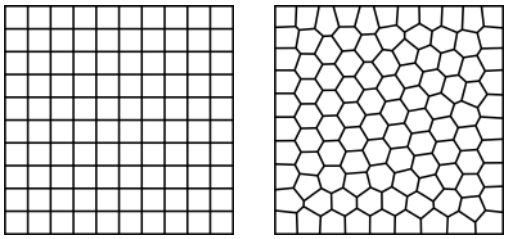

(a) 100 QUAD elements (b) 100 CVT elements

Figure 7: Mesh types used

$$||\mathbf{u}_h^{\mathcal{Q}} - \mathbf{u}_{ref}^{\mathcal{Q}}||_{\mathcal{L}_2} = \sqrt{\frac{1}{n_{\mathcal{Q}_{el}}} \sum_{i=1}^{n_{\mathcal{Q}_{el}}} \frac{\langle \mathbf{u}_{h(i)}^{\mathcal{Q}} - \mathbf{u}_{ref(i)}^{\mathcal{Q}}, \mathbf{u}_{h(i)}^{\mathcal{Q}} - \mathbf{u}_{ref(i)}^{\mathcal{Q}} \rangle}{\langle \mathbf{u}_{ref(i)}^{\mathcal{Q}}, \mathbf{u}_{ref(i)}^{\mathcal{Q}} \rangle}} \tag{65a}$$

$$||\mathbf{u}_h^{\mathcal{Q}} - \mathbf{u}_{ref}^{\mathcal{Q}}||_{\mathcal{H}_1} = \sqrt{\frac{1}{n_{\mathcal{Q}_{el}}} \sum_{i=1}^{n_{\mathcal{Q}_{el}}} \frac{\langle \boldsymbol{\varepsilon}(\mathbf{u}_{h(i)}^{\mathcal{Q}}) - \boldsymbol{\varepsilon}(\mathbf{u}_{ref(i)}^{\mathcal{Q}}), \boldsymbol{\sigma}(\mathbf{u}_{h(i)}^{\mathcal{Q}}) - \boldsymbol{\sigma}(\mathbf{u}_{ref(i)}^{\mathcal{Q}}) \rangle}{\langle \boldsymbol{\varepsilon}(\mathbf{u}_{ref(i)}^{\mathcal{Q}}), \boldsymbol{\sigma}(\mathbf{u}_{ref(i)}^{\mathcal{Q}}) \rangle}} \tag{65b}$$

Similarly, the accuracy of the pressure and the pressure flux/specific discharge approximations is quantified as

$$||\mathbf{p}_h^{\mathcal{Q}} - \mathbf{p}_{ref}^{\mathcal{Q}}||_{\mathcal{L}_2} = \sqrt{\frac{1}{n_{\mathcal{Q}_{el}}} \sum_{i=1}^{n_{\mathcal{Q}_{el}}} \frac{\langle \mathbf{p}_{h(i)}^{\mathcal{Q}} - \mathbf{p}_{ref(i)}^{\mathcal{Q}}, \mathbf{p}_{h(i)}^{\mathcal{Q}} - \mathbf{p}_{ref(i)}^{\mathcal{Q}} \rangle}{\langle \mathbf{p}_{ref(i)}^{\mathcal{Q}}, \mathbf{p}_{ref(i)}^{\mathcal{Q}} \rangle}} \tag{66a}$$

$$||\mathbf{p}_h^{\mathcal{Q}} - \mathbf{p}_{ref}^{\mathcal{Q}}||_{\mathcal{H}_1} = \sqrt{\frac{1}{n_{\mathcal{Q}_{el}}} \sum_{i=1}^{n_{\mathcal{Q}_{el}}} \frac{\langle \nabla \mathbf{p}_{h(i)}^{\mathcal{Q}} - \nabla \mathbf{p}_{ref(i)}^{\mathcal{Q}}, \mathbf{q}(\mathbf{p}_{h(i)}^{\mathcal{Q}}) - \mathbf{q}(\mathbf{p}_{ref(i)}^{\mathcal{Q}}) \rangle}{\langle \nabla \mathbf{p}_{ref(i)}^{\mathcal{Q}}, \mathbf{q}(\mathbf{p}_{ref(i)}^{\mathcal{Q}}) \rangle}}. \tag{66b}$$

To enable fair comparisons the relative $\mathcal{L}_2$ and $\mathcal{H}_1$ error norms are computed over a query mesh with $n_{\mathcal{Q}_{el}}$ elements unless stated otherwise. The terms $\mathbf{u}_h^{\mathcal{Q}}$, $\mathbf{p}_h^{\mathcal{Q}}$, $\mathbf{u}_{ref}^{\mathcal{Q}}$ and $\mathbf{p}_{ref}^{\mathcal{Q}}$ denote the numerically evaluated and reference displacements and pressures, interpolated at the nodes of the query mesh $\mathcal{Q}$, respectively. The operator $\langle \cdot, \cdot \rangle$ represents the scalar product. All reference solutions $\mathbf{u}_h$ and $\mathbf{p}_h$ are obtained through finely discretized VEM solutions. All solutions were performed using our in-house source codes developed in Matlab.

4.1. Porous domain with cavity

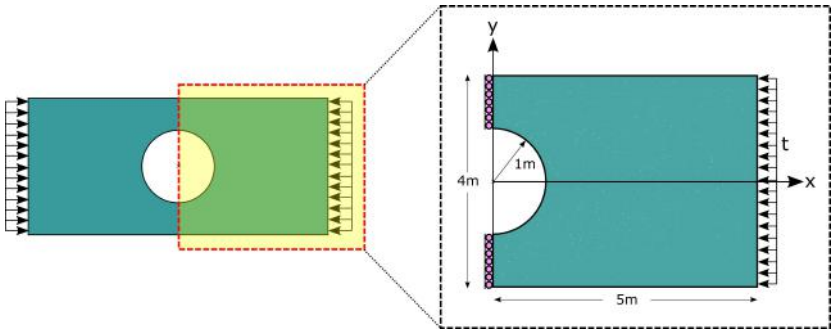

Figure 8: Geometry and boundary conditions of a porous domain with circular cavity

A rectangular porous domain with dimensions $10m \times 4m$ is considered, with a cavity of radius $R = 1m$ as shown in Fig. 8. Only half the domain is analysed due to symmetry. The boundary conditions are also shown in Fig. 8. The right edge is exposed to air and maintains a pressure $p = 0$. Null flow conditions are imposed at all boundaries, i.e., $\nabla p \cdot \mathbf{n} = 0$. A compressive load denoted by $\mathbf{t} = \left[t_x, 0\right]^T$, where $t_x = 75$ kN/m is incrementally applied on the right edge of the domain. The loading history is shown in Fig. 9. A homogeneous material

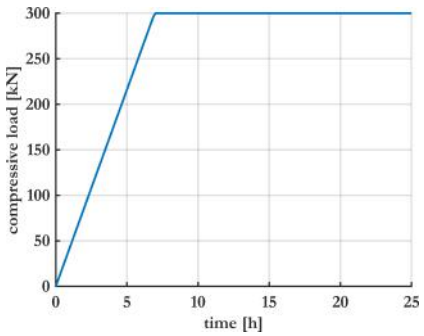

Figure 9: Compressive loading history

is assumed over the entire domain and the corresponding material parameters used are summarized in Table 3.

Three discretization schemes are used as shown in Fig. 10 and summarized in Table 4. Mesh 1 (Fig. 10a) is a pure VEM mesh of CVT elements with an average

Parameter	E	ν	γ_{f}	$\mathrm{K_s}$	$\mathrm{K_f}$	$\mathbf{g}$	ρ_{s}	ρ_{f}	n	α_B
	[MPa]	[/]	$[\mathrm{Pa \cdot s}]$	[Pa]	[Pa]	$[\mathrm{m \cdot s^{-2}}]$	$\mathrm{kg \cdot m^{-3}}$	$\mathrm{kg \cdot m^{-3}}$	[/]	[/]
Value	5	0.2	10^{-3}	3×10^4	10^4	0	10^3	10^3	0.2	1

Table 3: Homogeneous material parameters used

Label	**Full Mesh**	**Multiscale Mesh**	
	[-]	Macro	Micro
Mesh 1	$\mathrm{n_{el}} = 2500$	-	-
Mesh 2	$\mathrm{n_{el}} = 2500$	$\mathrm{n_{M_{el}}} = 50$	$\mathrm{n_{m_{el}}} = 50$
Mesh 3	$\mathrm{n_{el}} = 2500$	$\mathrm{n_{M_{el}}} = 250$	$\mathrm{n_{m_{el}}} = 10$

Table 4: Discretization scheme specifications

diameter $h = 0.1076m$. Mesh 2 (Fig. 10b) is a multiscale mesh comprising 50 coarse CVT elements of average diameter $h = 0.7880m$. Each coarse element clusters 50 fine CVT elements. Mesh 3 (Fig. 10c) is also a multiscale mesh consisting of 250 coarse CVT elements of average diameter $h = 0.5543m$. Here, each coarse element clusters 10 fine CVT elements.

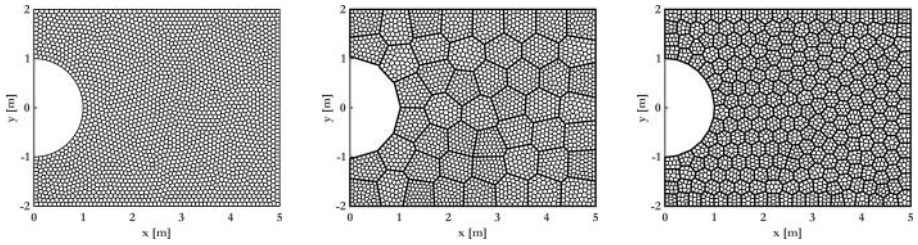

(a) (b) (c)

Figure 10: (a) Mesh 1, (b) Mesh 2, (c) Mesh 3.

4.1.1. Field contours

In all cases, the maximum pore-fluid pressures occur at $t_i = 6.83$ hours, $i = 42$; these are shown in Fig. 11. The corresponding displacement contours

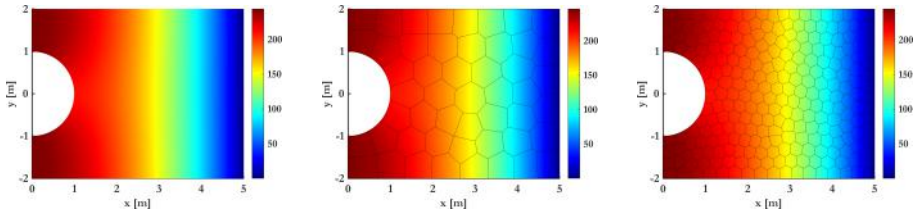

(a) Mesh 1 (b) Mesh 2 (c) Mesh 3

Figure 11: p: pressures of pore fluid at $t_i = 6.83$ hours, $i = 42$

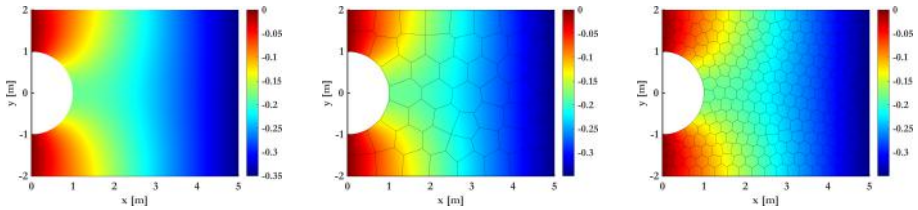

(a) Mesh 1 (b) Mesh 2 (c) Mesh 3

Figure 12: u_x: x-Displacements of solid skeleton at $t_i = 6.83$ hours, $i = 42$

u_x and u_y are shown in Figs. 12 and 13, respectively. The pressures computed by the method over Mesh 2 and Mesh 3 are nearly identical to the reference VEM solution, as illustrated in Fig. 11. Similarly, the displacements u_x and u_y evaluated over Meshes 2 and 3 are found to be equivalent to the associated Mesh 1 contours. This can be seen from Figs. 12 and 13, respectively. It can be concluded from this that the CMsVEM procedure over Mesh 2 proves sufficient for computing primary quantities, while offering stark reductions in computational complexity.

The stress contours σ_{xx}, σ_{yy}, σ_{xy} are illustrated in Figs. 14 , 15 , and 16, respectively. The Darcy velocities v_x and v_y are shown in Figs. 17 and 18, respectively. The Darcy velocity is evaluated through the following expression:

$$\mathbf{v} = \mathbf{q}/n, \tag{67}$$

where n denotes the porosity and $\mathbf{q}$ is the Darcy flux computed using Eq. (64).

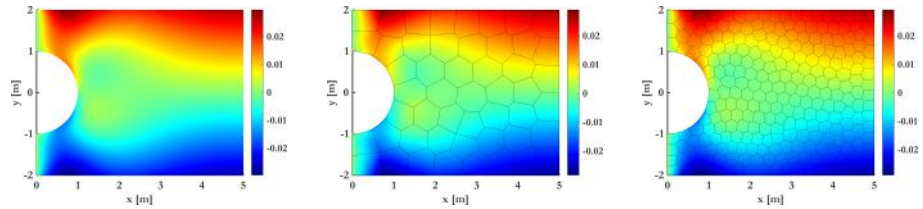

(a) Mesh 1 (b) Mesh 2 (c) Mesh 3

Figure 13: u_y: y-Displacements of solid skeleton at $t_i = 6.83$ hours, $i = 42$

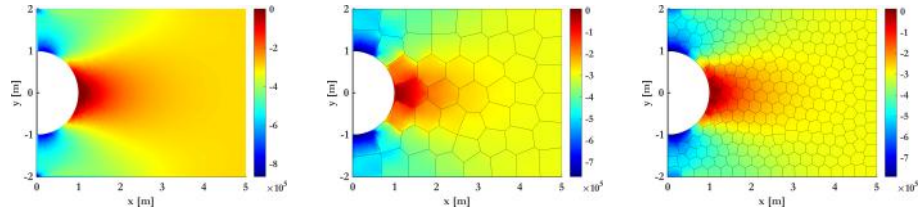

(a) Mesh 1 (b) Mesh 2 (c) Mesh 3

Figure 14: σ_{xx}: Stresses of solid skeleton at $t_i = 6.83$ hours, $i = 42$

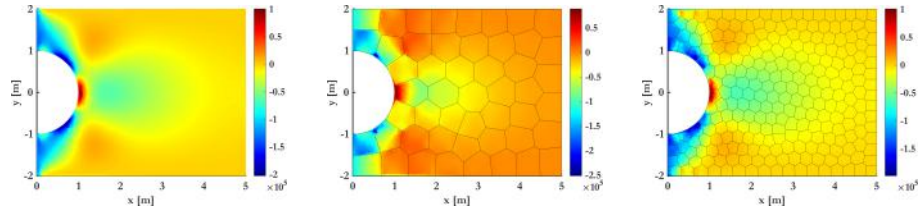

(a) Mesh 1 (b) Mesh 2 (c) Mesh 3

Figure 15: σ_{yy}: Stresses of solid skeleton at $t_i = 6.83$ hours, $i = 42$

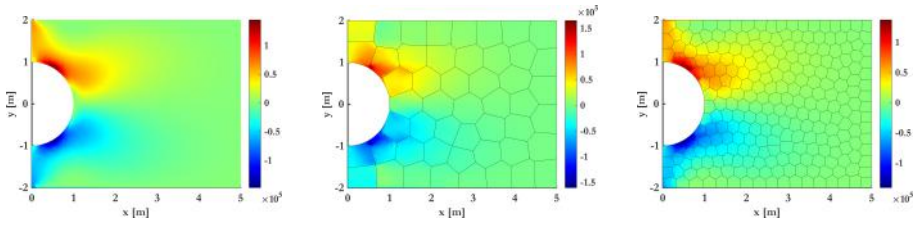

(a) Mesh 1 (b) Mesh 2 (c) Mesh 3

Figure 16: σ_{xy}: Stresses of solid skeleton at $t_i = 6.83$ hours, $i = 42$

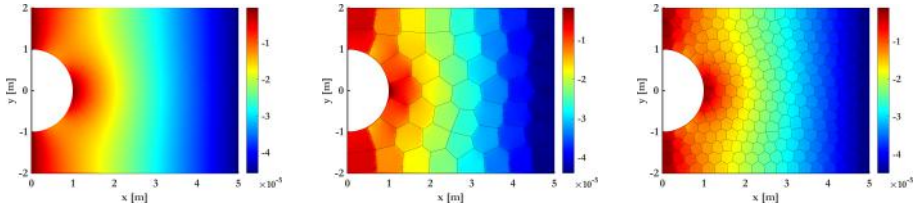

(a) Mesh 1 (b) Mesh 2 (c) Mesh 3

Figure 17: v_x: Darcy velocity of pore fluid at $t_i = 6.83$ hours, $i = 42$

The stresses σ_{xx}, σ_{yy}, σ_{xy} and the Darcy velocities v_x, v_y computed over Mesh 2 show significant deviations from the reference solution i.e., Mesh 1. Conversely, Mesh 3 offers practically equivalent results. Hence, Mesh 2 is insufficient in capturing local variations in secondary or derived fields. A finer coarse discretization, i.e., Mesh 3 is required in such cases. Despite proving more expensive than Mesh 2, it still offers significant reduction in computational effort compared to Mesh 1. This trade-off between accuracy and computational effort is studied more rigorously in Section 4.1.2 and 4.1.3, respectively.

4.1.2. Convergence behaviour

To investigate the convergence behaviour of the proposed CMsVEM, six different discretization schemes are considered at the coarse scale, i.e., with 25, 50, 100, 250, 500 and 1000 polygonal elements. For each case, the five different micro-structure discretizations shown in Fig. 19 are employed and the relative

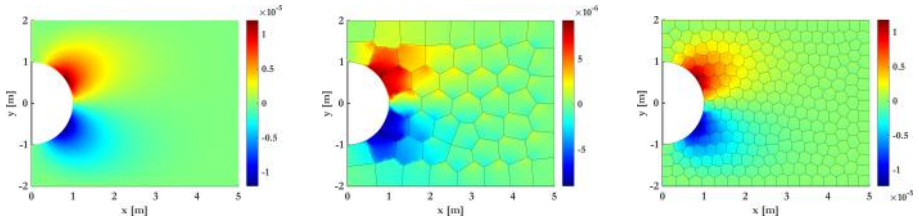

(a) Mesh 1 (b) Mesh 2 (c) Mesh 3

Figure 18: v_y: Darcy velocity of pore fluid at $t_i = 6.83$ hours, $i = 42$

$\mathcal{L}_2$ and $\mathcal{H}_1$ error norms are evaluated. A standard VEM solution with 5000 CVT elements is used as the reference solution.

Figs. 20a and 20b summarize the convergence analysis results for the solid skeleton displacements and stresses, respectively. The error in the solid skeleton quantities reduces for finer coarse and micro-element discretizations. The case of 250 coarse elements and 25 micro-elements per coarse element is an upper bound below which all solutions seems to provide identical and well-behaved results. This is not the case for the fluid phase, where the error is primarily controlled by the coarse element size rather than the micro-structure resolution as shown in Figs. 20c and 20d for the pressures and fluxes, respectively. Although this observation hints at the idea of resolving the two governing equations at different meshes hence further reducing computational costs, it is important to mention that this example involves a homogeneous domain where such a convergence response is to be expected.

The error convergence rates for both phases are summarized in Table 5. These are found to nearly coincide with the theoretical convergence rates of 2 in the $\mathcal{L}_2$ and 1 in the $\mathcal{H}_1$ relative error norms, respectively. The theoretical convergence rates are provided in [83] for elasto-static problems. Hence, all microstructural configurations result in near optimal error convergence rates. This establishes the CMsVEM as an alternative to the CMsFEM when flexible mesh generation is required.

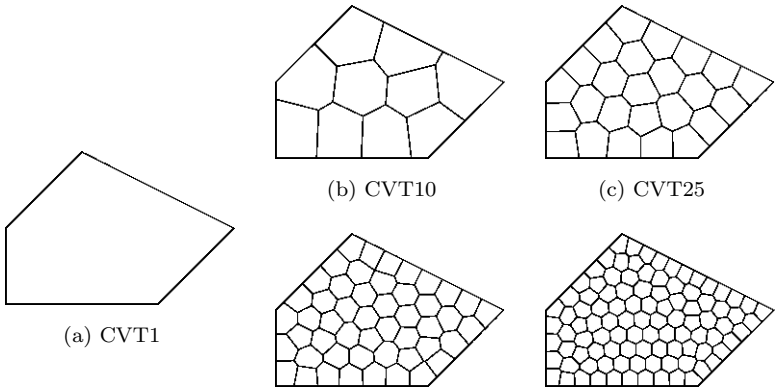

(a) CVT1 (b) CVT10 (c) CVT25 (d) CVT50 (e) CVT100

Figure 19: 5 microstructures illustrated for an arbitrarily chosen polygonal coarse element

	$\|\|\mathbf{u}_h - \mathbf{u}_{ex}\|\|_{\mathcal{L}_2}$	$\|\|\mathbf{p}_h - \mathbf{p}_{ex}\|\|_{\mathcal{L}_2}$	$\|\|\mathbf{u}_h - \mathbf{u}_{ex}\|\|_{\mathcal{H}_1}$	$\|\|\mathbf{p}_h - \mathbf{p}_{ex}\|\|_{\mathcal{H}_1}$
CVT1	1.6901	1.8265	0.8993	1.0316
CVT10	2.0504	2.0008	0.9279	1.0121
CVT25	1.8949	2.0470	0.9265	1.0141
CVT50	1.7623	1.6956	0.8926	1.0049
CVT100	2.0117	1.7914	1.1331	0.9780

Table 5: Rates of error convergence

4.1.3. Discussion on computational effort

To examine the computational toll of the CMsVEM, the time required for pre-processing, analysis, and downscaling is recorded. These times are averaged over five runs and are illustrated as a function of the coarse and fine discretizations used in 4.1.2.

The time required to create the coarse elements is displayed in Fig. 21a. This includes the evaluation of the multiscale basis functions and the upscaling procedure used to create coarse element state matrices. A linear front is observed, indicating that the number of operations required depends on both, the number of coarse and fine elements. This is expected as in this case the RVEs

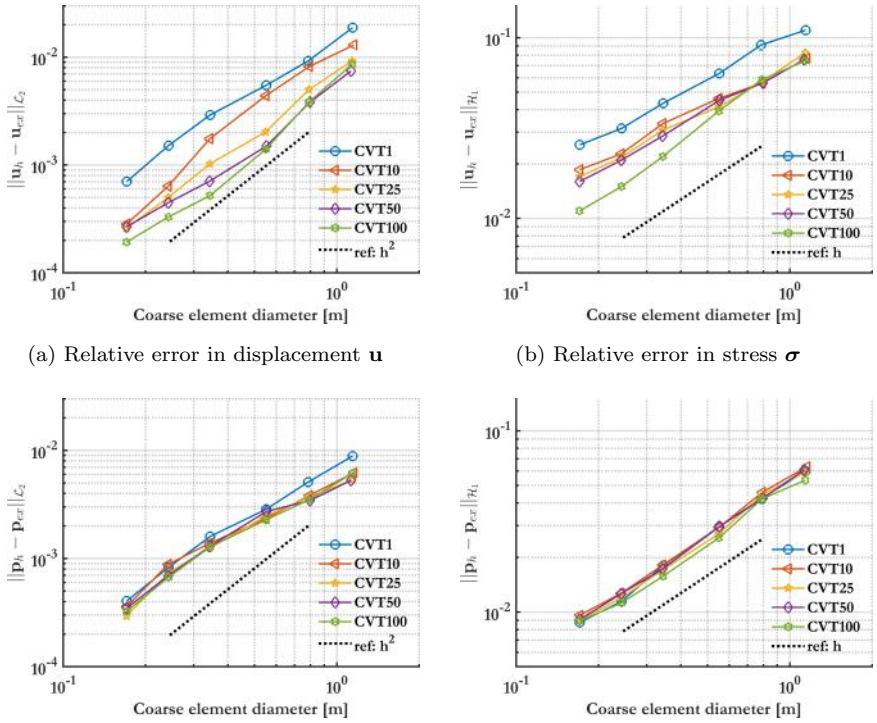

(a) Relative error in displacement $\mathbf{u}$

(b) Relative error in stress $\boldsymbol{\sigma}$

(c) Relative error in pressure $\mathbf{p}$

(d) Relative error in flux $\mathbf{q}$

Figure 20: Convergence results for 5 microstructure configurations at $t_i = 6.83$ hours, $i = 42$

are non-periodic and the basis-functions are evaluated for each coarse element individually. In the case of periodically repeated RVEs, basis functions would be evaluated once for each periodic group and the computational time would be independent of the number of coarse elements involved.

The time required for the assembly of the global coarse state matrices $\mathbf{K}_M$, $\mathbf{Q}_M$, $\mathbf{H}_M$, $\mathbf{S}_M$, and the solution of global system of linear equations at the coarse scale through finite-differences are shown in Figs. 21b and 21c, respectively. It is evident that these times depend exclusively on the number of coarse elements. The assembly procedure is of the order of magnitude $1E-02$ seconds and can be considered negligible in comparison to the solve times. This can be accounted for by the fact that the global state matrices are assembled only once.

The time required for downscaling is provided in Fig. 21d. This includes the

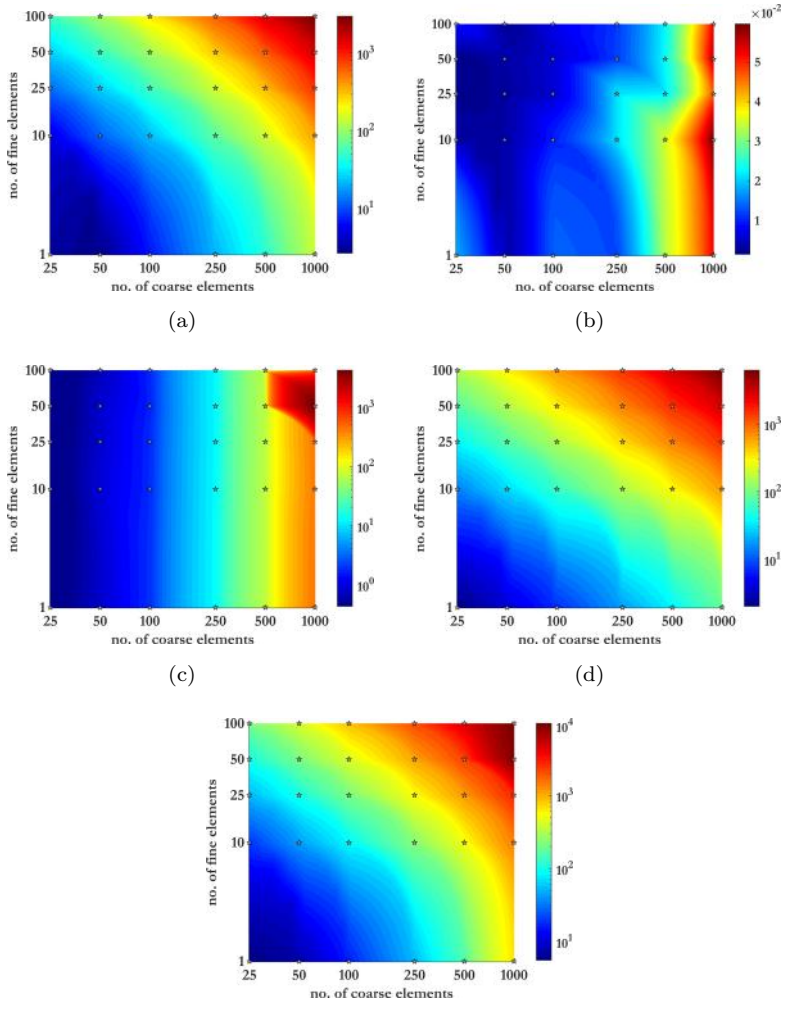

Figure 21: Computational time (in seconds) for (a) Coarse elements creation (b) Global coarse element state matrices assembly (c) Solution at the coarse scale (d) Down-scaling (e) Total time

procedure described in Section 3.6. The computational effort here is a function of the coarse and fine scale discretizations. Finally, to account for possible overheads in the computation, the total time taken for the entire CMsVEM is provided in Fig. 21e.

4.2. Heterogeneous Soil Domain

A fully saturated soil domain of 40 m $\times$25 m shown in Fig. 22 is considered. Two discretizations are examined, which are summarized in Table 6. In the first (see also, Fig. 22a) a coarse structured grid containing 40 (8×5) quadrilateral elements is considered. Each coarse element comprises a micro-mesh of 5×5 quadrilateral micro-elements. The total number of micro-elements is 1000. The second discretization, shown in Fig. 22b involves an unstructured coarse mesh containing 40 uniform CVT elements. In this case, each coarse element clusters 25 CVT fine elements and the total number of micro-elements is again 1000. A reference discretization of 40×25 quadrilateral elements is considered to facilitate comparisons. The domain is subjected to a compressive load at the top boundary with the loading history shown in Fig. 23. The domain is fully supported at its bottom edge. Sliding conditions are considered in the left and right-most edges.

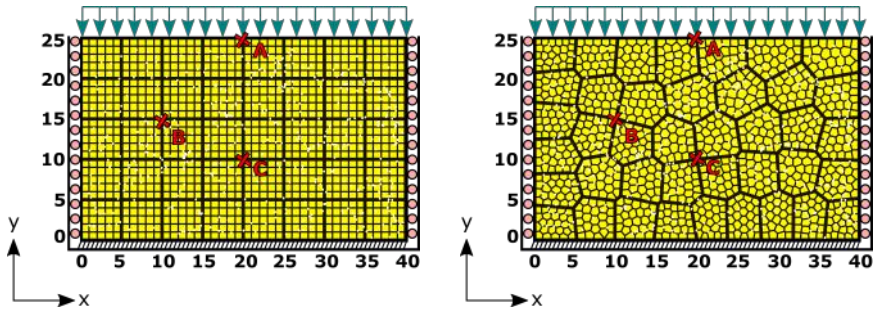

Figure 22: Saturated 40 m $\times$ 25 m soil domain with (a) 8×5 coarse structured quadrilateral mesh and 40×25 fine structured quadrilateral mesh, (b) coarse unstructured CVT polygonal mesh with 40 elements and fine unstructured CVT polygonal mesh with 1000 elements

Label	Full Mesh	Multiscale Mesh	
	[-]	Macro	Micro
QUAD	40 x 25	8 x 5	5 x 5
CVT	1000	40	25

Table 6: Discretization schemes

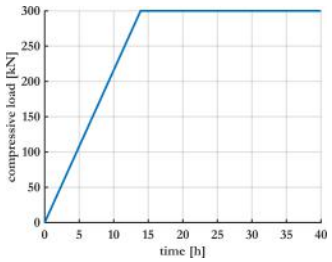

Figure 23: Loading history.

To investigate the fidelity of the phase-decoupling hypothesis used in deriving the multiscale basis functions in Section 3.3, two heterogeneous descriptions of the domain are examined. To investigate the influence of the assumed boundary conditions at the coarse element boundary for the evaluation of the micro-basis functions two cases are run for each heterogeneous description, i.e, the case of linear and oscillatory boundary conditions. The methods used are summarized in Table 8.

4.2.1. Case 1 - Heterogeneous permeability $\mathbf{k}$

In this case, isotropic heterogeneous random permeability fields are considered, sampled from a lognormal distribution of mean $\mu(\log(\mathbf{k})) = -12$ and

Parameter	ν	γ_f	K_s	K_f	$\mathbf{g}$	ρ_s	ρ_f	n
		$[Pa \cdot s]$	[Pa]	[Pa]	$[m \cdot s^{-2}]$	$[kg \cdot m^{-3}]$	$[kg \cdot m^{-3}]$	
Value	0.2	10^{-3}	10^{12}	2×10^9	0	2.8×10^3	10^3	0.2

Table 7: Homogeneous material parameters of the soil domain

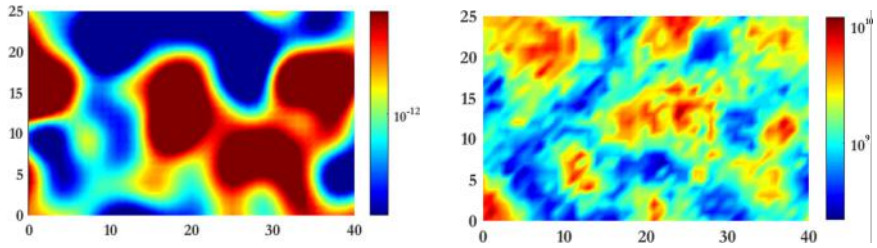

(a) (b)

Figure 24: (a) Randomly sampled heterogeneous isotropic permeability field, (b) Randomly sampled heterogeneous Young's modulus

Abbreviation	Method	Mesh-Type	Boundary Conditions
VEM	Virtual Element Method	Quadrilateral	-
MS-QUAD LIN	Multiscale Virtual Element Method	Quadrilateral	Linear
MS-CVT LIN	Multiscale Virtual Element Method	Polygonal	Linear
MS-QUAD OSC	Multiscale Virtual Element Method	Quadrilateral	Oscillatory
MS-CVT OSC	Multiscale Virtual Element Method	Polygonal	Oscillatory

Table 8: Methods investigated

standard deviation $\sigma(\log(\mathbf{k})) = 1.0$. The field has a maximum and minimum value of $\mathbf{k} = 5 \times 10^{-9}\,\mathrm{m}^2$ and $\mathbf{k} = 7 \times 10^{-16}\,\mathrm{m}^2$, respectively. A snapshot is provided in Fig. 24a. For the solid phase, a homogeneous modulus $\mathrm{E} = 5 \times 10^9\,\mathrm{Pa}$ is employed. The remaining material parameters are uniformly distributed over the entire domain and are summarized in Table 7. Due to the random distribution of the permeability, multiscale basis functions are evaluated all coarse elements individually.

Three points of interest, i.e., points A(20, 25), B(10,15), and C(20,10) are considered as shown in Fig. 22. The time evolution of the expectation values of displacements u_x, u_y, and pressures p obtained over $n_s = 5000$ samples at these points are illustrated in Fig. 25.

Due to symmetry the horizontal displacement component u_x at Points A and C is practically zero as illustrated in Figs. 25a and 25c, respectively. Minor

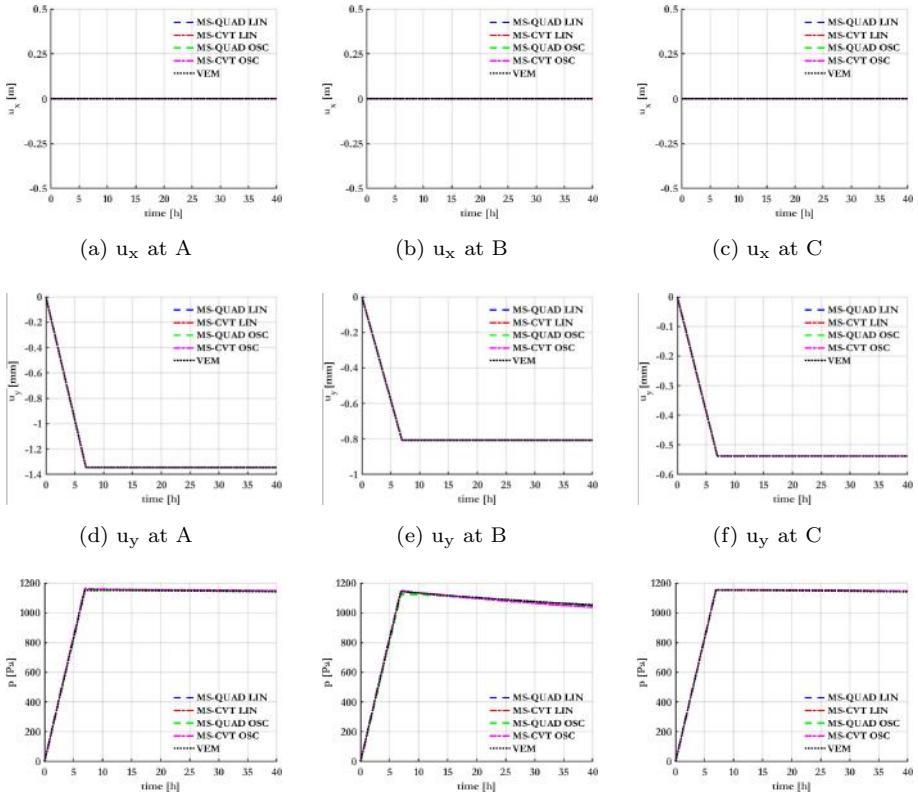

(a) u_x at A (b) u_x at B (c) u_x at C

(d) u_y at A (e) u_y at B (f) u_y at C

(g) p at A (h) p at B (i) p at C

Figure 25: Time evolution t = 40h of expectation values of horizontal displacement $E[u_x]$, vertical displacement $E[u_y]$, and pore-fluid pressure E[p] at points A, B, and C, obtained for $n_s = 5000$ samples

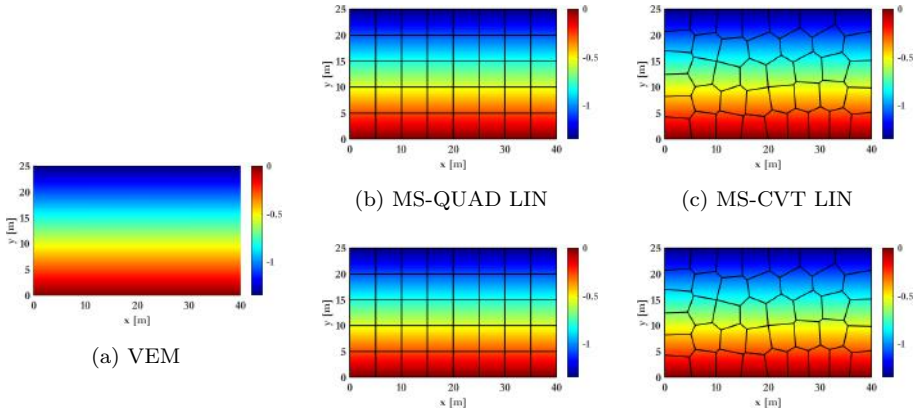

(a) VEM (b) MS-QUAD LIN (c) MS-CVT LIN

(d) MS-QUAD OSC (e) MS-CVT OSC

Figure 26: E[u_y] displacement contours (in [mm]) at t = 40h obtained for $n_s = 5000$ samples.

deviations from zero are attributed to asymmetric permeability fields sampled from the lognormal distribution. As shown in Figs. 25 regardless of the boundary conditions employed, all CMsVEM runs match perfectly the standard VEM solutions.

Snapshots of the expectation values of the results obtained at $t = 40$ hours are shown in Figs. 26 and 27 for the vertical displacement component and the pressures, respectively.

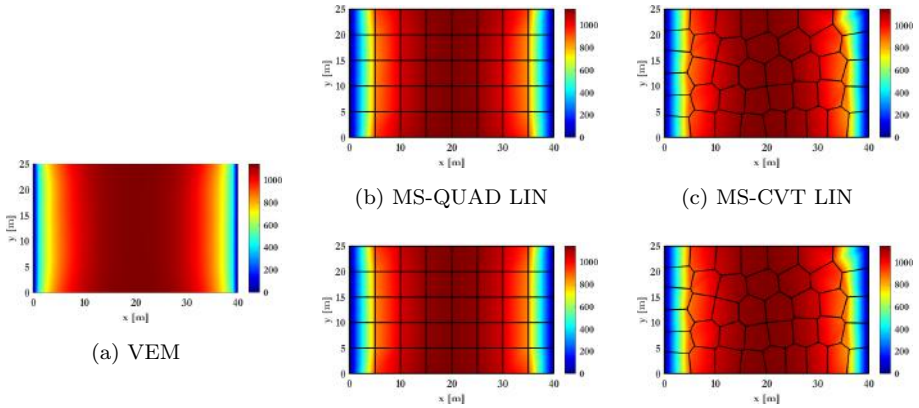

(a) VEM (b) MS-QUAD LIN (c) MS-CVT LIN (d) MS-QUAD OSC (e) MS-CVT OSC

Figure 27: E[p] pressure contours (in [Pa]) at t = 40h obtained for $n_s = 5000$ samples.

4.2.2. Case 2 - Heterogeneous permeability **k** *and heterogeneous Young's modulus E*

Here, the heterogeneous permeability **k** field employed in the previous case is considered together with a heterogeneous Young's Modulus E distribution. The heterogeneous random Young's modulus fields are defined with maximum and minimum values of $E = 1 \times 10^{10}$ Pa and $E = 7 \times 10^{8}$ Pa, respectively. A snapshot is provided in Fig. 24b. The remaining material parameters are uniformly distributed over the entire domain and are summarized in Table 7. As in the previous case, the multiscale basis functions are evaluated for all coarse elements individually.

The resulting time evolution of the expectation values of u_x, u_y, and p at points A, B and C as obtained over $n_s = 5000$ samples are shown in Fig. 28. Contrary to Case 1, the heterogeneities in the solid domain increase the granularity between the different methods considered. Although the accuracy of the predicted displacements is acceptable, the methods using oscillatory boundary conditions, i.e., MS-QUAD OSC and MS-CVT OSC provide the best match to the standard VEM solution. The differences are more pronounced in the predicted pressure fields Figs. 28, where MS-QUAD LIN and MS-CVT LIN

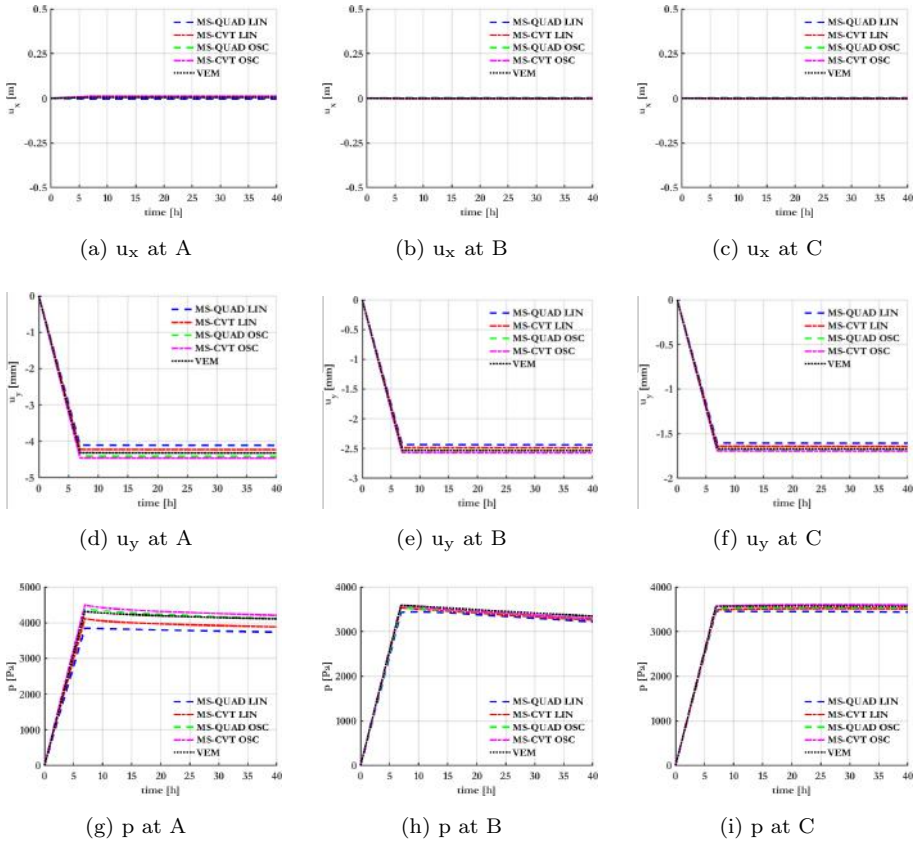

(a) u_x at A (b) u_x at B (c) u_x at C

(d) u_y at A (e) u_y at B (f) u_y at C

(g) p at A (h) p at B (i) p at C

Figure 28: Time evolution t = 40h of expectation values of horizontal displacement $E[u_x]$, vertical displacement $E[u_y]$, and pore-fluid pressure E[p] at points A, B, and C, obtained for $n_s = 5000$ samples

consistently under-predict pressures at the three points.

The contours of expectation values for the horizontal and the vertical component of the displacement fields at $t = 40$ hours are shown in Figs. 29 and 30, respectively. The corresponding pressure field is shown in Fig. 31.

The linear boundary conditions impose a strict constraint on the deformability of the heterogeneous micro-structure. This is consistent with the physics of the problem where a nonlinear displacement profile is to be expected due to the joined permeability and Young's modulus heterogeneity. The choice on the

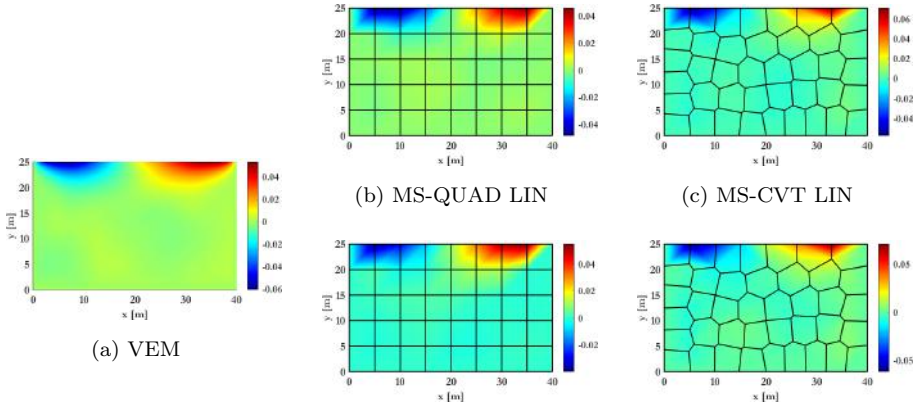

(a) VEM (b) MS-QUAD LIN (c) MS-CVT LIN

(d) MS-QUAD OSC (e) MS-CVT OSC

Figure 29: E[u_x] displacement contours (in [m]) at t = 40h obtained for $n_s = 5000$ samples.

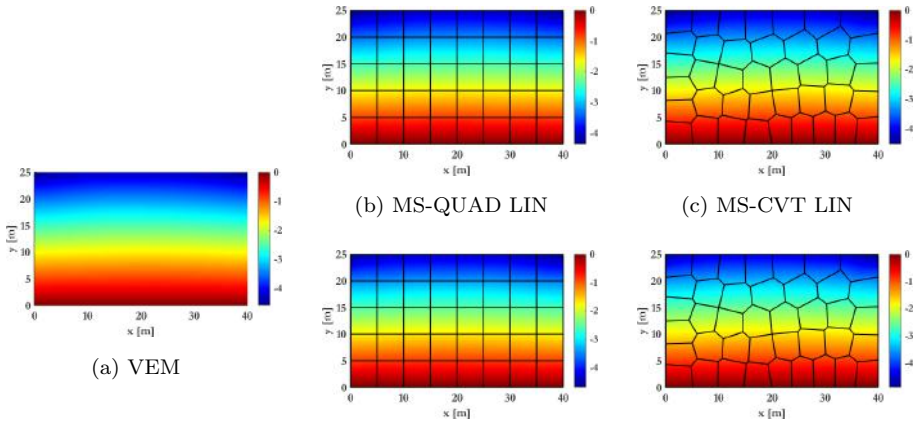

(a) VEM (b) MS-QUAD LIN (c) MS-CVT LIN

(d) MS-QUAD OSC (e) MS-CVT OSC

Figure 30: E[u_y] displacement contours (in [mm]) at t = 40h obtained for $n_s = 5000$ samples.

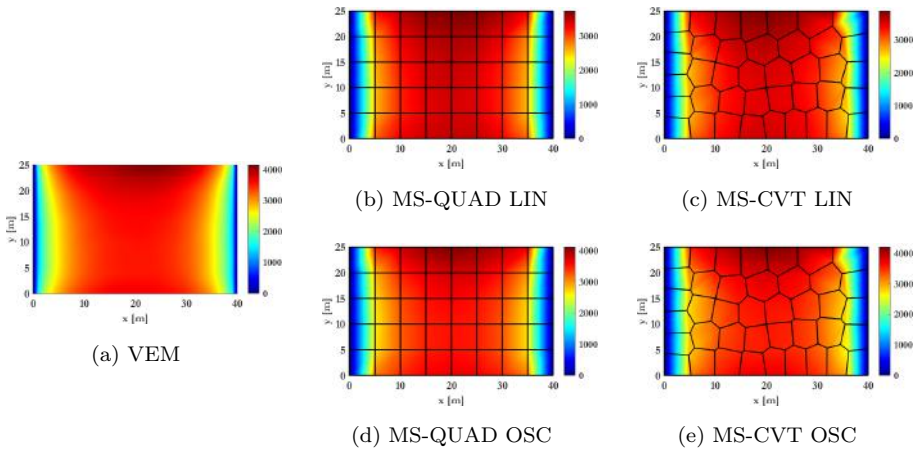

(a) VEM (b) MS-QUAD LIN (c) MS-CVT LIN (d) MS-QUAD OSC (e) MS-CVT OSC

Figure 31: E[p] pressure contours (in [Pa]) at t = 40h obtained for $n_s = 5000$ samples.

boundary conditions to be employed for the evaluation of the basis-functions should be driven by the physics. Using a decoupled scheme for the evaluation of the basis-functions on the other hand does not significantly affect the accuracy of the CMsVEM while imposing minimum costs on the evaluation of the basis vector. This observation could prove particularly beneficial in the case of non-linear problems where a re-evaluation of the basis would be required. However such aspects are beyond the scope of this work.

To examine whether the oscillatory boundary conditions ensure compatibility of the fine scale solution across boundaries, contour plots of the total displacement, pressure, strain component ϵ_{yy}, and stress component σ_{yy} obtained at $t = 40$ hours for a single realization of the heterogeneous Young's modulus and permeability fields using oscillatory boundary conditions are shown in Figs. 32. In all cases, the downscaled quantities vary smoothly across the coarse element boundaries, despite the prevalence of significant heterogeneities.

Consistency and continuity properties are investigated in more detail by considering two neighbouring coarse elements, i.e. 16 and 31, as shown in Fig. 33. The interface encountered is non-conforming in nature. These elements are chosen as the underlying material description here is highly heterogeneous. Conse-

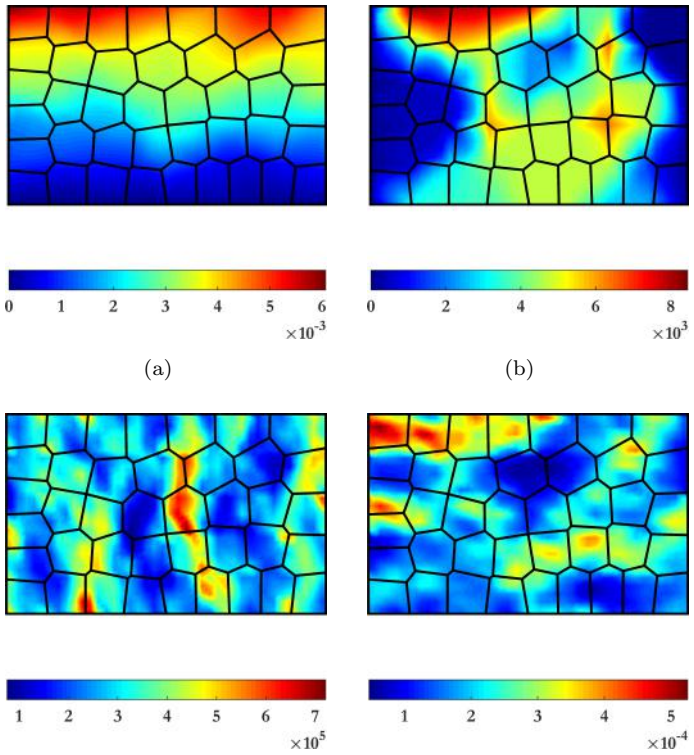

Figure 32: (a) $||\mathbf{u}||$ (in [m]), (b) p (in [Pa]), (c) $-\boldsymbol{\sigma}_{yy}$ (in [Pa]) and (d) $-\boldsymbol{\varepsilon}_{yy}$ contours at $t = 40$ hours for a single realization of the heterogeneous E and $\mathbf{k}$ field.

quently, continuity of field variables at this interface should provide satisfactory guarantees for similar continuous behaviour across other coarse element interfaces as well. The total displacements $||\mathbf{u}||$ and strain $\boldsymbol{\varepsilon}_{yy}$ evaluated at the fine-scale interface nodes belonging to each coarse element are provided in Tables 9 and 10.

It can be seen from Tables 9 and 10 that $||\mathbf{u}||$ and $\boldsymbol{\varepsilon}_{yy}$ evaluated at the fine nodes corresponding to coarse node M_{47}, i.e., 1 and 29, and M_{50}, i.e., 15 and 5 are practically identical. Despite non-conformity of intermediate edge interface nodes, the quantities appear continuous here as well.

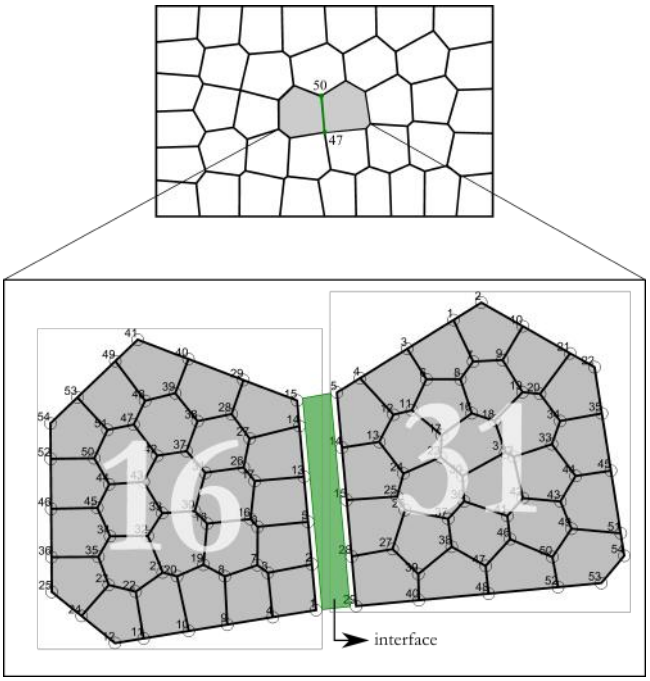

Figure 33: Microstructures of adjacent coarse elements 16 and 31. The interface joins coarse nodes M_{47} and M_{50}.

4.2.3. Discussion on computational gains

The computational efficiency of the CMsVEM is assessed by recording times for critical procedures for all methods. All times displayed are averaged over five runs.

The time taken for assembling global coarse scale state matrices $\mathbf{K}_M$, $\mathbf{Q}_M$, $\mathbf{H}_M$ and $\mathbf{S}_M$ is shown in Fig. 34a. This includes the computation of multiscale basis functions and upscaling procedures used to create coarse element state matrices. All multiscale methods practically perform equally in this regard and offer a speedup of approximately a factor eight ($\approx 8\times$) when compared to the VEM. As using oscillatory boundary conditions when computing multiscale basis functions does not require more computational effort than the simpler case of linear boundaries, one should always prefer MS-QUAD OSC and MS-CVT OSC over MS-QUAD LIN and MS-CVT LIN in the event of highly heteroge-

Fine Node	**15**	**14**	**13**	**5**	**2**	**1**
$\|\|\mathbf{u}\|\|$	3.19442	3.05568	2.98009	2.83392	2.70283	2.65383
ε_{yy}	-0.1645	-0.1645	-0.1646	-0.1647	-0.1647	-0.1648

Table 9: Fine-scale $||\mathbf{u}||$ (in [mm]) and $\varepsilon_{yy}(\times 10^{-3})$ along interface for coarse element 16

Fine Node	**5**	**14**	**15**	**28**	**29**
$\|\|\mathbf{u}\|\|$	3.19442	2.90025	2.82015	2.71886	2.65383
ε_{yy}	-0.165	-0.1649	-0.1648	-0.1649	-0.1649

Table 10: Fine-scale $||\mathbf{u}||$ (in [mm]) and $\varepsilon_{yy}(\times 10^{-3})$ along interface for coarse element 31

neous material definitions.

The time taken for the solution procedure is illustrated in Fig. 34b. All multiscale methods again perform equally efficiently and offer a speedup of $\approx 200\times$ when compared to the VEM. This enormous reduction in computational effort is to be expected as the number of nodes in the multiscale procedures is significantly reduced in comparison to it's VEM counterparts. Repeated matrix inversions in the case of finite-difference time domain solutions further establish the effectiveness of the CMsVEM.

The postprocessing times are displayed in Fig. 35a. This involves the downscaling procedure used to recover fine scale information and evaluating derivative quantities like stresses, strains and fluxes over fine element domains. Once again, all multiscale methods perform equivalently and offer a speedup of $\approx 2\times$ in comparison to the VEM. This is attributed to the fact that in the multiscale methods, the downscaling procedure is performed for each coarse element. This implicitly vectorizes the associated stress and flux computation loops. It is of interest to note that since the consolidation problem examined is linear, the multiscale basis functions are computed offline. As a result, no significant

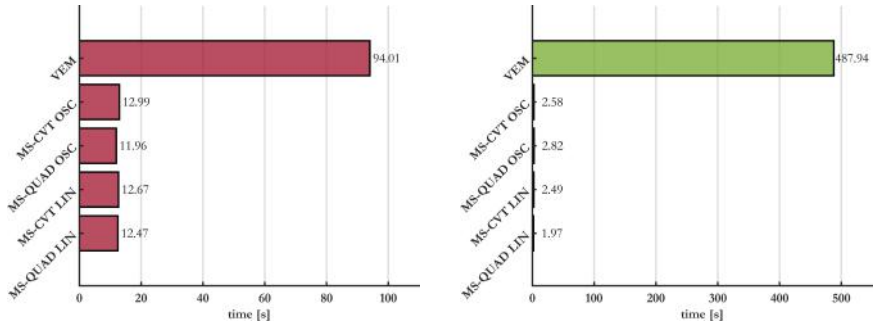

(a) (b)

Figure 34: (a) Time taken to assemble global coarse element state matrices, (b) Time taken to solve system of linear equations at coarse scale

overheads are incurred to the overall solution procedure.

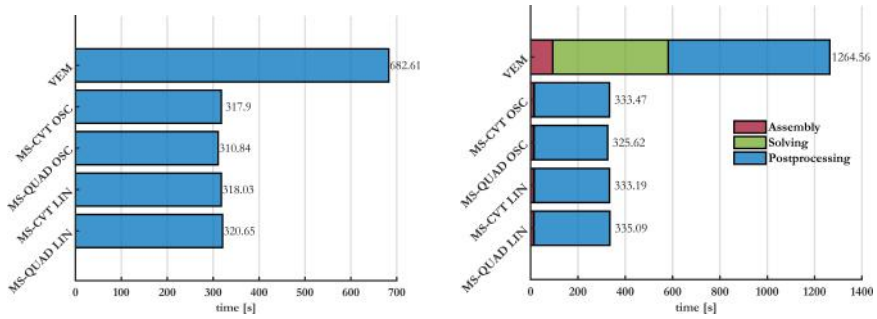

(a) (b)

Figure 35: (a) Time taken to postprocess the solution , (b) Total time taken

It can be seen from Fig. 35b that all multiscale methods offer an appreciable total speedup of $\approx 4\times$ when compared with the VEM. Such speedups prove extremely valuable when obtaining statistical moments for random field simulations using for e.g. classical Monte-Carlo approaches. In this example, expectation values for 5000 samples were computed, thus generating an overall speed up of $\approx 20000\times$ when compared to the VEM. A similar comparison between FEM, VEM, MsFEM and MsVEM is provided in Figs. 36 and 37. The VEM and MsVEM are found to offer quicker assembly and postprocessing

computational times than their FEM and MsFEM counterparts.

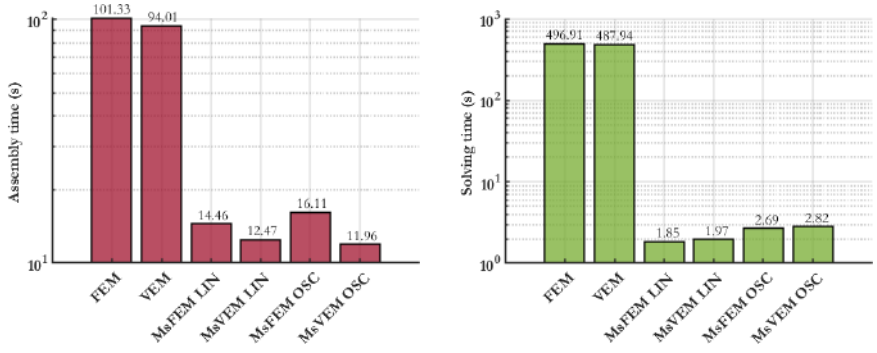

(a) (b)

Figure 36: (a) Time taken to assemble global coarse element state matrices, (b) Time taken to solve system of linear equations at coarse scale

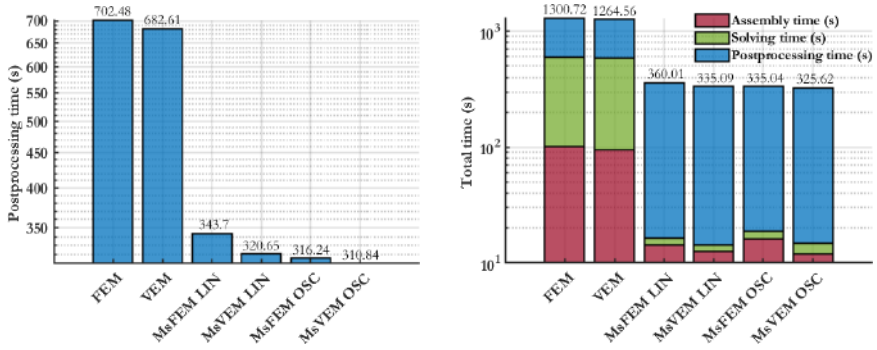

(a) (b)

Figure 37: (a) Time taken to postprocess the solution , (b) Total time taken

4.3. Honeycomb structure

The honeycomb structure shown in Fig. 38 is considered herein. The overall dimensions of the domain are $5m \times 5m$. This domain consists of 25 periodically repeated heterogeneous unit cells. Each unit cell comprises a matrix with a Young's modulus $E = 5$ MPa and a stiffer inclusion with $E = 500$ MPa. The structure is clamped at its bottom. The deflections along the horizontal are

	E [MPa]	ν [/]	γ_f [Pa · s]	K_s [Pa]	K_f [Pa]	ρ_s [kg · m^{-3}]	ρ_f [kg · m^{-3}]	n [/]	α_B [/]
Matrix	5	0.2	10^{-3}	3×10^4	10^4	10^3	10^3	0.2	1
Inclusion	500								

Table 11: Material parameters used

restricted on the left and right edges. No-flow conditions are imposed across all boundaries. The top maintains a pressure $p = 0$ and is subject to a progressively applied compressive load $\mathbf{t} = \begin{bmatrix} 0, & t_y \end{bmatrix}$. The loading history is shown in Fig. 9. The material parameters used are provided in Table 11.

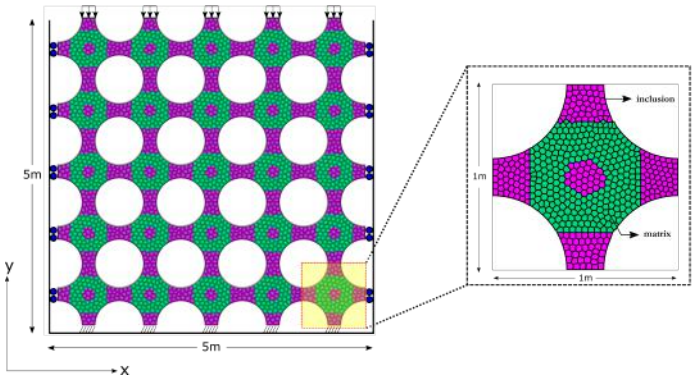

Figure 38: Schematic of a honeycomb structure

A multiscale discretization is considered wherein each of the 25 periodically repeating unit cells comprises 500 CVT elements. This is compared against a reference VEM solution evaluated over 12,500 CVT elements. All multiscale solutions are evaluated using oscillatory boundary conditions. Four multi-node coarse-element configurations, MS_1 to MS_4, are designed to examine the trade-off between accuracy and speedup. These are illustrated in Fig. 39.

All CMsVEM models involve the solution of a significantly reduced system of governing equations when compared to the reference VEM solution. In Fig. 40, the order reduction achieved per coarse element is provided as the ratio of the

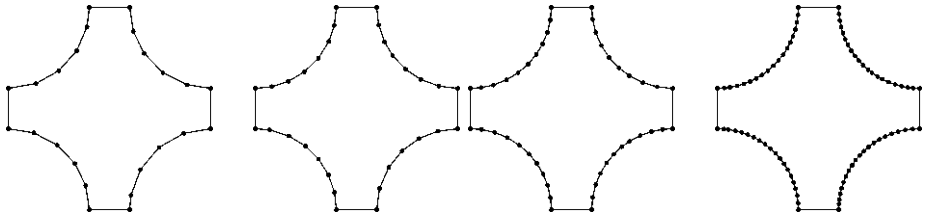

(a) MS_1: 24 coarse nodes (b) MS_2: 31 coarse nodes (c) MS_3: 44 coarse nodes (d) MS_4: 81 coarse nodes

Figure 39: The multi-node coarse element configurations

total number of degrees of freedom of the multiscale formulation to the degrees of freedom of the standard VEM implementation. Even in the case of the high-fidelity MS_4 coarse element, the order of the problem is practically halved.

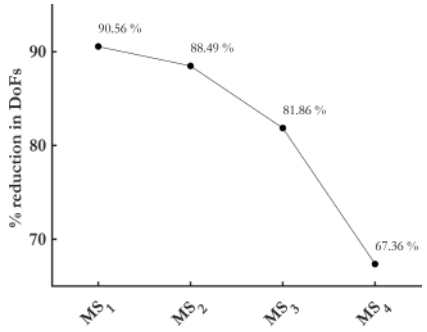

Figure 40: Percentage reduction in DoFs offered by each coarse element configuration, in relation to the complete VEM discretization.

The maximum pore-fluid pressures are found to occur at $t_i = 6.83$ hours, $i = 42$. Displacement, pressure, stress and flux contours are provided at this instant for the VEM and multiscale solutions. The total displacement contours $||\mathbf{u}||$ are shown in Fig. 41. Pressure contours p are provided in Fig. 42.

It can be seen from the Figs. 41 and 42 that the total displacement $||\mathbf{u}||$ and pressure p contours are practically the same for all cases. Von-Mises stress contours $\boldsymbol{\sigma}_{VM}$ are illustrated in Fig. 43. Total Darcy flux contours $||\mathbf{q}||$ are displayed in Fig. 44.

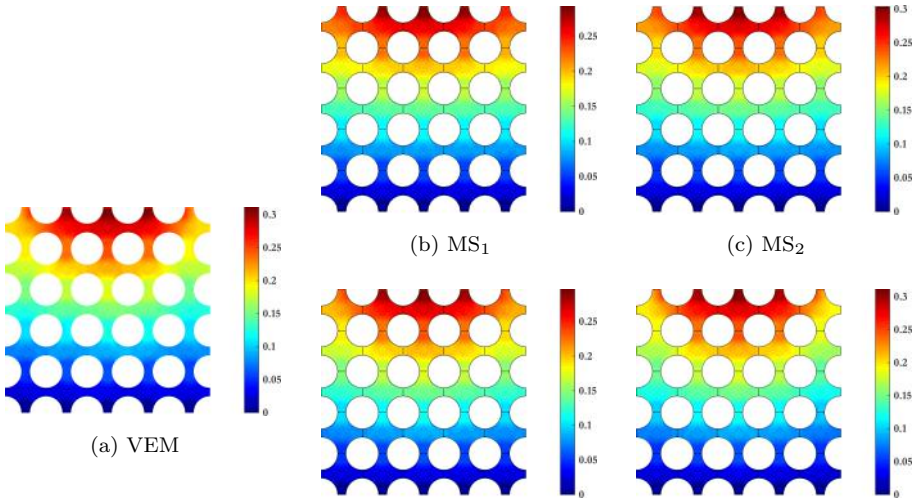

(a) VEM (b) MS_1 (c) MS_2 (d) MS_3 (e) MS_4

Figure 41: $||\mathbf{u}||$ total displacement contours at $t_i = 6.83$h, $i = 42$.

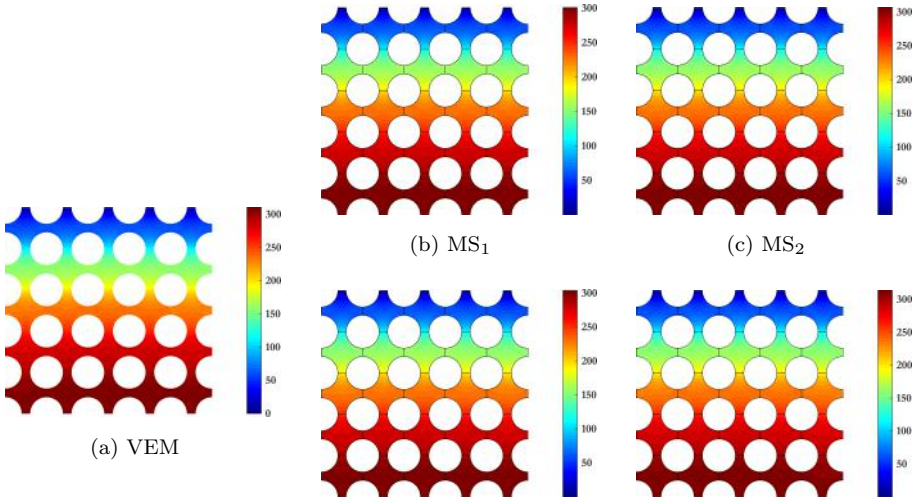

(a) VEM (b) MS_1 (c) MS_2 (d) MS_3 (e) MS_4

Figure 42: p pressure contours at $t_i = 6.83$h, $i = 42$.

Fig. 44 reveals that the total flux $||\mathbf{q}||$ contours is also practically equivalent for all cases. However, significant variations can be observed in the case of the

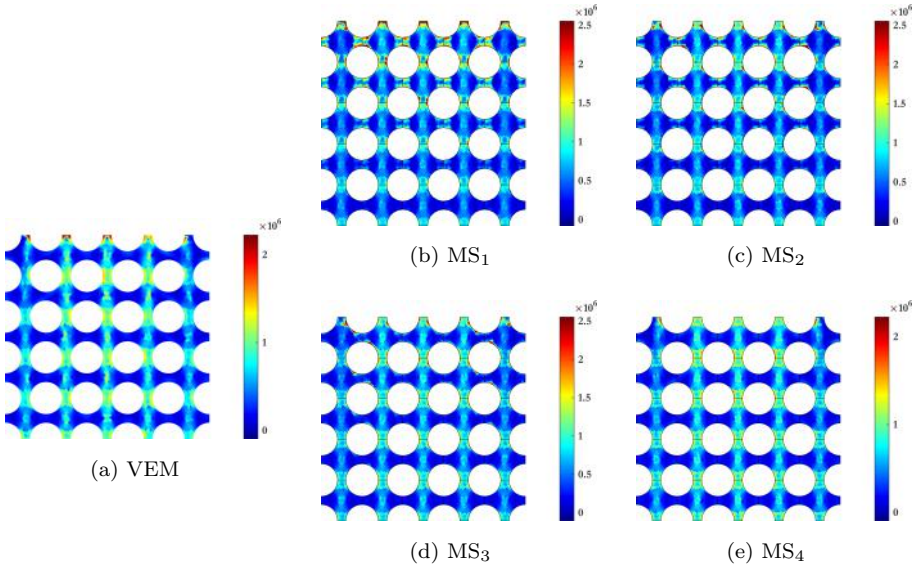

(a) VEM (b) MS_1 (c) MS_2 (d) MS_3 (e) MS_4

Figure 43: $\boldsymbol{\sigma}_{VM}$ Von-Mises stress contours at $t_i = 6.83$h, $i = 42$.

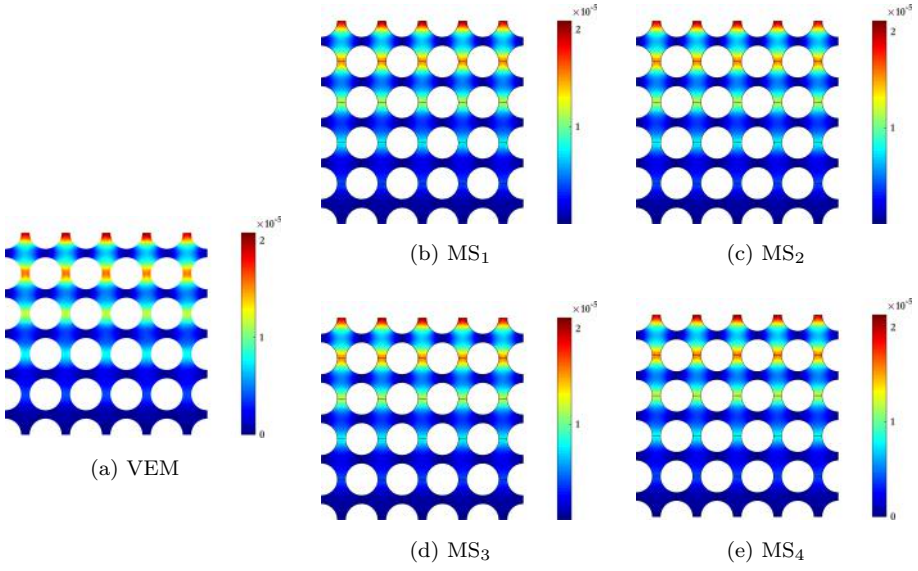

(a) VEM (b) MS_1 (c) MS_2 (d) MS_3 (e) MS_4

Figure 44: $||\mathbf{q}||$ total flux contours at $t_i = 6.83$h, $i = 42$.

Von-Mises stresses as shown in Fig. 43. The contours obtained are increasingly accurate moving from MS_1 to MS_4 when compared against the reference VEM solution. This is to be expected as the coarse element described by MS_4 provides a high-fidelity representation of the original curved boundary. This in turn ensures more accurate upscale and downscale mappings performed by the multiscale basis functions.

The time evolution of the relative $\mathcal{L}_2$ and $\mathcal{H}_1$ error norms in $\mathbf{u}$ and p are provided in Fig. 45. An appreciable reduction in errors is observed in Figs. 45a, 45b, 45c and 45d as the number of coarse nodes is increasing. This is to be expected as a more detailed account of the RVE geometry and underlying heterogeneities can prove critical to the fidelity of the upscaling and downscaling procedures.

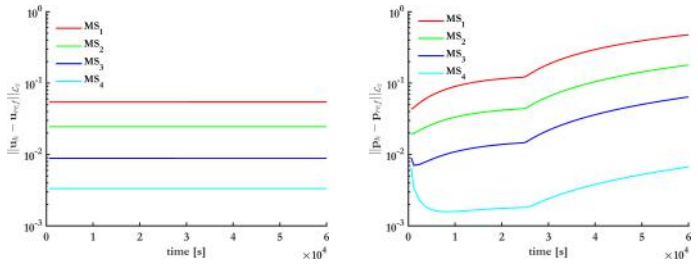

(a) Relative errors in displacements $\mathbf{u}$

(b) Relative errors in pressures p

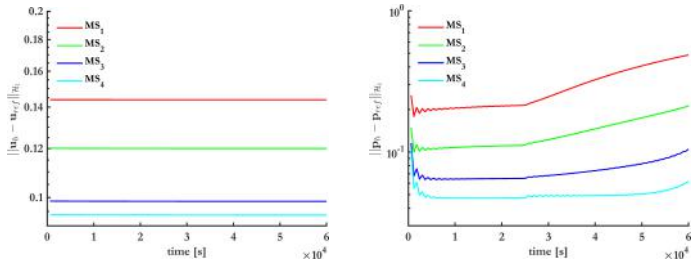

(c) Relative errors in stresses $\boldsymbol{\sigma}$

(d) Relative errors in flux $\mathbf{q}$

Figure 45: Evolution of errors in displacements and pressures for the four coarse-element configurations MS_1, MS_2, MS_3 and MS_4.

4.3.1. Discussion on computational gains

The computational cost associated with the MS_1, MS_2, MS_3 and MS_4 is studied here in terms of the speedup offered. The speedup metric is defined as follows

$$\text{speedup(operation)} = \frac{t_{\text{VEM}}(\text{operation})}{t_{\text{MS}_i}(\text{operation})},\ i = 1, \ldots 4, \tag{68}$$

where $t_{\text{VEM}}(\text{operation})$ and $t_{\text{MS}_i}(\text{operation})$ denote the times taken to complete a certain operation, using the VEM and CMsVEM discretizations, respectively.

The speedup offered by MS_1 through MS_4 for (a) assembly of global coarse element state matrices, (b) solving system of linear equations at the coarse scale, (c) post-processing the solution to obtain fine-scale information, and (d) the complete CMsVEM procedure, are shown in Figs. 46a, 46b, 46c and 46d, respectively. These operations are as defined in Section 4.2.

Near-linear trends in the speedup reduction is observed in Figs. 46a, 46c and 46d. A near-exponential decreasing trend is observed in the case of the solution procedure at the coarse-scale, as shown in Fig. 46b. The decreasing trends exhibited at all operations is further evidenced by the decrease in percentage reduction of coarse-scale DoFs, as shown in Fig. 40.

5. Conclusions

A novel CMsVEM has been developed for analysing consolidation phenomena in highly heterogeneous poroelastic media. The novelty of the method lies in using the VEM at the fine scale to enable flexible meshing capabilities to efficiently capture all types of heterogeneities. The solution procedure is performed at the coarse scale to reduce computational cost. Fine scale information is mapped onto the coarse scale through a set of numerically computed multi-scale basis functions. Subsequently, the solution is downscaled using the same basis functions to describe local fine scale variations. The ability of the method to handle flexible coarse element geometries enables more versatile meshing of non-standard domains.

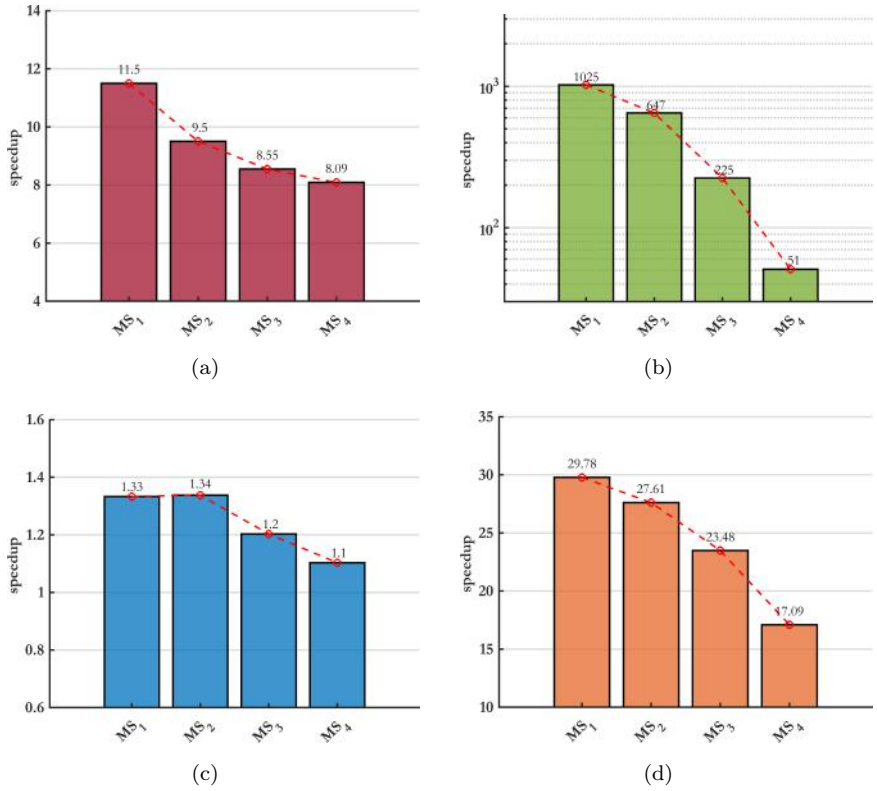

Figure 46: Speedup offered during (a) assembly of global coarse element state matrices, (b) solving system of linear equations at the coarse scale, (c) postprocessing the solution, (d) complete CMsVEM procedure

These extended meshing capabilities offered by the method allows for efficient modelling of complex geometries at the coarse and fine scale while retaining the accuracy of the standard FEM and its CMsFEM counterpart. The accuracy of the proposed method is validated against standard FEM and VEM solutions. Our convergence studies demonstrated that the CMsVEM is well behaved even in the case of highly oscillating heterogeneities at the fine scale.

The boundary conditions used in computing the multiscale basis functions are known to play a critical role in the accuracy of the method. Oscillating boundary conditions are shown to offer a better account of the behaviour of the system when significant heterogeneities are present.

The computational upscaling procedure performed offline, is shown to significantly drive down computational costs compared to the standard FEM or VEM, by reducing computational complexity. Consequently, overhead memory requirements are also appreciably lowered.

A limitation of the proposed method lies in it being confined to 2-D domains only. Extending the method to allow for more general 3-D polyhedral discretizations at both scales is currently under development.

Acknowledgements

This work has been carried out under the auspices of the grant: "European industrial doctorate for advanced, lightweight and silent, multifunctional composite structures — N2N". The N2N project is funded under the European Union's Horizon 2020 research and innovation programme under the Marie Sklodowska-Curie Actions Grant: 765472.

References

[1] F.-X. Bécot, L. Jaouen, An alternative biot's formulation for dissipative porous media with skeleton deformation, The Journal of the Acoustical Society of America 134 (6) (2013) 4801–4807.

[2] F. Chevillotte, L. Jaouen, F.-X. Bécot, On the modeling of visco-thermal dissipations in heterogeneous porous media, The Journal of the Acoustical Society of America 138 (6) (2015) 3922–3929.

[3] F. Chevillotte, C. Perrot, E. Guillon, A direct link between microstructure and acoustical macro-behavior of real double porosity foams, The Journal of the Acoustical Society of America 134 (6) (2013) 4681–4690.

[4] V.-H. Nguyen, E. Rohan, S. Naili, Multiscale simulation of acoustic waves in homogenized heterogeneous porous media with low and high permeability contrasts, International Journal of Engineering Science 101 (2016) 92–109.

[5] C. V. Singh, R. Talreja, A multiscale approach to modeling of composite damage, in: Modeling Damage, Fatigue and Failure of Composite Materials, Elsevier, 2016, pp. 329–345.

[6] M. A. Biot, General theory of three-dimensional consolidation, Journal of applied physics 12 (2) (1941) 155–164.

[7] N. Castelletto, H. Hajibeygi, H. A. Tchelepi, Multiscale finite-element method for linear elastic geomechanics, Journal of Computational Physics 331 (2017) 337–356.

[8] N. Guo, J. Zhao, Multiscale insights into classical geomechanics problems, International Journal for Numerical and Analytical Methods in Geomechanics 40 (3) (2016) 367–390.

[9] C. L. Cipolla, E. P. Lolon, J. C. Erdle, B. Rubin, et al., Reservoir modeling in shale-gas reservoirs, SPE reservoir evaluation & engineering 13 (04) (2010) 638–653.

[10] E. Perrin, B. Bou-Saïd, F. Massi, Numerical modeling of bone as a multiscale poroelastic material by the homogenization technique, Journal of the Mechanical Behavior of Biomedical Materials 91 (2019) 373–382.

[11] T. Kuroki, T. Ito, K. Onishi, Boundary element method in biot's linear consolidation, Applied Mathematical Modelling 6 (2) (1982) 105–110.

[12] Y. Chang, K. Mohanty, Scale-up of two-phase flow in heterogeneous porous media, Journal of Petroleum Science and Engineering 18 (1-2) (1997) 21–34.

[13] Y. Davit, M. Quintard, Technical notes on volume averaging in porous media i: how to choose a spatial averaging operator for periodic and quasiperiodic structures, Transport in Porous Media 119 (3) (2017) 555–584.

[14] W. Guannan, An efficient analytical homogenization technique for mechanical-hygrothermal responses of unidirectional composites with applications to optimization and multiscale analyses, Chinese Journal of Aeronautics 32 (2) (2019) 382–395.

[15] K. Markov, L. Preziosi, Heterogeneous media: micromechanics modeling methods and simulations, Springer Science & Business Media, 2012.

[16] M. Tootkaboni, L. Graham-Brady, A multi-scale spectral stochastic method for homogenization of multi-phase periodic composites with random material properties, International journal for numerical methods in engineering 83 (1) (2010) 59–90.

[17] J. Schröder, A numerical two-scale homogenization scheme: the fe 2-method, in: Plasticity and beyond, Springer, 2014, pp. 1–64.

[18] I. Sokolova, M. G. Bastisya, H. Hajibeygi, Multiscale finite volume method for finite-volume-based simulation of poroelasticity, Journal of Computational Physics 379 (2019) 309–324.

[19] T. Hou, Y. Efendiev, Multiscale Finite Element Methods, 2009.

[20] S. P. Triantafyllou, E. N. Chatzi, A hysteretic multiscale formulation for nonlinear dynamic analysis of composite materials, Computational Mechanics 54 (2014) 763–787.

[21] J. G. Berryman, Comparison of upscaling methods in poroelasticity and its generalizations, Journal of Engineering Mechanics 131 (9) (2005) 928–936.

[22] I. Babuška, J. E. Osborn, Generalized finite element methods: their performance and their relation to mixed methods, SIAM Journal on Numerical Analysis 20 (3) (1983) 510–536.

[23] T. Y. Hou, X.-H. Wu, A multiscale finite element method for elliptic problems in composite materials and porous media, Journal of computational physics 134 (1) (1997) 169–189.

[24] H. Zhang, Z. Fu, J. Wu, Coupling multiscale finite element method for consolidation analysis of heterogeneous saturated porous media, Advances in water resources 32 (2) (2009) 268–279.

[25] H.-W. Zhang, J.-K. Wu, J. Lü, Z.-D. Fu, Extended multiscale finite element method for mechanical analysis of heterogeneous materials, Acta mechanica sinica 26 (6) (2010) 899–920.

[26] V. Kippe, J. E. Aarnes, K.-A. Lie, A comparison of multiscale methods for elliptic problems in porous media flow, Computational Geosciences 12 (3) (2008) 377–398.

[27] S. Mousavi, N. Sukumar, Numerical integration of polynomials and discontinuous functions on irregular convex polygons and polyhedrons, Computational Mechanics 47 (5) (2011) 535–554.

[28] J. E. Bishop, A displacement-based finite element formulation for general polyhedra using harmonic shape functions, International Journal for Numerical Methods in Engineering 97 (1) (2014) 1–31.

[29] G. Manzini, A. Russo, N. Sukumar, New perspectives on polygonal and polyhedral finite element methods, Mathematical Models and Methods in Applied Sciences 24 (08) (2014) 1665–1699.

[30] C. Talischi, A. Pereira, G. H. Paulino, I. F. Menezes, M. S. Carvalho, Polygonal finite elements for incompressible fluid flow, International Journal for Numerical Methods in Fluids 74 (2) (2014) 134–151.

[31] S. Biabanaki, A. Khoei, P. Wriggers, Polygonal finite element methods for contact-impact problems on non-conformal meshes, Computer Methods in Applied Mechanics and Engineering 269 (2014) 198–221.

[32] D. W. Spring, S. E. Leon, G. H. Paulino, Unstructured polygonal meshes with adaptive refinement for the numerical simulation of dynamic cohesive fracture, International Journal of Fracture 189 (1) (2014) 33–57.

[33] N. Sukumar, J. Bolander, Voronoi-based interpolants for fracture modelling, Tessellations in the Sciences.

[34] S. Leon, D. Spring, G. Paulino, Reduction in mesh bias for dynamic fracture using adaptive splitting of polygonal finite elements, International Journal for Numerical Methods in Engineering 100 (8) (2014) 555–576.

[35] C. Talischi, G. H. Paulino, A. Pereira, I. F. Menezes, Polytop: a matlab implementation of a general topology optimization framework using unstructured polygonal finite element meshes, Structural and Multidisciplinary Optimization 45 (3) (2012) 329–357.

[36] M. Floater, A. Gillette, N. Sukumar, Gradient bounds for wachspress coordinates on polytopes, SIAM Journal on Numerical Analysis 52 (1) (2014) 515–532.

[37] N. Sukumar, Quadratic maximum-entropy serendipity shape functions for arbitrary planar polygons, Computer Methods in Applied Mechanics and Engineering 263 (2013) 27–41.

[38] S. Martin, P. Kaufmann, M. Botsch, M. Wicke, M. Gross, Polyhedral finite elements using harmonic basis functions, in: Computer Graphics Forum, Vol. 27, Wiley Online Library, 2008, pp. 1521–1529.

[39] C. Talischi, G. H. Paulino, Addressing integration error for polygonal finite elements through polynomial projections: a patch test connection, Mathematical Models and Methods in Applied Sciences 24 (08) (2014) 1701–1727.

[40] C. Talischi, A. Pereira, I. F. Menezes, G. H. Paulino, Gradient correction for polygonal and polyhedral finite elements, International Journal for Numerical Methods in Engineering 102 (3-4) (2015) 728–747.

[41] L. Beirão Da Veiga, F. Brezzi, A. Cangiani, G. Manzini, L. Marini, A. Russo, Basic principles of virtual element methods, Mathematical Models and Methods in Applied Sciences 23(1) (2013) 199–214.

[42] B. Ahmad, A. Alsaedi, F. Brezzi, L. D. Marini, A. Russo, Equivalent projectors for virtual element methods, Computers & Mathematics with Applications 66 (3) (2013) 376–391.

[43] F. Brezzi, R. S. Falk, L. D. Marini, Basic principles of mixed virtual element methods, ESAIM: Mathematical Modelling and Numerical Analysis 48 (4) (2014) 1227–1240.

[44] J. Bonelle, A. Ern, Analysis of compatible discrete operator schemes for elliptic problems on polyhedral meshes, ESAIM: Mathematical Modelling and Numerical Analysis 48 (2) (2014) 553–581.

[45] G. Vacca, L. Beirão da Veiga, Virtual element methods for parabolic problems on polygonal meshes, Numerical Methods for Partial Differential Equations 31 (6) (2015) 2110–2134.

[46] B. A. de Dios, K. Lipnikov, G. Manzini, The nonconforming virtual element method, ESAIM: Mathematical Modelling and Numerical Analysis 50 (3) (2016) 879–904.

[47] K. Lipnikov, G. Manzini, M. Shashkov, Mimetic finite difference method, Journal of Computational Physics 257 (2014) 1163–1227.

[48] A. Gain, C. Talischi, G. H. Paulino, On the virtual element method for three-dimensional elasticity problems on arbitrary polyhedral meshes, Computer Methods in Applied Mechanics and Engineering 282 (2013) 132–160. doi:10.1016/j.cma.2014.05.005.

[49] E. Artioli, S. De Miranda, C. Lovadina, L. Patruno, A stress/displacement virtual element method for plane elasticity problems, Computer Methods in Applied Mechanics and Engineering 325 (2017) 155–174.

[50] E. Artioli, L. B. Da Veiga, C. Lovadina, E. Sacco, Arbitrary order 2d virtual elements for polygonal meshes: part i, elastic problem, Computational Mechanics 60 (3) (2017) 355–377.

[51] L. Beirão Da Veiga, F. Brezzi, L. D. Marini, Virtual elements for linear elasticity problems, SIAM Journal on Numerical Analysis 51 (2) (2013) 794–812.

[52] G. H. Paulino, A. L. Gain, Bridging art and engineering using escher-based virtual elements, Structural and Multidisciplinary Optimization 51 (4) (2015) 867–883.

[53] L. Beirão da Veiga, D. Mora, G. Rivera, A virtual element method for reissner-mindlin plates, Tech. rep., CI2MA preprint 2016-14, available from http://www. ci2ma. udec. cl.

[54] C. Chinosi, Vem for the reissner-mindlin plate based on the mitc approach: The element of degree 2, in: European Conference on Numerical Mathematics and Advanced Applications, Springer, 2017, pp. 519–527.

[55] V. Gyrya, H. M. Mourad, C1-continuous virtual element method for poisson-kirchhoff plate problem, Tech. rep., Los Alamos National Lab.(LANL), Los Alamos, NM (United States) (2016).

[56] V. M. Nguyen-Thanh, X. Zhuang, H. Nguyen-Xuan, T. Rabczuk, P. Wriggers, A virtual element method for 2d linear elastic fracture analysis, Computer Methods in Applied Mechanics and Engineering 340 (2018) 366–395.

[57] F. Aldakheel, B. Hudobivnik, P. Wriggers, Virtual element formulation for phase-field modeling of ductile fracture, International Journal for Multiscale Computational Engineering 17 (2).

[58] A. Hussein, B. Hudobivnik, P. Wriggers, A combined adaptive phase field and discrete cutting method for the prediction of crack paths.

[59] P. Wriggers, W. Rust, B. Reddy, A virtual element method for contact, Computational Mechanics 58 (6) (2016) 1039–1050.

[60] E. Artioli, S. Marfia, E. Sacco, High-order virtual element method for the homogenization of long fiber nonlinear composites, Computer Methods in Applied Mechanics and Engineering 341 (2018) 571–585.

[61] G. Vacca, An h 1-conforming virtual element for darcy and brinkman equations, Mathematical Models and Methods in Applied Sciences 28 (01) (2018) 159–194.

[62] O. Andersen, H. M. Nilsen, X. Raynaud, Virtual element method for geomechanical simulations of reservoir models, Computational Geosciences 21 (5-6) (2017) 877–893.

[63] J. Coulet, I. Faille, V. Girault, N. Guy, F. Nataf, A fully coupled scheme using virtual element method and finite volume for poroelasticity, Computational Geosciences (2019) 1–23.

[64] L. B. Da Veiga, A. Russo, G. Vacca, The virtual element method with curved edges, ESAIM: Mathematical Modelling and Numerical Analysis 53 (2) (2019) 375–404.

[65] E. Artioli, L. B. da Veiga, M. Verani, An adaptive curved virtual element method for the statistical homogenization of random fibre-reinforced composites, Finite Elements in Analysis and Design 177 (2020) 103418.

[66] P. Wriggers, B. Hudobivnik, F. Aldakheel, A virtual element formulation for general element shapes, Computational Mechanics (2020) 1–15.

[67] F. Brezzi, K. Lipnikov, V. Simoncini, A family of mimetic finite difference methods on polygonal and polyhedral meshes, Mathematical Models and Methods in Applied Sciences 15 (10) (2005) 1533–1551.

[68] F. Brezzi, A. Buffa, K. Lipnikov, Mimetic finite differences for elliptic problems, ESAIM: Mathematical Modelling and Numerical Analysis-Modélisation Mathématique et Analyse Numérique 43 (2) (2009) 277–295.

[69] F. Brezzi, K. Lipnikov, M. Shashkov, V. Simoncini, A new discretization methodology for diffusion problems on generalized polyhedral meshes, Computer Methods in Applied Mechanics and Engineering 196 (37-40) (2007) 3682–3692.

[70] F. Brezzi, K. Lipnikov, V. Simoncini, A family of mimetic finite difference methods on polygonal and polyhedral meshes, Math. Models Methods Appl. Sci. 15 (2005) 1533–1553.

[71] L. Beirão Da Veiga, A mimetic finite difference method for linear elasticity, M2AN: Math. Model. Numer. Anal 44 (2) (2010) 231–250.

[72] P. B. Bochev, J. M. Hyman, Principles of mimetic discretizations of differential operators, in: Compatible spatial discretizations, Springer, 2006, pp. 89–119.

[73] L. Beirão Da Veiga, F. Brezzi, L. Marini, A. Russo, The hitchhiker's guide to the virtual element method, Mathematical Models and Methods in Applied Sciences 24(8) (2014) 1541–1573.

[74] A. Sreekumar, S. P. Triantafyllou, F.-X. Bécot, F. Chevillotte, A multiscale virtual element method for the analysis of heterogeneous media, International Journal for Numerical Methods in Engineering 121 (8) (2020) 1791–1821.

[75] L. Beirão Da Veiga, F. Brezzi, L. D. Marini, A. Russo, Mixed virtual element methods for general second order elliptic problems on polygonal meshes, ESAIM: Mathematical Modelling and Numerical Analysis 50 (3) (2016) 727–747.

[76] F. Dassi, G. Vacca, Bricks for the mixed high-order virtual element method: projectors and differential operators.

[77] R. Bürger, S. Kumar, D. Mora, R. Ruiz-Baier, N. Verma, Virtual element methods for the three-field formulation of time-dependent linear poroelasticity, arXiv preprint arXiv:1912.06029.

[78] M. Buck, O. Iliev, H. Andrä, Multiscale finite elements for linear elasticity: oscillatory boundary conditions, in: Domain Decomposition Methods in Science and Engineering XXI, Springer, 2014, pp. 237–245.

[79] L. Beirão da Veiga, C. Lovadina, A. Russo, Stability analysis for the virtual element method, Mathematical Models and Methods in Applied Sciences 27 (13) (2017) 2557–2594.

[80] A. Cangiani, G. Manzini, A. Russo, N. Sukumar, Hourglass stabilization and the virtual element method, International Journal for Numerical Methods in Engineering 102 (3-4) (2015) 404–436.

[81] F. Dassi, L. Mascotto, Exploring high-order three dimensional virtual elements: bases and stabilizations, Computers & Mathematics with Applications 75 (9) (2018) 3379–3401.

[82] C. Talischi, G. H. Paulino, A. Pereira, I. F. M. Menezes, Polymesher: a general-purpose mesh generator for polygonal elements written in matlab, Structural and Multidisciplinary Optimization 45 (3) (2012) 309–328. doi:10.1007/s00158-011-0706-z.
URL https://doi.org/10.1007/s00158-011-0706-z

[83] L. Beirão da Veiga, F. Dassi, A. Russo, High-order virtual element method on polyhedral meshes, Computers & Mathematics with Applications 74 (5) (2017) 1110–1122.

Appendix A Monomial Spaces

The contents of the scalar and vector valued monomial spaces, i.e., $\mathbb{M}_k(\mathcal{K})$ and $[\mathbb{M}_k(\mathcal{K})]^2$ are provided in Table 12.
where $\xi = \frac{x-x_\mathcal{K}}{h_\mathcal{K}}$ and $\eta = \frac{y-y_\mathcal{K}}{h_\mathcal{K}}$ denote the scaled scalar valued monomials in each parametric direction, respectively. The diameter and the centroid of the element $\mathcal{K}$ are denoted by $h_\mathcal{K}$ and $(x_\mathcal{K}, y_\mathcal{K})^T$, respectively. The number of members of each of these spaces is generalizable to $n_k^{(1)} = \frac{(k+1)(k+2)}{2}$ and $n_k^{(2)} = (k+1)(k+2)$, respectively. The contents of the kernels $\mathbb{K}^{\boldsymbol{\mathcal{E}}}$ and $\mathbb{K}^{\nabla}$ are expressed as:

$$\mathbb{K}^{\boldsymbol{\mathcal{E}}}([\mathbb{M}(\mathcal{K})]^2) \equiv \mathbb{K}^{\boldsymbol{\mathcal{E}}}(\mathcal{K}) = \left\{ \begin{Bmatrix} 1 \\ 0 \end{Bmatrix}, \quad \begin{Bmatrix} 0 \\ 1 \end{Bmatrix}, \quad \begin{Bmatrix} \eta \\ -\xi \end{Bmatrix} \right\} \tag{69a}$$

$$\mathbb{K}^{\nabla}(\mathbb{M}(\mathcal{K})) \equiv \mathbb{K}^{\nabla}(\mathcal{K}) = \left\{ 1 \right\}. \tag{69b}$$

Polynomial order	$\mathbb{M}_k(\mathcal{K})$	$[\mathbb{M}_k(\mathcal{K})]^2$
$k=0$	$\mathbb{M}_0(\mathcal{K}) = \left\{1\right\}$	$[\mathbb{M}_0(\mathcal{K})]^2 = \left\{ \begin{Bmatrix} 1 \\ 0 \end{Bmatrix}, \quad \begin{Bmatrix} 0 \\ 1 \end{Bmatrix} \right\}$
arbitrary order k	$\mathbb{M}_k(\mathcal{K}) = \left\{ \mathbb{M}_{k-1}(\mathcal{K}), \quad \xi^k, \quad \xi^{k-1}\eta, \quad \ldots \quad \eta^k \right\}$	$[\mathbb{M}_k(\mathcal{K})]^2 = \left\{ [\mathbb{M}_{k-1}(\mathcal{K})]^2, \quad \begin{Bmatrix} \xi^k \\ 0 \end{Bmatrix}, \quad \begin{Bmatrix} 0 \\ \xi^k \end{Bmatrix}, \quad \begin{Bmatrix} \xi^{k-1}\eta \\ 0 \end{Bmatrix}, \quad \begin{Bmatrix} 0 \\ \xi^{k-1}\eta \end{Bmatrix}, \quad \ldots \quad \begin{Bmatrix} \eta^k \\ 0 \end{Bmatrix}, \quad \begin{Bmatrix} 0 \\ \eta^k \end{Bmatrix} \right\}$

Table 12: Generalized scalar and vector valued monomials for $\mathbb{M}_k(\mathcal{K})$ and $[\mathbb{M}_k(\mathcal{K})]^2$, respectively

905 The zero-energy modes of $\mathbb{K}^{\boldsymbol{\varepsilon}}(\mathcal{K})$ can be endowed with a rigid-body mechanics interpretation. In a 2D physical space, these correspond to two translations and a rotation, respectively.

Appendix B Virtual Projectors

Following Eq. (18), the projected quantities are expanded through the relevant monomial bases:

$$\Pi^{\boldsymbol{\varepsilon}}_k \mathbf{u}_\mathrm{h} = \sum_{i=1}^{n_k^{(2)}-3} \zeta_i^{\boldsymbol{\varepsilon}} \mathbf{m}_i, \quad \forall \mathbf{m}_i \in [\mathbb{M}_k(\mathcal{K})]^2 \setminus \mathbb{K}^{\boldsymbol{\varepsilon}}(\mathcal{K}) \tag{70a}$$

$$\Pi^{\nabla}_k \mathrm{p}_\mathrm{h} = \sum_{i=1}^{n_k^{(1)}-1} \zeta_i^{\nabla} \mathrm{m}_i, \quad \forall \mathrm{m}_i \in \mathbb{M}_k(\mathcal{K}) \setminus \mathbb{K}^{\nabla}(\mathcal{K}) \tag{70b}$$

$$\Pi^{0}_k \mathrm{p}_\mathrm{h} = \sum_{i=1}^{n_k^{(1)}} \zeta_i^{0} \mathrm{m}_i, \quad \forall \mathrm{m}_i \in \mathbb{M}_k(\mathcal{K}), \tag{70c}$$

where the unknown quantities $\zeta_i^{\boldsymbol{\varepsilon}}$, ζ_i^{∇} and ζ_i^0 are to be understood as discretized forms of the corresponding projection operators. These are collected

and stored in vector form in $\boldsymbol{\zeta}^{\boldsymbol{\varepsilon}}$, $\boldsymbol{\zeta}^{\nabla}$ and $\boldsymbol{\zeta}^{0}$, respectively. Inserting the expressions in Eq. (70) into the orthogonality conditions in Eq. (18) and simplifying, the following relations are obtained:

$$\sum_{i=1}^{n_k^{(2)}-3} \zeta_i^{\boldsymbol{\varepsilon}} \mathrm{a}_{\mathcal{K}}^{\boldsymbol{\varepsilon}}(\mathbf{m}_i, \mathbf{m}_j) = \mathrm{a}_{\mathcal{K}}^{\boldsymbol{\varepsilon}}(\mathbf{u}_h, \mathbf{m}_j) \tag{71a}$$

$$\sum_{i=1}^{n_k^{(1)}-1} \zeta_i^{\nabla} \mathrm{a}_{\mathcal{K}}^{\nabla}(\mathrm{m}_i, \mathrm{m}_j) = \mathrm{a}_{\mathcal{K}}^{\nabla}(\mathrm{p}_h, \mathrm{m}_j) \tag{71b}$$

$$\sum_{i=1}^{n_k^{(1)}} \zeta_i^{0} \mathrm{a}_{\mathcal{K}}^{0}(\mathrm{m}_i, \mathrm{m}_j) = \mathrm{a}_{\mathcal{K}}^{0}(\mathrm{p}_h, \mathrm{m}_j). \tag{71c}$$

The discretized projectors are solved for as follows

$$\boldsymbol{\zeta}^{\boldsymbol{\varepsilon}} = [\mathbf{G}^{\boldsymbol{\varepsilon}}]^{-1}\mathbf{B}^{\boldsymbol{\varepsilon}}, \tag{72a}$$

$$\boldsymbol{\zeta}^{\nabla} = [\mathbf{G}^{\nabla}]^{-1}\mathbf{B}^{\nabla}, \tag{72b}$$

$$\boldsymbol{\zeta}^{0} = [\mathbf{G}^{0}]^{-1}\mathbf{B}^{0}, \tag{72c}$$

For a more detailed discussion on the evaluation of $\mathcal{L}_2$ operator, please refer to [73, 76].

Appendix C Consistency Terms

The consistency terms as shown in Eq. (29) are defined as:

$$\mathbf{K}_C = \boldsymbol{\zeta}^{\boldsymbol{\varepsilon}^T} \underbrace{\left[\int_{\mathcal{K}_m} \boldsymbol{\varepsilon}(\mathbf{m}_i)\, \boldsymbol{\sigma}(\mathbf{m}_j)\, \mathrm{d}\mathcal{K} \right]}_{\mathbf{G}^{\boldsymbol{\varepsilon}}} \boldsymbol{\zeta}^{\boldsymbol{\varepsilon}}, \quad i,j = 1,\ldots,n_k^2 - 3, \tag{73a}$$

$$\mathbf{Q}_C = \boldsymbol{\zeta}^{\boldsymbol{\varepsilon}^T} \left[\int_{\mathcal{K}_m} \boldsymbol{\varepsilon}(\mathbf{m}_i)\ \{\alpha\mathbf{m}\}\ \mathrm{m}_j\, \mathrm{d}\mathcal{K} \right] \boldsymbol{\zeta}^0, \quad i = 1,\ldots,n_k^2 - 3,\ j = 1,\ldots,n_k^1, \tag{73b}$$

$$\mathbf{H}_C = \boldsymbol{\zeta}^{\nabla^T} \underbrace{\left[\int_{\mathcal{K}_m} \nabla(\mathrm{m}_i)\ \left\{ \frac{\mathbf{k}}{\gamma_f} \right\}\ \nabla(\mathrm{m}_j)\, \mathrm{d}\mathcal{K} \right]}_{\mathbf{G}^{\nabla}} \boldsymbol{\zeta}^{\nabla}, \quad i,j = 1,\ldots,n_k^1 - 1, \tag{73c}$$

$$\mathbf{S}_C = \boldsymbol{\zeta}^{0^T} \underbrace{\left[\int_{\mathcal{K}_m} \nabla(\mathrm{m}_i)\ \{\mathrm{S}_\varepsilon\}\ \nabla(\mathrm{m}_j)\, \mathrm{d}\mathcal{K} \right]}_{\mathbf{G}^0} \boldsymbol{\zeta}^0, \quad i,j = 1,\ldots,n_k^1, \tag{73d}$$

where only the integral term in Eq. (73b) needs to be freshly computed. The other integrals $\mathbf{G}^{\boldsymbol{\varepsilon}}$, $\mathbf{G}^{\nabla}$ and $\mathbf{G}^0$ have already been computed to derive the necessary projection operators in Section B.

Appendix D Stability Terms

The stability terms as shown in Eq. (29) are defined as:

$$\mathcal{S}_{\mathcal{K}}^K(\mathbf{u}_h, \mathbf{v}_h) \equiv \mathbf{K}_S = (\mathbb{I}_2 - \boldsymbol{\Pi}_{\mathrm{tot}}^{\boldsymbol{\varepsilon}})\, \beta_K\, (\mathbb{I}_2 - \boldsymbol{\Pi}_{\mathrm{tot}}^{\boldsymbol{\varepsilon}}) \tag{74a}$$

$$\mathcal{S}_{\mathcal{K}}^Q(\mathbf{u}_h, \mathrm{w}_h) \equiv \mathbf{Q}_S = (\mathbb{I}_2 - \boldsymbol{\Pi}_{\mathrm{tot}}^{\boldsymbol{\varepsilon}})\, \beta_Q\, (\mathbb{I}_1 - \boldsymbol{\Pi}_{\mathrm{tot}}^{0}) \tag{74b}$$

$$\mathcal{S}_{\mathcal{K}}^H(\mathrm{p}_h, \mathbf{w}_h) \equiv \mathbf{H}_S = (\mathbb{I}_1 - \boldsymbol{\Pi}_{\mathrm{tot}}^{\nabla})\, \beta_H\, (\mathbb{I}_1 - \boldsymbol{\Pi}_{\mathrm{tot}}^{\nabla}) \tag{74c}$$

$$\mathcal{S}_{\mathcal{K}}^S(\mathrm{p}_h, \mathrm{w}_h) \equiv \mathbf{S}_S = (\mathbb{I}_1 - \boldsymbol{\Pi}_{\mathrm{tot}}^{0})\, \beta_S\, (\mathbb{I}_1 - \boldsymbol{\Pi}_{\mathrm{tot}}^{0}), \tag{74d}$$

where $\mathbb{I}_1$ and $\mathbb{I}_2$ denote appropriately sized identity matrices and β_K, β_Q, β_H and β_S denote stabilization parameters. The classical choice for these parameters, as originally defined only for β_K in [41, 73] is given:

$$\beta_K^{(1)} = |\mathcal{K}|, \tag{75}$$

where the area of the element under consideration has been included to ensure scaling of the stabilization energy with element-size. However, non-optimal error convergence rates in the case of three-dimensional higher order methods have been reported with this choice in [83].

An alternate strategy for defining β_S, the D-recipe stabilization, (originally proposed in [81] and adapted into an engineering context in [48]) is used here for defining all stability parameters:

$$\beta_K^{(2)} = \gamma_K \, |\mathcal{K}| \frac{\mathrm{tr}(\mathbb{D})}{\mathrm{tr}(\mathbf{D}^{\boldsymbol{\varepsilon}^T} \mathbf{D}^{\boldsymbol{\varepsilon}})}, \tag{76a}$$

$$\beta_Q^{(2)} = \gamma_Q \, |\mathcal{K}| \frac{\mathrm{tr}(\alpha \, \mathbf{m})}{\mathrm{tr}(\mathbf{D}^{0^T} \mathbf{D}^{0})}, \tag{76b}$$

$$\beta_H^{(2)} = \gamma_H \, |\mathcal{K}| \frac{\mathbf{k}/\gamma_f}{\mathrm{tr}(\mathbf{D}^{\nabla^T} \mathbf{D}^{\nabla})}, \tag{76c}$$

$$\beta_S^{(2)} = \gamma_S \, |\mathcal{K}| \frac{\mathrm{tr}(\mathrm{S}_\varepsilon)}{\mathrm{tr}(\mathbf{D}^{0^T} \mathbf{D}^{0})}, \tag{76d}$$

where the scaling parameters $\gamma_K = \gamma_Q = \gamma_H = \gamma_S = 1$. The D-recipe approach ensures correct scaling in relation to the associated consistency terms by taking into account the material parameters involved in the formulation. The terms $\mathbf{D}^{\boldsymbol{\varepsilon}}$, $\mathbf{D}^{\nabla}$ and $\mathbf{D}^{0}$ contain the relevant monomials evaluated at each DoF:

$$\mathbf{D}^{\boldsymbol{\varepsilon}} = \begin{bmatrix} \mathrm{dof}_1(\mathbf{m}_1) & \dots & \mathrm{dof}_1(\mathbf{m}_{n_k^{(2)}-3}) \\ \vdots & \ddots & \vdots \\ \mathrm{dof}_{n^{(2)}}(\mathbf{m}_1) & \dots & \mathrm{dof}_{n^{(2)}}(\mathbf{m}_{n_k^{(2)}-3}) \end{bmatrix}, \quad \forall \, \mathbf{m} \in [\mathbb{M}_\mathrm{k}(\mathcal{K})]^2 \setminus \mathbb{K}^{\boldsymbol{\varepsilon}}(\mathcal{K}) \tag{77a}$$

$$\mathbf{D}^{\nabla} = \begin{bmatrix} \mathrm{dof}_1(\mathrm{m}_1) & \dots & \mathrm{dof}_1(\mathrm{m}_{n_k^{(1)}-1}) \\ \vdots & \ddots & \vdots \\ \mathrm{dof}_{n^{(1)}}(\mathrm{m}_1) & \dots & \mathrm{dof}_{n^{(1)}}(\mathrm{m}_{n_k^{(1)}-1}) \end{bmatrix}, \quad \forall \, \mathrm{m} \in \mathbb{M}_\mathrm{k}(\mathcal{K}) \setminus \mathbb{K}^{\nabla}(\mathcal{K}) \tag{77b}$$

$$\mathbf{D}^{0} = \begin{bmatrix} \mathrm{dof}_1(\mathrm{m}_1) & \dots & \mathrm{dof}_1(\mathrm{m}_{n_k^{(1)}}) \\ \vdots & \ddots & \vdots \\ \mathrm{dof}_{n^{(1)}}(\mathrm{m}_1) & \dots & \mathrm{dof}_{n^{(1)}}(\mathrm{m}_{n_k^{(1)}}) \end{bmatrix}, \quad \forall \, \mathrm{m} \in \mathbb{M}_\mathrm{k}(\mathcal{K}), \tag{77c}$$

where $n^{(1)} = kN_v + \frac{k(k+1)}{2}$ and $n^{(2)} = 2kN_v + k(k+1)$ are the number of DoFs of the $\mathcal{V}_{\mathrm{h}2}$ and $\mathcal{V}_{\mathrm{h}1}$, respectively, as shown in Table 1.

The projection operators in Eq. (74) are defined as follows:

$$\mathbf{\Pi}^{\boldsymbol{\varepsilon}}_{\text{tot}} = \mathbf{D}^{\boldsymbol{\varepsilon}}\boldsymbol{\zeta}^{\boldsymbol{\varepsilon}} + \mathbf{D}^{\boldsymbol{\varepsilon}}_{S}\boldsymbol{\zeta}^{\boldsymbol{\varepsilon}}_{S} \tag{78a}$$

$$\mathbf{\Pi}^{\nabla}_{\text{tot}} = \mathbf{D}^{\nabla}\boldsymbol{\zeta}^{\nabla} + \mathbf{D}^{\nabla}_{S}\boldsymbol{\zeta}^{\nabla}_{S} \tag{78b}$$

$$\mathbf{\Pi}^{0}_{\text{tot}} = \mathbf{D}^{0}\boldsymbol{\zeta}^{0}, \tag{78c}$$

where $\mathbf{D}^{\boldsymbol{\varepsilon}}_{S}$ and $\mathbf{D}^{\nabla}_{S}$ contain monomials from the relevant kernel spaces, evaluated at each DoF.

$$\mathbf{D}^{\boldsymbol{\varepsilon}}_{S} = \begin{bmatrix} \text{dof}_1(\mathbf{m}_1) & \dots & \text{dof}_1(\mathbf{m}_3) \\ \vdots & \ddots & \vdots \\ \text{dof}_{n^{(2)}}(\mathbf{m}_1) & \dots & \text{dof}_{n^{(2)}}(\mathbf{m}_3) \end{bmatrix}, \quad \forall\, \mathbf{m} \in \mathbb{K}^{\boldsymbol{\varepsilon}}(\mathcal{K}) \tag{79a}$$

$$\mathbf{D}^{\nabla}_{S} = \begin{bmatrix} \text{dof}_1(\mathrm{m}_1) \\ \vdots \\ \text{dof}_{n^{(1)}}(\mathrm{m}_1) \end{bmatrix}, \quad \forall\, \mathrm{m} \in \mathbb{K}^{\nabla}(\mathcal{K}). \tag{79b}$$

The stability projection operators $\boldsymbol{\zeta}^{\boldsymbol{\varepsilon}}_{S}$ and $\boldsymbol{\zeta}^{\nabla}_{S}$ can be computed:

$$\boldsymbol{\zeta}^{\boldsymbol{\varepsilon}}_{S} = [\mathbf{G}^{\boldsymbol{\varepsilon}}_{S}]^{-1}\mathbf{B}^{\boldsymbol{\varepsilon}}_{S} \tag{80a}$$

$$\boldsymbol{\zeta}^{\nabla}_{S} = [\mathbf{G}^{\nabla}_{S}]^{-1}\mathbf{B}^{\nabla}_{S}, \tag{80b}$$

where $\mathbf{G}^{\boldsymbol{\varepsilon}}_{S} = \mathbf{B}^{\boldsymbol{\varepsilon}}_{S}\mathbf{D}^{\boldsymbol{\varepsilon}}_{S}$ and $\mathbf{G}^{\nabla}_{S} = \mathbf{B}^{\nabla}_{S}\mathbf{D}^{\nabla}_{S}$. The terms $\mathbf{B}^{\boldsymbol{\varepsilon}}_{S}$ and $\mathbf{B}^{\nabla}_{S}$ are specially defined:

$$\mathbf{B}^{\boldsymbol{\varepsilon}}_{S} = \begin{bmatrix} 1/N_v & 0 & 1/N_v & 0 & \dots \\ 0 & 1/N_v & 0 & 1/N_v & \dots \\ \eta(\mathbf{x}_1) & -\xi(\mathbf{x}_1) & \eta(\mathbf{x}_2) & -\xi(\mathbf{x}_2) & \dots \end{bmatrix} \tag{81a}$$

$$\mathbf{B}^{\nabla}_{S} = \begin{bmatrix} 1/N_v & 1/N_v & \dots \end{bmatrix}. \tag{81b}$$

For a more detailed discussion on defining stability matrices, please refer to [73].

Appendix E Computing oscillatory kinematical constraints

For the RVE ($\alpha = 2$) shown in Fig. 5b and the micro-element i = 9, Eq. (33) assumes the following form:

$$\mathbf{u}^2_{\mathrm{m}(9)} = \underbrace{\mathbf{N}^{\mathrm{u}}_{\mathrm{m}(9)}}_{12\times 12}\,\mathbf{u}_{\mathrm{M}(2)} \tag{82a}$$

$$\mathbf{p}^2_{\mathrm{m}(9)} = \underbrace{\mathbf{N}^{\mathrm{p}}_{\mathrm{m}(9)}}_{6\times 6}\,\mathbf{p}_{\mathrm{M}(2)}, \tag{82b}$$

where the fine nodal displacement $\mathbf{u}^2_{\mathrm{m}(9)}$ and pressure $\mathbf{p}^2_{\mathrm{m}(9)}$ vectors are

$$\mathbf{u}^2_{\mathrm{m}(9)} = \Big[\mathrm{u_{mx,6}} \quad \mathrm{u_{my,6}} \quad \mathrm{u_{mx,7}} \quad \mathrm{u_{my,7}} \quad \mathrm{u_{mx,13}} \quad \mathrm{u_{my,13}} \quad \mathrm{u_{mx,12}} \quad \mathrm{u_{my,12}} \quad \mathrm{u_{mx,11}} \quad \mathrm{u_{my,11}} \quad \mathrm{u_{mx,10}} \quad \mathrm{u_{my,10}},\Big]^T \tag{83}$$

and

$$\mathbf{p}^2_{\mathrm{m}(9)} = \Big[\mathrm{p_{m,6}} \quad \mathrm{p_{m,7}} \quad \mathrm{p_{m,13}} \quad \mathrm{p_{m,12}} \quad \mathrm{p_{m,11}} \quad \mathrm{p_{m,10}}\Big]^T, \tag{84}$$

respectively. Similarly, the corresponding nodal vectors at the coarse scale are

$$\mathbf{u}_{\mathrm{M}(2)} = \Big[\mathrm{u_{Mx,2}} \quad \mathrm{u_{My,2}} \quad \mathrm{u_{Mx,3}} \quad \mathrm{u_{My,3}} \quad \mathrm{u_{Mx,9}} \quad \mathrm{u_{My,9}} \quad \mathrm{u_{Mx,8}} \quad \mathrm{u_{My,8}} \quad \mathrm{u_{mx,7}} \quad \mathrm{u_{my,7}} \quad \mathrm{u_{mx,6}} \quad \mathrm{u_{my,6}},\Big]^T, \tag{85}$$

and

$$\mathbf{p}_{\mathrm{M}(2)} = \Big[\mathrm{p_{M,2}} \quad \mathrm{p_{M,3}} \quad \mathrm{p_{M,9}} \quad \mathrm{p_{M,8}} \quad \mathrm{p_{M,7}} \quad \mathrm{p_{M,6}}\Big]^T, \tag{86}$$

for the displacements and pressures, respectively.

For the RVE ($\alpha = 2$) shown in Fig. 5b, the arrays of multiscale basis function arrays $\mathbf{N}^{\mathrm{u}}_{\mathrm{m}}$ and $\mathbf{N}^{\mathrm{p}}_{\mathrm{m}}$ are 42×12 and 21×6 matrices, respectively. To compute the kinematical constraints for $\mathbf{N}^{\mathrm{u}}_{\mathrm{M},6}$ and $\mathbf{N}^{\mathrm{p}}_{\mathrm{M},6}$ as illustrated in Fig. 5b, the edge boundaries are grouped into opposite and adjacent edges as shown in Table 13. Kinematical constraints are then assigned to the RVE as follows:

- To compute $\mathbf{N}^{\mathrm{u}}_{\mathrm{Mx},6}$:

1. Solve reduced version of Eq. (35) for $\bar{\mathrm{u}}_\mathrm{x}$ over Γ_{Adj}:

$$-\frac{\partial}{\partial\xi}\cdot\left(\mathrm{E}\frac{\partial\bar{\mathrm{u}}_\mathrm{x}}{\partial\xi}\right)=0 \text{ on } \Gamma_{\mathrm{M_7M_6}},\quad \bar{\mathrm{u}}_\mathrm{x}(\xi_{\mathrm{M_6}})=1,\ \bar{\mathrm{u}}_\mathrm{x}(\xi_{\mathrm{M_7}})=0 \tag{87a}$$

$$-\frac{\partial}{\partial\xi}\cdot\left(\mathrm{E}\frac{\partial\bar{\mathrm{u}}_\mathrm{x}}{\partial\xi}\right)=0 \text{ on } \Gamma_{\mathrm{M_6M_2}},\quad \bar{\mathrm{u}}_\mathrm{x}(\xi_{\mathrm{M_6}})=1,\ \bar{\mathrm{u}}_\mathrm{x}(\xi_{\mathrm{M_2}})=0. \tag{87b}$$

2. Assign $\bar{\mathrm{u}}_\mathrm{x}$ to $x-$DoFs on adjacent edges: $\bar{\mathrm{u}}_\mathrm{x}|_{\Gamma_{\mathrm{adj}}}=\bar{\mathrm{u}}_\mathrm{x}$.
3. Assign sliding conditions to $y-$DoFs on adjacent edges: $\bar{\mathrm{u}}_\mathrm{y}|_{\Gamma_{\mathrm{adj}}}=0$.
4. Assign fully clamped conditions on opposite edges: $\bar{\mathbf{u}}|_{\Gamma_{\mathrm{opp}}}=\mathbf{0}$.

- To compute $\mathbf{N}^{\mathrm{u}}_{\mathrm{My},6}$:

1. Solve reduced version of Eq. (35) for $\bar{\mathrm{u}}_\mathrm{y}$ over Γ_{Adj}:

$$-\frac{\partial}{\partial\xi}\cdot\left(\mathrm{E}\frac{\partial\bar{\mathrm{u}}_\mathrm{y}}{\partial\xi}\right)=0 \text{ on } \Gamma_{\mathrm{M_7M_6}},\quad \bar{\mathrm{u}}_\mathrm{y}(\xi_{\mathrm{M_6}})=1,\ \bar{\mathrm{u}}_\mathrm{y}(\xi_{\mathrm{M_7}})=0 \tag{88a}$$

$$-\frac{\partial}{\partial\xi}\cdot\left(\mathrm{E}\frac{\partial\bar{\mathrm{u}}_\mathrm{y}}{\partial\xi}\right)=0 \text{ on } \Gamma_{\mathrm{M_6M_2}},\quad \bar{\mathrm{u}}_\mathrm{y}(\xi_{\mathrm{M_6}})=1,\ \bar{\mathrm{u}}_\mathrm{y}(\xi_{\mathrm{M_2}})=0. \tag{88b}$$

2. Assign $\bar{\mathrm{u}}_\mathrm{y}$ to $y-$DoFs on adjacent edges: $\bar{\mathrm{u}}_\mathrm{y}|_{\Gamma_{\mathrm{adj}}}=\bar{\mathrm{u}}_\mathrm{y}$.
3. Assign sliding conditions to $x-$DoFs on adjacent edges: $\bar{\mathrm{u}}_\mathrm{x}|_{\Gamma_{\mathrm{adj}}}=0$.
4. Assign fully clamped conditions on opposite edges: $\bar{\mathbf{u}}|_{\Gamma_{\mathrm{opp}}}=\mathbf{0}$.

- To compute $\mathbf{N}^{\mathrm{p}}_{\mathrm{M},6}$:

1. Solve reduced version of Eq. (36) for $\bar{\mathrm{p}}$ over Γ_{Adj}:

$$-\frac{\partial}{\partial\xi}\cdot\left(\frac{\mathbf{k}}{\gamma_\mathrm{f}}\frac{\partial\bar{\mathrm{p}}}{\partial\xi}\right)=0 \text{ on } \Gamma_{\mathrm{M_7M_6}},\quad \bar{\mathrm{p}}(\xi_{\mathrm{M_6}})=1,\ \bar{\mathrm{p}}(\xi_{\mathrm{M_7}})=0 \tag{89a}$$

$$-\frac{\partial}{\partial\xi}\cdot\left(\frac{\mathbf{k}}{\gamma_\mathrm{f}}\frac{\partial\bar{\mathrm{p}}}{\partial\xi}\right)=0 \text{ on } \Gamma_{\mathrm{M_6M_2}},\quad \bar{\mathrm{p}}(\xi_{\mathrm{M_6}})=1,\ \bar{\mathrm{p}}(\xi_{\mathrm{M_2}})=0 \tag{89b}$$

2. Assign $\bar{\mathrm{p}}$ on adjacent edges: $\bar{\mathrm{p}}|_{\Gamma_{\mathrm{adj}}}=\bar{\mathrm{p}}$.
3. Assign zero conditions on opposite edges: $\bar{\mathrm{p}}|_{\Gamma_{\mathrm{opp}}}=\mathbf{0}$.

	Edges	Nodes
Opposite (Opp)	$\Big(\Gamma_{M_2M_3},\ \Gamma_{M_3M_9},\ \Gamma_{M_9M_8},\ \Gamma_{M_8M_7}\Big)$	$\Big(1,\ 2,\ 3,\ 8,\ 15,\ 18,\ 21,\ 20,\ 19\Big)$
Adjacent (Adj)	$\Big(\Gamma_{M_7M_6},\ \Gamma_{M_6M_2}\Big)$	$\Big(19,\ 17,\ 16,\ 9,\ 4,\ 1\Big)$

Table 13: Opposite and adjacent boundary edges and nodes used for computing multiscale basis functions